Investigating High-T_C Superconductivity on the Atomic Scale by Scanning Tunneling Microscopy

by

Eric William Hudson

B.A. (University of Chicago) 1992
M.A. (University of California, Berkeley) 1994

A dissertation submitted in partial satisfaction of the

requirements for the degree of

Doctor of Philosophy

in

Physics

in the

GRADUATE DIVISION

of the

UNIVERSITY OF CALIFORNIA AT BERKELEY

Committee in charge:

Professor J.C. Séamus Davis, Chair
Professor Paul McEuen
Professor Norman Phillips

Spring 1999

The dissertation of Eric William Hudson is approved:

James Davis   5/11/1999

Chair   Date

Paul McE   5/19/99

                             Date

Norman E. Phillips   5/20/99

                             Date

University of California at Berkeley

Spring 1999

Investigating High-T_C Superconductivity
on the Atomic Scale
by
Scanning Tunneling Microscopy

Abstract

Investigating High-T$_C$ Superconductivity on the Atomic Scale by Scanning Tunneling Microscopy
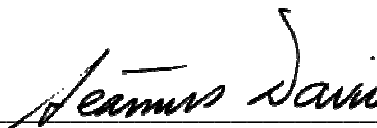
by

Eric William Hudson

Doctor of Philosophy in Physics

University of California at Berkeley

Professor J.C. Séamus Davis, Chair

More than 10 years after the initial discovery of high T$_c$ superconductivity, a microscopic theory comparable to the BCS theory of conventional superconductivity has still not emerged. A number of important advances have been made, however, on both theoretical and experimental fronts.   In particular, several investigations have demonstrated, macroscopically, the d-wave nature of the order parameter in these exotic superconductors. In this thesis I will present a newly developed technique that extends these investigations to the atomic scale. Using a specially designed scanning tunneling microscope, we have studied the effects of atomic scale perturbations to the order parameter in the high temperature superconductor $Bi_2Sr_2CaCu_2O_{8+\delta}$. Quasiparticle scattering from native scattering centers and quantized vortices induced by the application of magnetic fields allow us to observe the response of the pairing mechanism to microscopic disturbances and might one day help to unlock its remaining secrets.

Professor J.C. Séamus Davis
Dissertation Committee Chair

To my wife,

Amy Sarah Aukerman

who put up with seven years of long days and nights

Table of Contents

List of Figures

Acknowledgements

The results described in this thesis are the product of the hard work by many individuals, whom I'd like to thank. First of all, thanks to my mentor Dr. Shuheng Pan, without whom none of this would have been possible. He has taught me nearly all I know about scanning tunneling microscopy and has inspired me to continue in this fascinating field. Thanks also to my long-time coworker and friend Andrew Schechter, who helped me build a lab out of an empty room and always seemed willing (and able) to help me rethink problems I was having. Then undergrads Ray Simmonds, Claudia YiLeon and Mike Braganza were instrumental in helping me design, build and test the vibration isolation and fridge. Abram Hardin went out of his way to help us get things going, as did George Weber, who taught me a lot about machining and design. Tom Pedersen's handiwork can be seen throughout our apparatus, from the RF shielding to the STM body – we wouldn't be where we are now without his ingenuity and skill. Thanks also to friend and coworker Kristine Lang, who has been invaluable in helping me analyze our results and get through this thesis.

I'd be remiss in not thanking my family and friends as well. To my parents, who read all of my papers, even though I'm not entirely sure they understood any of them, and to my sister Paula, who probably did, I'd like to say thanks for all of your support. Thanks also to Bob and Geoff, who reminded me that its important to have fun in life, and that although writing this thing didn't necessarily fall into that category, discovering what's in it certainly did.

And finally, I'd like to thank my advisor Professor Séamus Davis, who has taught me, through consummate example, how to be a physicist. He has pushed me, and induced me to push myself, to achieve the results chronicled, in part, in these pages.

Curriculum Vita

ERIC W. HUDSON

1945 Berkeley Way #318
Berkeley, CA 94704-1002
Phone: 510-486-8369
E-mail: ehudson@socrates.berkeley.edu
Web: http://socrates.berkeley.edu/~ehudson

Department of Physics
University of California
Berkeley, CA 94720-7300
510-643-9090

Degrees:

Ph.D.	Physics, University of California, Berkeley,	1999
M.A.	Physics, University of California, Berkeley,	1994
B.A.	Physics/Linguistics, University of Chicago,	1992

Dissertation

"Investigating High-T_C Superconductivity on the Atomic Scale by Scanning Tunneling Microscopy"
Committee: J.C. Séamus Davis (Thesis Chair); Paul McEuen; Norman Phillips

Fellowships, Grants and Awards:

NIST/NRC Postdoctoral Research	NIST	1999-2001
Volunteer Service Award	Department of Physics, UC Berkeley	1997
Graduate Research Fellowship	Department of Physics, UC Berkeley	1994-1996
Outstanding GSI Award	UC Berkeley	1993
Phi Beta Kappa	University of Chicago	1992

Teaching Experience:

Academic Tutor - Physics   U.C. Berkeley, Housing and Dining   1996-1998
   Led individual and group tutoring sessions in dormitory academic center
Academic Tutor - Physics & Math   U.C. Berkeley, Housing and Dining   1995-1996
Head Graduate Student Instructor   U.C. Berkeley, Physics Department
   Taught discussion and laboratory sections, held office hours, graded exams, and performed
   administrative duties

Physics 8B: Introductory Physics (E&M, Modern)	Fall 1993
Physics 8A: Introductory Physics (Mechanics, Fluids)	Summer 1993
Physics 8A	Spring 1993

Graduate Student Instructor   U.C. Berkeley, Physics Department
   Taught discussion and laboratory sections, held office hours and graded exams and lab reports

Physics 8B	Fall 1992

Academic Tutor - Math   Univ. of Chicago   1990-1992
   Led individual and group tutoring sessions in library study lounge
Discussion Section Leader   Univ. of Chicago, Math Department   1989-1990
   Led discussion sections and graded homework for the Math 130 sequence, introductory calculus

Community Service:

Longfellow Middle School Science Outreach Program	1995-1997
Physics Department Web Developer	1994-1998
Instructional Technology Program Graduate Student Council	1994-1998
Computer Committee, U.C. Berkeley Physics Dept.	1995-1997
Faculty-Student Liaison Committee, U.C. Berkeley Physics Department	1993-1994

Research Experience:

STM on Exotic Superconductors   U.C. Berkeley   1994-Present

We have constructed a very low temperature scanning tunneling microscope (STM), using a custom-built ^{3}He fridge, operating between the temperatures of 250 mK and 30 K and in magnetic fields of up to 7.25 T. Using this STM we have studied the topography and the density of states of both high-T_c ($YBa_2Cu_3O_{7-x}$ and $Bi_2Sr_2CaCu_2O_{8+x}$) and p-wave (Sr_2RuO_4) superconductors. We have focussed particularly on defects in the order parameter, caused by, for example, intentionally doped impurities or by magnetic vortices. We hope that by closely studying the density of states near these defects that we can derive further understanding of the pairing mechanism and other features of these exotic materials.

Modeling Catalysis of CO   Argonne National Lab   Summer 1990

I created a simple model of catalysis of CO on a Pd substrate using cellular automata methods in order to try to replicate and understand the chaotic behavior of this experimental system.

Publications:

"Evidence for a Charge Density Wave in Sr_2RuO_4 by Scanning Tunneling Microscopy," E.W. Hudson, S.H. Pan, A.V. Puchkov, Z.X. Shen, T. Kimura and Y. Tokura, and J.C. Davis, *in preparation.*.

"Quasiparticle Scattering from Single Zn Impurities in $Bi_2Sr_2Ca(Cu_{1-x}Zn_x)_2O_{8+\delta}$," E.W. Hudson, S.H. Pan, K.M. Lang, H. Eisaki, S. Uchida, and J.C. Davis, *in preparation*.

"Atomic Scale Imaging and Spectroscopy of Vortices in $Bi_2Sr_2CaCu_2O_{8+\delta}$," S.H. Pan, E.W. Hudson, A.K. Gupta, K.-W. Ng, and J.C. Davis, *in preparation*.

"Atomic Scale Quasiparticle Scattering Resonances in $Bi_2Sr_2CaCu_2O_{8+\delta}$," E.W. Hudson, S.H. Pan, A.K. Gupta, K.-W. Ng, and J.C. Davis, *to appear in Science*.

"Search for Superconductivity in Lithium," K.M. Lang, Ari Mizel, J. Mortara, E. Hudson, J. Hone, Marvin L. Cohen, A. Zettl, and J.C. Davis, *J. Low Temp. Phys.* **114** (5/6), 445 (1999).

"^{3}He Refrigerator Based Very Low Temperature Scanning Tunneling Microscope," S.H. Pan, E.W. Hudson and J.C. Davis, *Rev. Sci. Inst.* **70** (2), 1459 (1999).

"Vacuum tunneling of superconducting quasiparticles from atomically sharp scanning tunneling microscope tips**,**" S.H. Pan, E.W. Hudson and J.C. Davis, *App. Phys. Lett*. **73** (20), 2992 (1998).

"Imaging and identification of atomic planes of cleaved $Bi_2Sr_2CaCu_2O_{8+\delta}$ by high resolution scanning tunneling microscopy," S.H. Pan, E.W. Hudson, J. Ma and J.C. Davis, *App. Phys. Lett.* **73** (1), 58 (1998).

"A very low temperature vibration isolation system," E.W. Hudson, R.W. Simmonds, C.A. YiLeon, S.H. Pan and J.C. Davis, *Czech. J. Of Phys.* **46** (S5), 2737 (1996).

Presentations:

May 1999   Superconducting Vortices and Related Phenomena (Irvine, CA)
        "Atomic Scale Imaging and Spectroscopy of Vortices in $Bi_2Sr_2CaCu_2O_{8+\delta}$."
March 1999   American Physical Society (Atlanta, GA)
        "Evidence for a Charge Density Wave in Sr_2RuO_4 by Scanning Tunneling Microscopy and Spectroscopy."
March 1999   American Physical Society (Atlanta, GA)
        "High Resolution, Low Temperature STM/STS of Vortices in Single Crystal $Bi_2Sr_2CaCu_2O_{8+\delta}$."
March 1998   American Physical Society (Los Angeles, CA)
        "Observation of Multiple Atomic Layers on Bi-2212 by Low Temperature Scanning Tunneling Microscopy."
March 1997   Cal Day (University of California, Berkeley)
        "Low Temperature Physics."

Professional Membership:

American Physical Society   1992-Present

Chapter 1.

Design and Operation of a ^{3}He Refrigerator Based Scanning Tunneling Microscope

All of the results described in this thesis were obtained with a scanning tunneling microscope (STM) that operates, with high spatial and energy resolution, at temperatures down to 240 mK and in magnetic fields up to 7.25 T. The system consists of a compact and rigid STM head, mounted directly on a low vibration, single shot, ^{3}He refrigerator. This refrigerator can be operated at its base temperature continuously for several days before the ^{3}He needs to be recondensed. The system is equipped with a sample transport manipulator from room temperature and a cleavage device at low temperature, so that the cryogenic ultrahigh vacuum (UHV) condition inside the cryostat can be utilized. A superconducting magnet provides a field of up to 7.25 T at the sample along the STM tip direction. In this chapter I will describe the design and operation of this STM system, which, at its base temperature, has better than 0.5 pm z-direction resolution in imaging mode, and better than 20 μV energy resolution in spectroscopy mode.

1.1. Background

An important direction for the development of scanning tunneling microscopes (STMs) is toward applications in the millikelvin temperature range. Such instruments will permit the study of physical phenomena that occur only at very low temperatures. For example, the superconducting phase transition in Sr_2RuO_4, a p-wave superconductor structurally isomorphic to the high-T_c superconductor $La_{2-x}Ba_xCuO_4$, occurs at 1 K. Even for phenomena that occur and are observable at higher temperatures, energy resolution (which is limited by thermal broadening) can be dramatically improved if the measurements are performed at millikelvin temperatures. For example, spectroscopy of the vortex core states of $NbSe_2$ (as discussed in chapter 2), which we can clearly image at 300 mK, are nearly impossible to resolve at 4.2 K. Although numerous STM instruments have produced results near 4.2 K, few have been used at much lower temperatures (Hess 1991, Fukuyama 1996). Here I will describe the development of a very low temperature STM with very high spatial and spectroscopic resolution for operation in a magnetic field.

1.2. Instrument design

Operation of a scanning tunneling microscope at low temperatures brings the benefits of low thermal drift and low thermal noise, which are required for high-resolution measurements. On the other hand, very low temperature refrigeration techniques often hamper the efforts to achieve high-resolution measurements due to the

introduction of mechanical vibrations. Furthermore, the physical space within the cryostat, especially when a high magnetic field is required, is often too limited to allow an effective cryogenic vibration-isolation stage. Our efforts to address these challenges are concentrated in the following three elements: 1. a very rigid STM head that is less susceptible to vibration, 2. a refrigeration scheme that has very low intrinsic vibrational noise and 3. a good external vibration-isolation system to reduce transmission of vibrations from the external environment to the STM cryostat.

1.2.1. STM head

To fit into the limited space inside the refrigerator, and to adapt to the configuration of the refrigeration scheme, our STM head is required to be compact and arranged for top loading of samples. Figure 1.1 shows a schematic diagram of the STM head. It integrates a coarse-approach motor and a tube scanner into a main body (8)
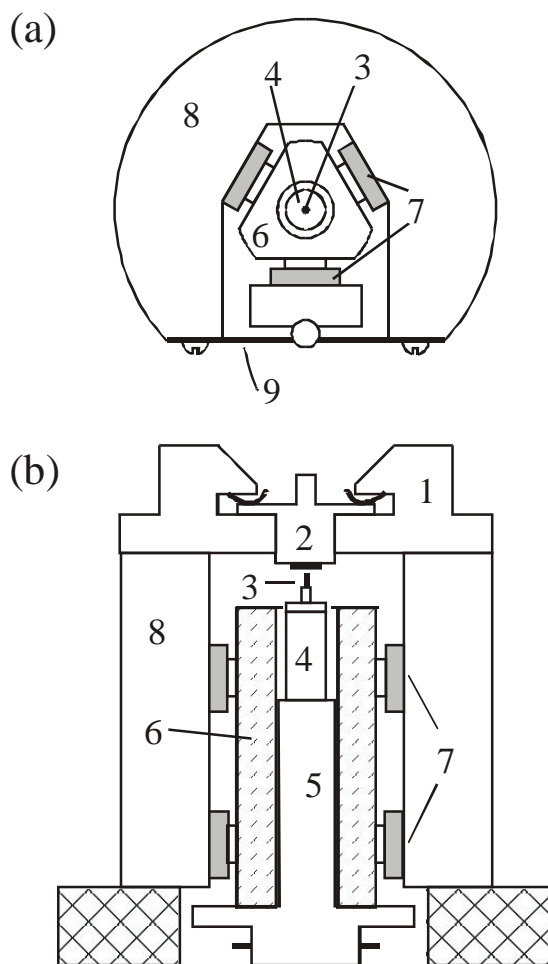
Figure 1.1. The STM head, (a) top view (with sample receptacle removed for clarity) and (b) side view. 1.5" in diameter by 1.75" high. (1) Sample Receptacle, (2) Sample Holder, (3) Tip, (4) Tube Scanner, (5) Scanner Holder, (6) Sapphire Prism, (7) Shear Piezo Stacks, (8) Macor Body, (9) Spring Plate (*not to scale*).

2
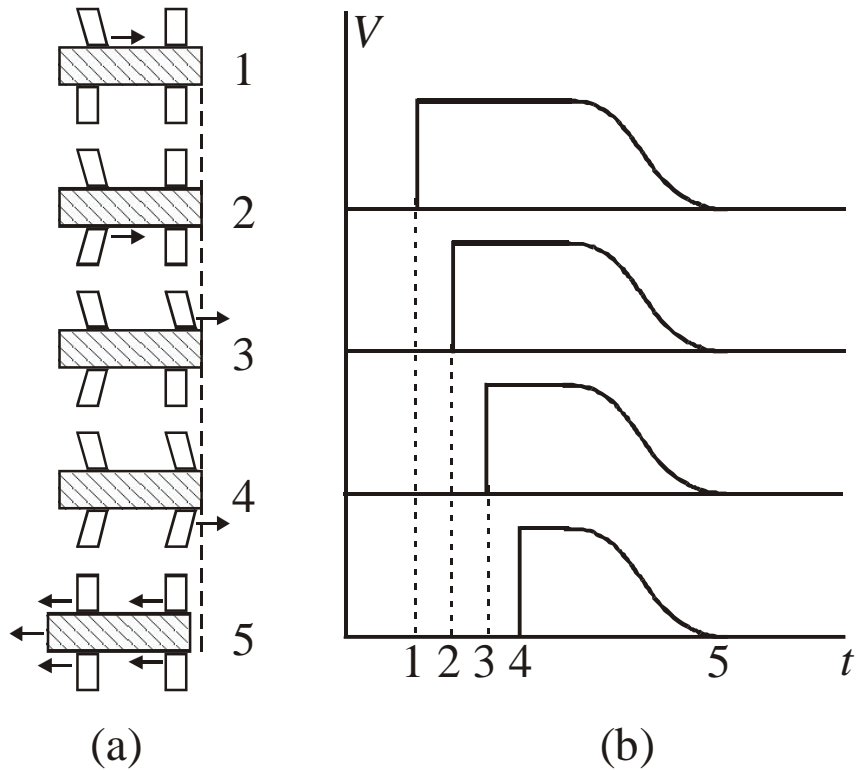
Figure 1.2. Schematic illustration of the working principle of the piezo coarse approach motor. (a) The sequence of motions of shear piezo stacks and the sapphire prism. (b) The sequence of voltages applied to each piezo leg to produce the motions in (a).

machined from a single piece of Macor (a machinable ceramic[1]). On top of the body is a spring loaded sample receptacle (1) machined from brass, which makes strong electrical and thermal contact to the sample holder (2), and thus to the sample, when it is loaded from above. The coarse-approach mechanism is a piezo actuated motor that consists of the main body (8), a spring press-plate (9), six shear-piezo stacks[2] with ceramic contact-pads[3] glued on top (7), and a prism-shaped sapphire shaft[4] (6) with a hole in the center.

Such a coarse approach motor has been described in detail elsewhere (Pan 1993). The schematic drawing in Fig. 1.2 briefly illustrates its working principle. Four piezo legs hold a moving shaft in position. When a voltage is applied to one leg, it slides backward (to the right) along the surface of the shaft, as friction between the other three legs and the shaft holds the shaft stationary. After an appropriate delay, the same voltage is applied to one of the other piezo legs. Once again, the shaft does not move while this second leg slides backward along the sapphire surface. After all the legs have been sequentially and independently slid backwards, the voltages on all legs are ramped down

[1] Manufactured by Corning Incorporated, purchased from Ceramic Products.
[2] Four layers of 0.0197" thick EBL 4 (=PZT 8) with nickel electrodes, distributed by Staveley Sensors.
[3] 0.020" thick, Superstrate/Hirel grade, manufactured by Coors Ceramic Company.
[4] Purchased from Gebrüder Wild Edelsteine.

simultaneously, as shown in the drawing. Consequently, all the legs together carry the shaft one step forward (to the left).

This design has been proven to have some unique features which are suitable for use in very low temperature scanning probe instruments (Pan unpublished, Behler 1993). Most importantly, the motor is very reliable, with reproducible step sizes[5]. Secondly, since motion is constrained to lie along the z-axis, relocating a portion of the surface after withdrawing the tip, which is necessary, for example, when transferring liquid He or ramping the magnetic field, becomes possible. In fact, we have repeatedly withdrawn the tip by about half a millimeter and reapproached to find in plane displacements of only 100 Å. In addition, since the motor does not rely on inertia, it can be operated in a vertical direction with minimal step-size differences due to gravity. This is an important feature as it allows a compact design suitable for use in the most common top loading refrigerators and in small bore, high field, solenoid magnets. Furthermore, the piezo legs constantly clamp the moving shaft and no voltage is required to keep the shaft in position while it is stationary. Thus the entire structure is rigid and stable.

After bringing the tip within several hundred Angstroms of the surface with use of the coarse approach motor, fine control of the tip position is achieved via a tube scanner. As shown in Fig. 1.1, this 1/8" diameter piezo tube-scanner[6] (4) is glued with epoxy[7] onto the scanner-holder (5), which is also machined from Macor. This assembly is then mounted into the hole in the sapphire prism (6). The assembly of (4) and (5) can easily be changed to obtain various scan ranges. The tip holder in our design is a fine metal tube glued into a ceramic tube[8] and then glued on top of the tube scanner. The tip (3) is held in the fine tube simply by friction. The design of the STM head is simple and compact. It has a dimensions of 1.75" in height and 1.5" in diameter.

1.2.2. Refrigeration

The refrigeration scheme used in this setup is a specially designed, low noise, single shot, ^{3}He sorption refrigerator. As shown in the schematic drawing of Fig. 1.3, the refrigerator is housed in a vacuum can (9) which is immersed in a liquid helium bath inside a superinsulated dewar[9]. The small (4.5 inch diameter) but long (3 ft.) neck of the dewar reduces the boil-off rate of the liquid helium to about 4 l a day (with the superconducting magnet installed) and thus also reduces vibrations due to evaporation of the liquid ^{4}He in the bath. A 700 l/min rotary pump[10] is used to pump on the ^{4}He pot to achieve a temperature of 1.2 K at the ^{4}He stage. This temperature will condense the ^{3}He gas into about 10 cc of liquid in the ^{3}He pot. An activated charcoal pump (7), when

---

[5] The piezo motor in our STM head has a step size of about 2000 Å at room temperature and about 300 Å at temperatures below 4 K, when driven with a peak voltage of 300 V. One can easily vary the step size by changing the applied voltage.

[6] EBL 4 (= PZT 8), with nickel electrodes, purchased from Staveley Sensors.

[7] For this and other non-conducting glue joints we use Torrseal, purchased from Varian Vacuum Products.

[8] Ceramic #31478, 1 mm OD, 0.5 mm ID, purchased from Alfa Aesar.

[9] Manufactured by Kadel Engineering.

[10] SD-700, manufactured by Varian Vacuum Products.
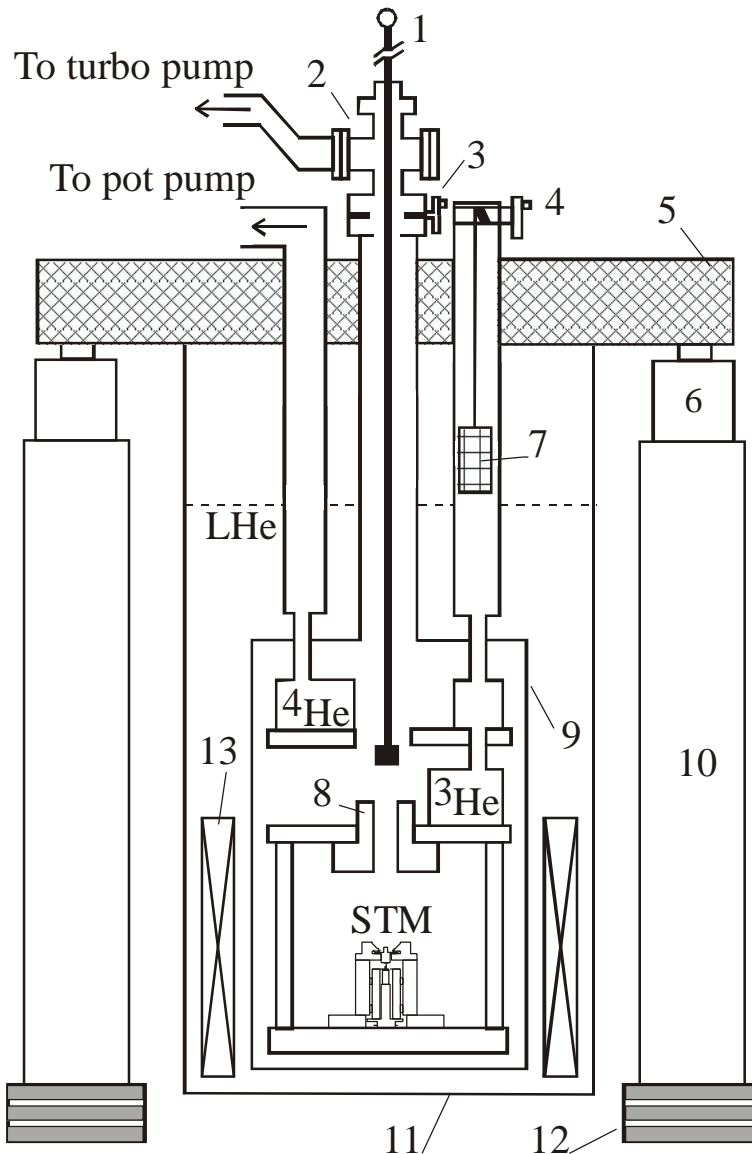
Figure 1.3. STM cryostat and vibration-isolation table. (1) Manipulator rod, (2) Load-lock chamber, (3) Gate-valve, (4) Charcoal sorption pump lift/lowering mechanism, (5) Table top of the vibration-isolation table, (6) Air-spring, (7) Activated charcoal sorption pump, (8) Mechanical sample cleavage stage, (9) Vacuum chamber, (10) Supporting leg, (11) Superinsulation dewar, (12) Stacked rubber and steel pads, (13) 7.25 T Magnet (*not to scale*).

lowered into the 4.2 K region by a lift mechanism[11] (4), pumps on the condensed ^{3}He to achieve a base temperature of 220 mK at the ^{3}He stage. To achieve this temperature, all mechanical and electrical connections from room temperature must be minimized and carefully heat-sunk. Radiation from room temperature is also carefully baffled. With these measures, 10 cc condensed ^{3}He can keep the refrigerator at 220 mK for about 3 to 4

---

[11] Design concept by R.E. Packard.

days before recondensation is required. We can cool the STM from room temperature down to its base temperature in less than 36 hours[12].

1.2.3. Thermometry

At the STM head we reach a base temperature of 237 mK. A commercially calibrated Cernox thermometer[13] is attached to the sample receptacle to ensure accurate measurement of the sample temperature. Since the sample surface faces inwards, we believe that it reaches the equilibrium temperature of the sample receptacle as measured by the calibrated Cernox thermometer. We have verified that the STM tip also cools to this temperature by fitting tunneling spectra from a superconducting Nb tip to BCS theory (Pan 1998B), which will be discussed in depth in chapter 3. All thermometers are carefully thermally anchored to the measuring points and operated with low current, low frequency AC bridge circuits, thus avoiding self-heating. We also fastened a resistive heater on the base plate of the STM to vary the base temperature when needed. The operation of the refrigerator is rather simple and straightforward.

1.2.4. Superconducting Magnet

A 7.25 T superconducting solenoid with 4.5" bore[14] is installed in the bottom of the ^{4}He dewar and surrounds the stainless steel vacuum can of the refrigerator. The sample receptacle on the STM head is located at the center of the homogeneous (0.1 % over 1 cm DSV) region of the magnetic field. The two current leads of the superconducting magnet are detachable. When the magnetic field is stabilized at the desired field strength and set in persistent mode, the current leads are detached from the magnet and raised to the top of the dewar to reduce the ^{4}He boil-off. With such an arrangement, the entire system has a ^{4}He boil-off rate[15] of about 5 l per day. Hence, the 16 l capacity of the dewar gives about 3 days of operation, matching the length of the continuous operation time of the ^{3}He fridge for a single shot. All materials used in the refrigerator and STM head are nonmagnetic. We have successfully operated the STM at the maximum field of 7.25 T.

1.2.5. Vacuum System and Sample Manipulator

A 60 l/s turbo pump[16] pumps our 4 l stainless steel vacuum can (4" in diameter by 21" long) via a load-lock chamber (2) (a 4-way cross), a gate valve (3), and a 5/8"

---

[12] We pump on the vacuum can overnight (12 hours), transfer liquid nitrogen and cool to 77 K the next morning (6 hours), and transfer liquid helium and cool to 4.2 K that evening (12 hours). When starting the fridge the next morning we can condense the ^{3}He in about 1 hour and then stabilize at 250 mK about an hour after starting the fridge.

[13] Manufactured by Lakeshore Cryogenics.

[14] AMI Job #5924, Magnet #3114, model A7045-3, manufactured by American Magnetics.

[15] The He level in the dewar is measured with a 241 Liquid Helium Level Monitor, manufactured by Lakeshore Cryogenics. The sensor is mounted above the vacuum can flange, and the liquid level is not allowed to fall below this level.

[16] TMU 065, backed by MVP 012 diaphragm pump, manufactured by Balzers.

diameter, 40" long, stainless steel tube. The vacuum has been measured[17] at the load-lock chamber as 4 x 10^{-6} Torr at room temperature after 12 hours of pumping without baking. A 6 ft long manipulator rod (1) that passes through a custom-built, differentially-pumped double o-ring feed-thru allows us to transfer samples from room temperature down to the STM which remains at low temperatures. Such an arrangement not only greatly reduces experimental turn around time, but also enables us to utilize the UHV conditions at very low temperatures for *in situ* tip cleaning by field-emission and sample cleavage. A mechanical sample cleavage stage (8) is directly mounted on the ^{3}He refrigerator for cleaving samples at low temperatures.

1.2.6. Vibration Isolation

Early tests showed that our STM head is very rigid and that our charcoal pump based refrigerator is vibrationally quiet. Hence, we did not need to use the originally designed low temperature vibration-isolation stage (Hudson 1996). Instead, we have bolted the STM to a solid frame, made of OFHC copper and plated with gold, that directly extends from the coldest stage of the fridge. This frame supports the STM head vertically, with the sample receptacle facing upward for top-loading of samples. Eliminating the vibration isolation between the STM and the refrigerator greatly simplifies the arrangement of thermal and electrical connections.

Thus, all vibration-isolation is external and at room temperature. As depicted in Fig. 1.3, the refrigerator is mounted below a custom built vibration-isolation table, of the same general design commonly used for millikelvin cryostats. The triangular tabletop (5) is filled with lead shot (weighing about 1000 pounds) and sits on top of three commercial air springs[18]. Three legs filled with concrete support the air springs to elevate the refrigerator to a height where one can comfortably work on the STM. Beneath these legs, rubber and steel pads are stacked to serve as a first vibration damper. The entire system is housed in an acoustic-isolation room and all control electronics are placed in an adjacent room to avoid vibrational noise from cooling fans and movement of the operators. All mechanical pumps are located in a separate basement, except for the turbo pump. During STM operation, the gate valve above the vacuum chamber is closed and the turbo pump is turned off. Cryogenic temperatures guarantee maintenance of good vacuum in the vacuum chamber.

1.2.7. Control Electronics

Our STM control electronics were purchased from Topometrix Inc[19]. This DSP-based feedback control system operates at 100 kHz, with three 16 bit ADC's (one which continuously monitors the current from our current amplifier, and two which are used for

---

[17] Pressure measurement at the load lock performed with a Compact Full Range Gauge PKR-250 controlled by a SingleGauge controller, both manufactured by Balzers.

[18] Manufactured by the Technical Manufacturing Corporation (TMC).

[19] Topometrix recently merged with Park Instruments to form ThermoMicroscopes. We purchased this system for its versatility (they provide full electronic schematics and source code) and for the local support (they are based in Sunnyvale, just an hour's drive south).
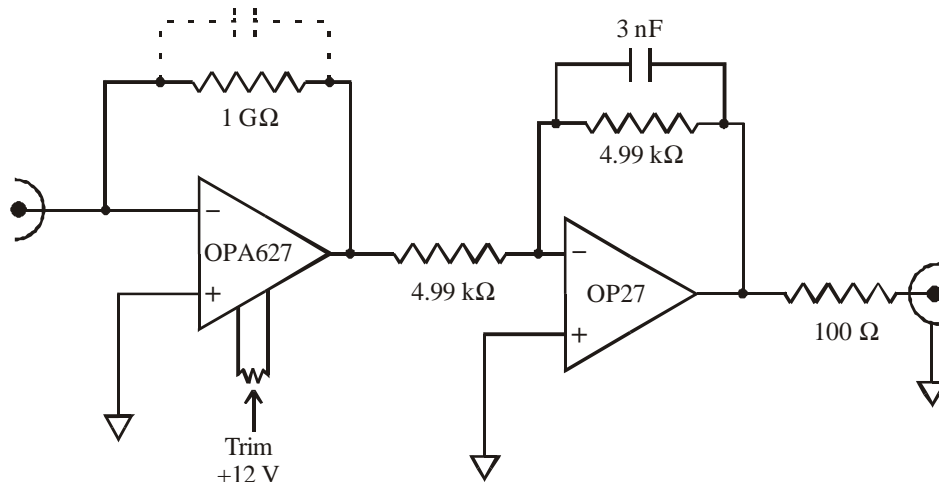
Figure 1.4. Schematic of our current amplifier. The 1 GΩ resistor is from Eltec Industries, and is used for its low shunt capacitance and low noise (near the k_BT threshold). The OPA627 from Burr Brown is a low noise op amp, with good current noise characteristics (30 fA_{pp} from 0.1 – 10 Hz and 2 $fA/\sqrt{Hz}$ at 100 Hz) and an input bias current of less than 1 pA. The signal is intentionally filtered at 10 kHz, but provides an effective bandwidth of about 3 kHz.

additional inputs, such as output from our lock-in amplifier), five 16 bit scan DAC's with high voltage amplifiers (which supply between ± 220 V to drive the tube scanner), and a 16 bit DAC which provides ± 10 V for sample bias. The system also comes equipped with additional inputs to allow the addition of voltage modulations to both the bias (used for dI/dV measurements) and Z-piezo outputs, as well as with multiple digital IO ports, which we use to trigger our walker controller.

The system required some modification of both the electronics interface and the software. The original electronics interface consisted of three multi-pin connectors, for easy connection to the company's various instruments. We replaced these with BNC connectors for all signals, and included frequency selectable filters for the scanner signals (which we usually set at 3 kHz, but occasionally set as low as 10 Hz for highly sensitive spectroscopic measurements). Additionally, we insert a divider (by 10 or by 100) into the sample bias line at the fridge top (which increases the energy resolution to approximately 30 μV or 3 μV respectively). The software also required modifications, including the use of logarithmic feedback, a modified tip approach method, and various changes to data collection routines, some of which will be detailed in appendix A.

1.3.2. Current Amplifier

We use two different current amplifiers with our STM, depending on the status of the experiment. While performing field emission, we use a commercial amplifier[20], which has the benefits of variable gain (10^4 to 10^9 V/A) and overvoltage and overcurrent protection. For all other purposes we use a custom built amplifier, a schematic of which is provided in Fig. 1.4. This two-stage amplifier (I/V Converter) has a fixed gain of 1

---

[20] A 1212 current amplifier, manufactured by Ithaco and distributed by D.L. Instruments.

mV/pA and an effective bandwidth of approximately 3 kHz. Noise at the output is about 4 mV$_{pp}$ (equivalent to 4 pA$_{pp}$). The amplifier is mounted directly to the vacuum feedthru on top of the cryostat, and obtains DC power (regulated down to 12 V from 15 V) from the STM controller to reduce problems of ground loops.

1.3. STM Operation

For the remainder of this chapter I will provide an introduction to STM and discuss some of the techniques used in our STM work. In the next chapter I will show examples of the application of some of these techniques to the conventional superconductor NbSe$_2$, both to illustrate these methods and to demonstrate the operating condition of our instrument. More specific details of operation (such as outlines of data collection routines) will be presented in appendix A.

1.3.1. Theory of Scanning Tunneling Microscopy

A scanning tunneling microscope simply consists of a sharp tip (a piece of wire), which is brought within several Angstroms of a sample surface, and moved with respect to that surface. The tip and sample, both electrical conductors, have a bias voltage applied between them, which results in a measurable current tunneling through the vacuum that separates them. Although detailed models of imaging and spectroscopy with an STM are necessarily complex, I will present only a very straightforward theory of tunneling, first proposed by Bardeen (1960) and applied to STM by Tersoff and Hamann
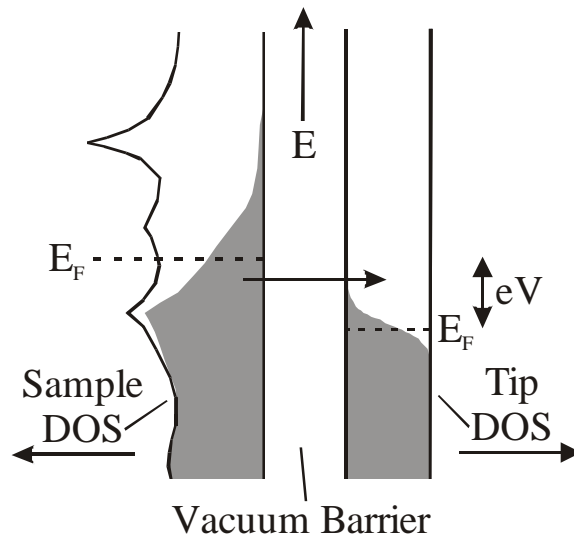
Figure 1.5. Schematic of tunneling from sample to tip. The Fermi energies of the sample and tip, originally in coincidence when the systems are brought near contact, are separated by an energy eV due to the application of a sample bias voltage V ($V < 0$ in the case pictured here). This allows electrons to tunnel elastically through the vacuum barrier separating the two, leading to a detectable current. The magnitude of this current depends on the density of states of both tip and sample, on the distance between them, on the voltage applied, and on the amount of thermal broadening (as pictured here by the shaded filled states, obtained by multiplying the density of states by the Fermi function).

9

(1983,1985) soon after the invention of scanning tunneling microscopy (Binnig 1982a & 1982b).

In the Bardeen model of tunneling, the tip and sample are treated as two separate systems, each with their own local density of states (DOS), which lightly overlap. Time dependent perturbation theory can then be used to calculate the rate of electron transfer between the two systems. If energy is conserved in the tunneling process (elastic tunneling), then the tunneling current depends on the DOS of each subsystem in a logical fashion:

$$I = I_{sample \to tip} - I_{tip \to sample}$$

$$= \frac{4\pi e}{\hbar} \int_{-\infty}^{\infty} |M|^2 \, r_s(E_s) r_t(E_t) \{ f(E_s)[1 - f(E_t)] - f(E_t)[1 - f(E_s)] \} de \tag{1.1}$$

where e is the charge on an electron, $\hbar$ is Planck's constant, |M| is the matrix element for tunneling, r is the density of states (of the sample s or the tip t), and f is the Fermi function: $f(E) = \{1 + \exp[(E - E_F)/k_B T]\}^{-1}$ (E_F is the Fermi energy, k_B is Boltzmann's constant and T is the temperature). Thus the current depends on the probability of a full state existing for the electrons to tunnel out of and an empty state existing for them to tunnel into.

As mentioned, the tunneling process is assumed to be elastic, so E_s and E_t must describe states of equal energy. However, when written with respect to the Fermi energies of their respective systems (each set to 0), which are separated due to an applied sample bias voltage V, these energies become $E_s = e - eV$ and $E_t = e$ (see Fig. 1.5). Thus, the tunneling current becomes:

$$I = \frac{4\pi e}{\hbar} \int_{-\infty}^{\infty} |M|^2 \, r_s(e - eV) r_t(e)[f(e - eV) - f(e)] de \tag{1.2}$$

1.3.2. Constant Current Topography

With an understanding of the current flow between sample and tip, each of several modes of operation of the STM can now be described. Perhaps the most common mode of operation for a scanning tunneling microscope is that of constant current topography. Here, as shown in Fig. 1.6, a feedback loop is used to keep a constant current flow as the tip is scanned back and forth across the sample. The topographic nature of this measurement relies on an important fact about the tunneling matrix element – its magnitude depends exponentially on the tip-sample separation s:

$$|M|^2 \propto \exp\left(-2 \frac{\sqrt{2mj}}{\hbar} s\right) \approx \exp\left(-\sqrt{j \, (eV)} \, s(\text{Å})\right) \tag{1.3}$$

(in the approximation that $V \ll \phi$, where ϕ is the convoluted work function of the tip and sample). Thus, as the tunneling current depends exponentially on tip-sample separation, maintaining a constant current essentially keeps the tip a constant distance from the sample surface. As the work function ϕ is typically on the order of 4 eV, an increase in tip-sample separation of only 1 Å can decrease the current by a factor of $e^2 \sim 7.4$. Due to

Feedback
Control

$I \propto e^{-z/\,z_0}$

Amp

Data-Acquisition

Z

XY Scan Control

Y

X

Sample

Bias

Tip
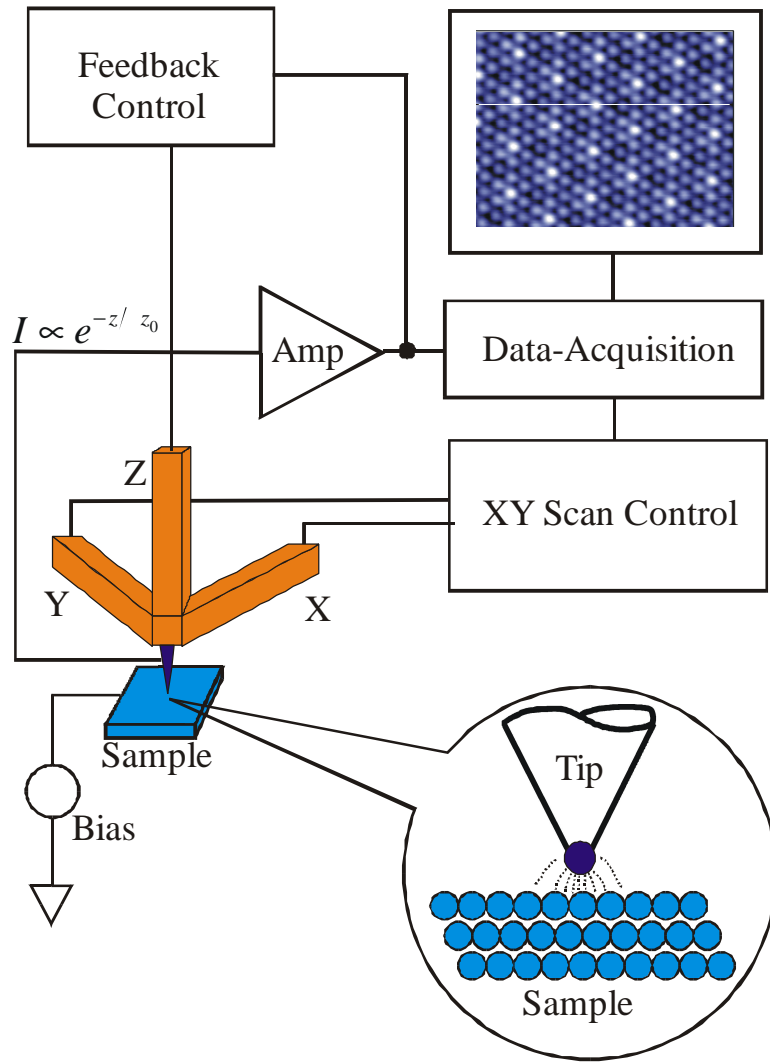
Sample

Figure 1.6. Schematic of operation of a scanning tunneling microscope. An atomically sharp tip is brought within a few Angstroms of an atomically flat surface. Feedback maintains the tip/sample separation by holding the tunneling current I constant.

this strong dependence, measurement of variations in the feedback voltage as a function of lateral position serve as high resolution topographic images of the surface.

1.3.3. Current vs. Tip/Sample Separation (log I vs. s)

The exponential dependence (eqn. 1.3) of the tunneling matrix element on both tip/sample separation and on the square root of the work function allows a second type of measurement to be made – log I vs. s spectroscopy. In this mode of operation, the current is recorded while the tip is slowly withdrawn several Angstroms from the sample surface. If the tunnel junction is a good, clean, vacuum barrier, then the current should fall exponentially with the displacement, and the slope of the line (on a log-linear plot)

should reveal the convoluted work function for the tip-sample system (e.g. Coombs 1986, Garcia 1986):

$$f[\text{eV}] = \frac{\hbar^2}{8m}\left(\frac{d\ln I}{ds}\right)^2 \approx 0.95\left(\frac{d\ln I}{ds[\text{Å}]}\right)^2 \tag{1.4}$$

We always confirm clean vacuum tunneling with this technique at the outset of an experiment. The use of this measurement for characterization of a Nb tip is discussed in chapter 3.

1.3.4. Differential Conductance Spectroscopy

In addition to measuring the work function and topography, the STM also has the ability to measure a much more scientifically interesting property of the surface – the electronic density of states (DOS). The first demonstration of this measurement, referred to as scanning tunneling spectroscopy (STS), was by Stroscio et al. (1986) on Si(100). The ability to extract DOS information from the tunneling current may be easily seen by using eqn 1.2 with some simplifying assumptions. For small sample bias at constant tip/sample separation the tunneling matrix element can be considered a constant and removed from the integral, yielding:

$$I \propto \frac{4\pi e}{\hbar}\int_{-\infty}^{\infty} r_s(e-eV)r_t(e)\left[f(e-eV)-f(e)\right]de \tag{1.5}$$

With the further assumptions that the density of states of the tip is constant in the energy range of interest (which is true for properly chosen tip materials), and that the temperature is sufficiently low that the Fermi functions may be treated as step functions, we find:

$$I \propto \int_{-\infty}^{\infty} r_s(e-eV)\left[\theta(e-eV)-\theta(e)\right]de = \int_{0}^{eV} r_s(e-eV)de \tag{1.6}$$

Thus, the differential tunneling conductance, $G(V) = dI/dV|_V$, is simply proportional to the local density of states of the sample at $E = eV$.

We typically measure the differential tunneling conductance by setting the tip-sample separation, characterized by the junction resistance at a given sample bias, and then turning off feedback so that this separation is fixed. A small, sinusoidal voltage modulation is then applied to the bias voltage, and the resulting current modulation, as read by a lock-in amplifier attached to the output of the current amplifier, is proportional to the differential conductance. This can be seen using the Taylor expansion of the current:

$$I(V + dV\sin(wt)) \approx I(V) + \frac{dI}{dV}\bigg|_V \cdot dV\sin(wt) \tag{1.7}$$

At a given point on the surface, then, a differential conductance spectrum is obtained by recording the amplitude of the lock-in output, proportional to dI/dV (and hence indicative of the density of states), as a function of applied sample bias (energy).

1.3.5. Differential Conductance Mapping

A natural extension of the above technique is to measure lateral position dependence as well as energy dependence. In this case, rather than measuring the

conductance at a single position, it is measured at a series of points on the surface. At a given spatial position, the differential conductance at one or more energies is measured. Then, the tip is moved, using feedback as in topography mode, to the next position, at which point the feedback is once again disabled and the next conductance measurements are made. This mapping technique allows easy visualization of the evolution of the DOS with position, and its usage will be discussed in depth in chapters 5 and 6.

Chapter 2.

Tunneling and Superconductivity: Testing Our Scanning Tunneling Microscope

Our initial tests of the STM at both room temperature and low temperatures were performed on highly oriented pyrolytic graphite (HOPG)[21]. Further tests were then performed on 2H-NbSe$_2$[22], a well-studied material that has both charge density wave (CDW) and superconducting phase transitions at low temperatures, and is thus ideal for test and calibration. As it is a type II superconductor, a moderate magnetic field (0-3 T) produces a vortex lattice which can be imaged to test operation in a magnetic field. I will discuss measurements of each of these phenomena in this chapter.

a = 3.45 Å
c = 12.54 Å

u = 1.68 Å

Se
Nb
Se
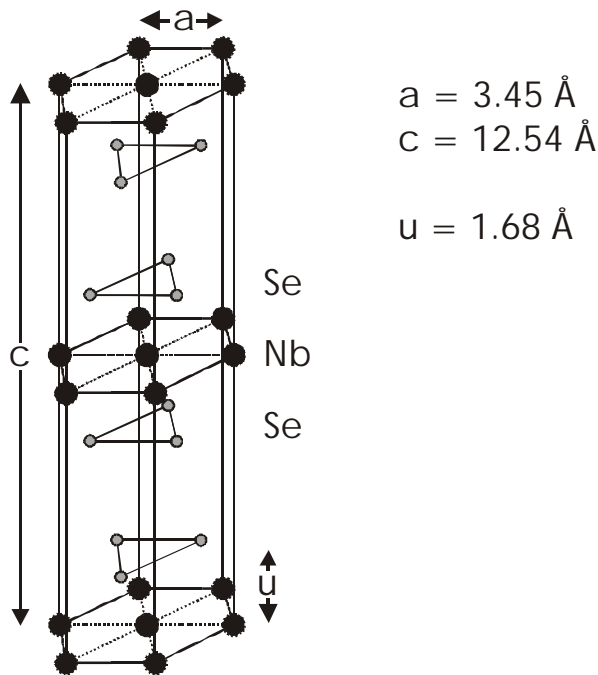
Figure 2.1. Schematic diagram of a unit cell of NbSe$_2$ (2H phase). The material cleaves easily between adjacent Se planes, revealing a hexagonal lattice of Se atoms with a nearest neighbor distance of 3.45 Å.

---

[21] Purchased from Union Carbide.
[22] Generously provided by Prof. Alex Zettl.

2.1. Topography: Charge Density Wave

As mentioned in the previous chapter, a common mode of operation for a scanning tunneling microscope is that of constant current topography mode. In Fig. 2.2, I show a constant current image of $NbSe_2$ at a temperature of 240 mK. Both the atomic corrugation and a charge density wave modulation are clearly resolved. Below the image, a line-profile, position-marked with a white line on the image, shows that the noise level is on the order of 0.5 pm. This is consistent with the noise on our high voltage amplifiers for the scan piezo. Unless otherwise noted, all topography shown in
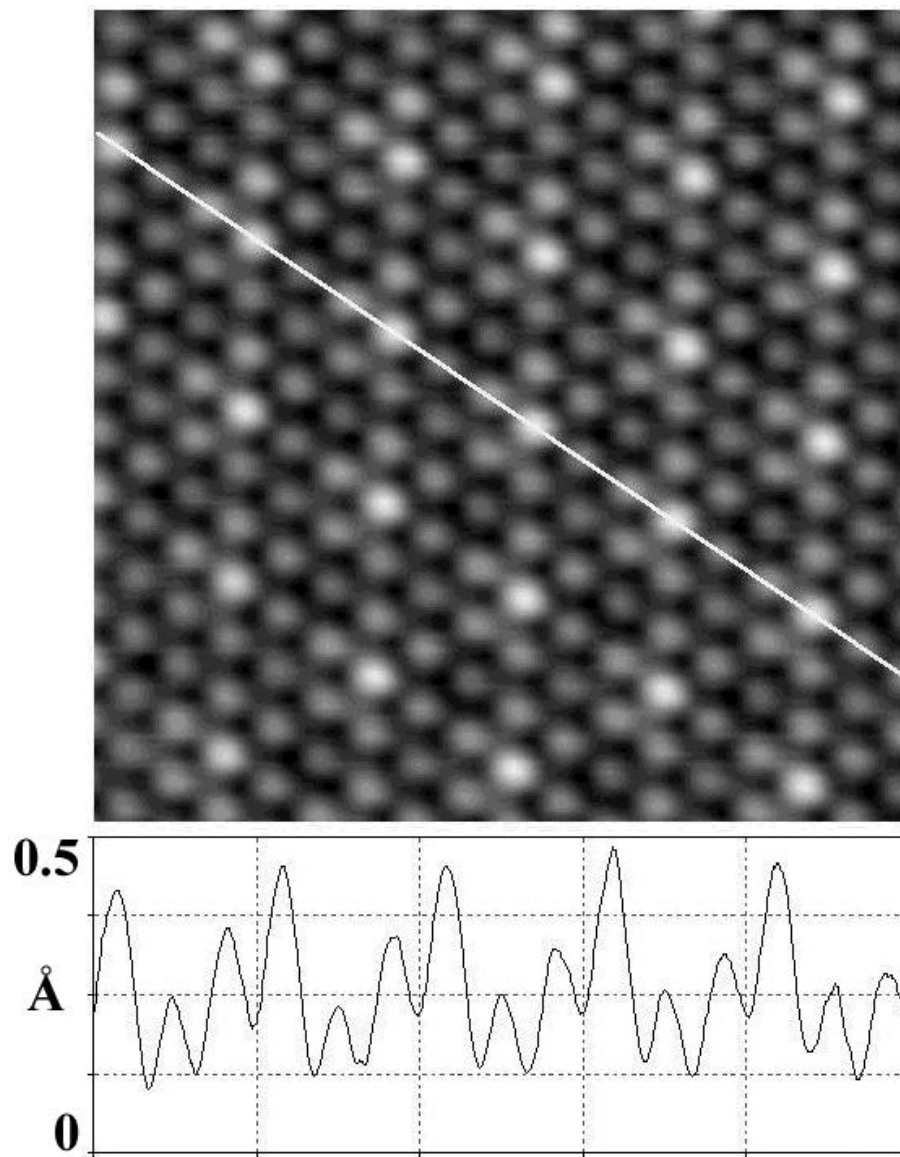
Figure 2.2. Constant current image on $NbSe_2$ at 240 mK. (I = 50 pA, V_{sample} = -50 mV, 50 Å scan range). Below the image, a line-profile, whose position is marked with a white line on the image, shows the apparent atomic corrugation and CDW modulation.
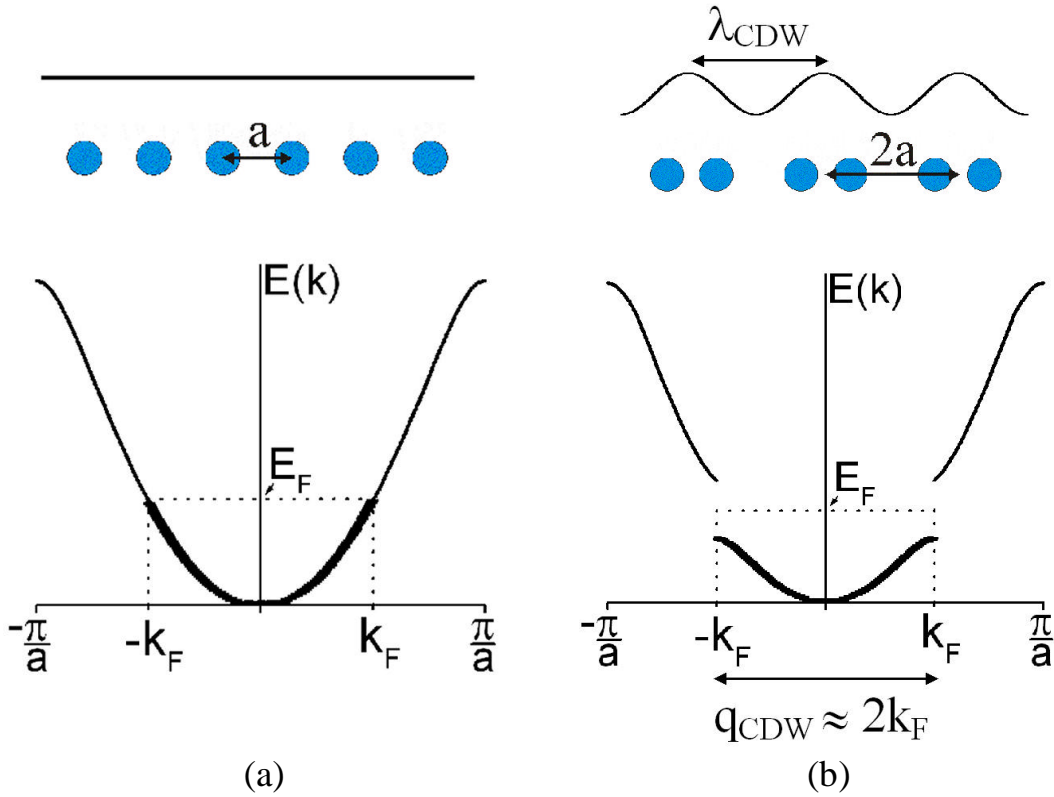
Figure 2.3. Overview of charge density waves, as demonstrated in a one-dimensional material at half filling. The lattice begins, as shown in **a**, uniformly spaced (lattice constant *a*) with a nearly uniform charge density (as indicated by the flat line above the lattice).

If, as shown in **b**, a periodic lattice distortion occurs, inducing a charge density modulation with wave vector $q_{CDW} \approx 2k_F$ ($2\pi/2a$ in this example), then a gap opens about the Fermi energy, reducing the energy of the filled electron states (darkly shaded portion of the dispersion relation).

this thesis is original and unfiltered (the only image processing employed is plane subtraction leveling).

As noted above, a second charge density modulation is observed in addition to the atomic one – every third atom appears brighter than the rest. This is due to the presence of a charge density wave in the material. Charge density waves (CDW's) are perhaps most easily understood by studying the one-dimensional model proposed by Peierls (1955, pp. 101-14)[23]. Figure 2.3 shows a schematic representation of his argument. A one dimensional chain of atoms, with lattice spacing *a*, has a dispersion relation as pictured in Fig. 2.3a. In the case of half-filling, electrons will occupy those states shaded darkly, out to the Fermi wave vector k_F (half the Brillouin zone). The electronic energy of this system can be significantly reduced, however, if the edge of the Brillouin zone were to be brought into coincidence with the Fermi wave vector (in this case, if it were cut in half). This can occur, as pictured in Fig. 2.3b, if every other atom in the chain is

---

[23] Overhauser (1978) also provides a nice introduction to charge density waves.

displaced slightly from its equilibrium position. In that case, the unit cell is doubled (now with lattice constant $2a$) and the Brillouin zone is halved. The gap that opens at the edge of the Brillouin zone now has the effect of significantly lowering the energies of the occupied states (and raising the energies of the unoccupied states), thus reducing the overall energy of the system[24].

Charge density waves can in general form in any system where the presence of a periodic lattice distortion, which costs potential energy, leads to a more than offsetting reduction of the electronic energy by opening a gap at the Fermi energy. As there is a strong relationship between the wave vector of the charge density wave q_{CDW} and the Fermi wave vector k_F ($q_{CDW} \sim 2\,k_F$), CDW's occur most often in materials whose Fermi surfaces are nested, that is, whose Fermi surfaces have fairly flat, parallel portions. In these cases a single CDW wave vector can gap more of the Fermi surface, and thus produce a larger energy reduction.

Figure 2.3b indicates three methods of observing the existence of a charge density wave. First of all, the CDW is accompanied by a periodic lattice distortion. However, the magnitude of this distortion is frequently quite small, and difficult to observe by STM.[25] The second method of observation is the one which introduced this section – the presence of the charge density modulation itself[26]. In NbSe$_2$, this modulation is clear, and enables us to make a direct measurement of the wave vectors associated with the CDW. An FFT of the topography of Fig 2.4a, shown in Fig. 2.4b, allows easy identification of the CDW wave vectors, which can then be plotted on a Fermi surface map in an attempt to identify which portions of the Fermi surface take part in the excitation. The Fermi surface of NbSe$_2$ is shown in Fig. 2.4c, and the nested portions of the hole sheet clearly match our observed CDW wave vectors.

The final method of CDW observation, as shown in Fig. 2.3b, is the presence of a gap in the density of states. Such a gap may be measured directly by tunneling spectroscopy, as will be discussed in the next section.

2.2. Tunneling Spectroscopy: Measuring Gaps

As mentioned in chapter 1, STM techniques allow not only the imaging of topography with atomic resolution, but also simultaneous measurement of the local density of states (LDOS) at the surface.

---

[24] For a review of weak periodic potentials see Kittel 1986, pp. 160-3 and Ashcroft 1976, pp. 152-9.
[25] X-ray and neutron scattering are sensitive to periodic lattice distortions, but due to the small magnitude of these distortions in CDW's, it is not uncommon that they will be missed by these techniques as well.
[26] The details of the appearance of a CDW in STM topography are a topic of great interest, for example in the magnitude and energy dependence of the features. See, for example, Kikuchi (1995).

(a)

(b)

(c)
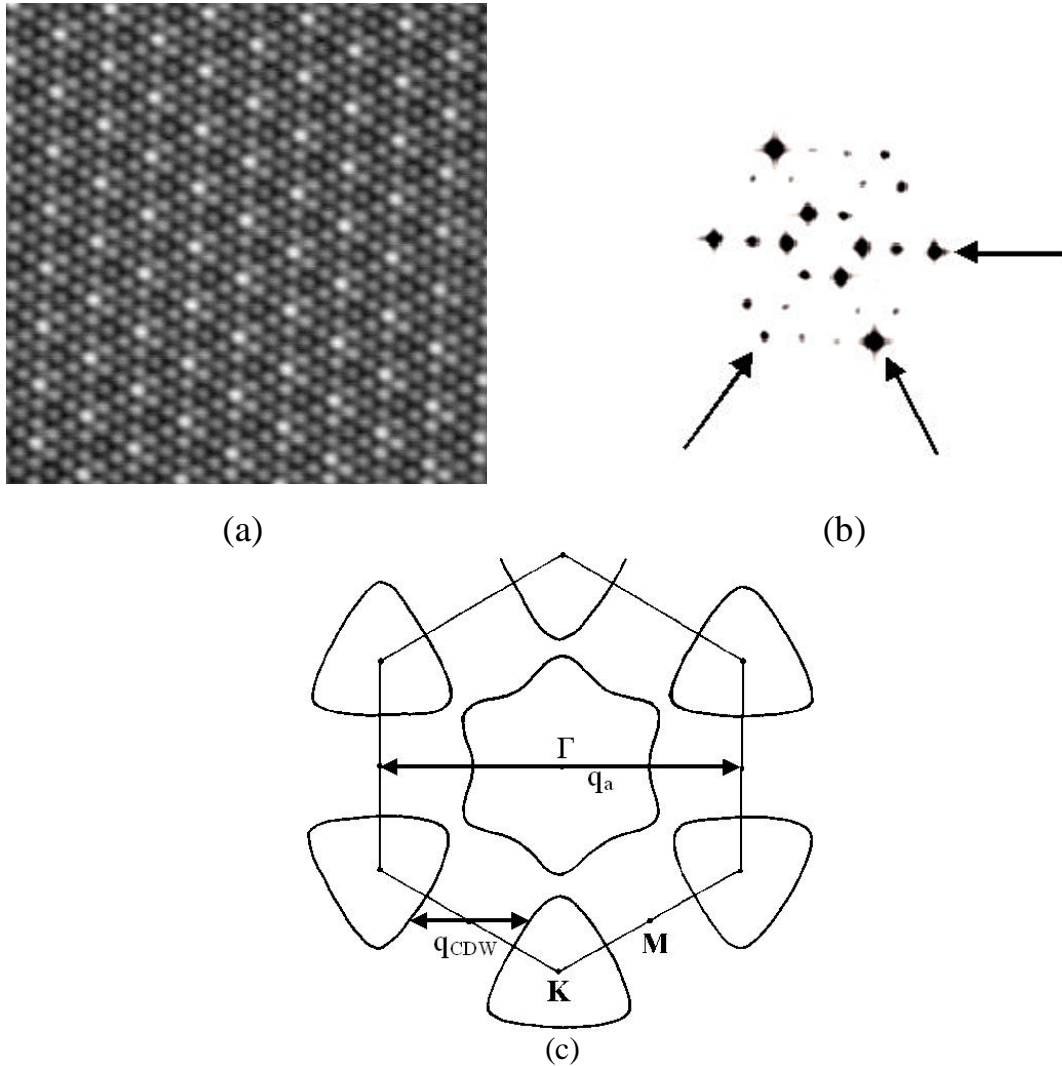
Figure 2.4. **a.** High resolution topography on NbSe$_2$ at 240 mK, of a larger area than that shown in Fig. 2.2. (I = 50 pA, V$_{sample}$ = -50 mV, 100 Å scan range).
b. FFT of the image shown in (a). The three arrows point along the reciprocal lattice directions (perpendicular to lines of atoms in (a)). The three spectral peaks at the heads of the arrows (and those reciprocated across the center) comprise the atomic lattice. Along the same directions, at one-third of the wave vector, (three times the wavelength) are spectral peaks corresponding to the CDW wave vectors.
c. The Fermi surface of NbSe$_2$, with one reciprocal lattice vector q_a and one CDW wave vector q_{CDW} superimposed. Note that q_{CDW} connects nested portions of the hole sheet of the Fermi surface (Williams 1976, Wilson 1975).

2.2.1. Charge Density Wave Gap

Figure 2.5 shows an example of such spectroscopy on this material. The opening of a gap at the portions of the Fermi surface indicated in Fig. 2.4b leads to a dip in the total density of states, and thus to a drop in the tunneling conductance in the "energy gap," the edges of which are indicated by arrows in Fig. 2.5. In addition to this CDW

gap, however, a much stronger feature is observed at lower energies (closer to the Fermi energy, or $V_{sample} = 0$). As this feature is associated with the superconductivity in this material, I will briefly review tunneling into superconductors before returning to high resolution spectroscopy.

2.2.2. Tunneling into Superconductors

As discussed in the previous chapter, the tunneling current between two electrodes depends on the density of states of both. When one of the electrodes is assumed to be "ideally metallic," the differential conductance reduces approximately to a measurement of the density of states of the other. For this reason tunneling was very successful in verifying BCS theory predictions (Bardeen 1957) of the quasiparticle excitation spectrum of superconductors (Giaever 1961).

Tunneling into a superconducting sample is slightly different than tunneling into a metallic sample, and thus bears some investigation. As understood within the framework of BCS theory, all Cooper pairs of electrons condense into a single, low energy state. In this state, the equivalent single electron energy or "many-body energy of one electron," defined as the total energy of the state divided by the number of electrons, is equal to the Fermi energy E_F. Lying at energies above this ground state (separated by the superconducting gap energy D) are the excited quasiparticle states. For a given wave
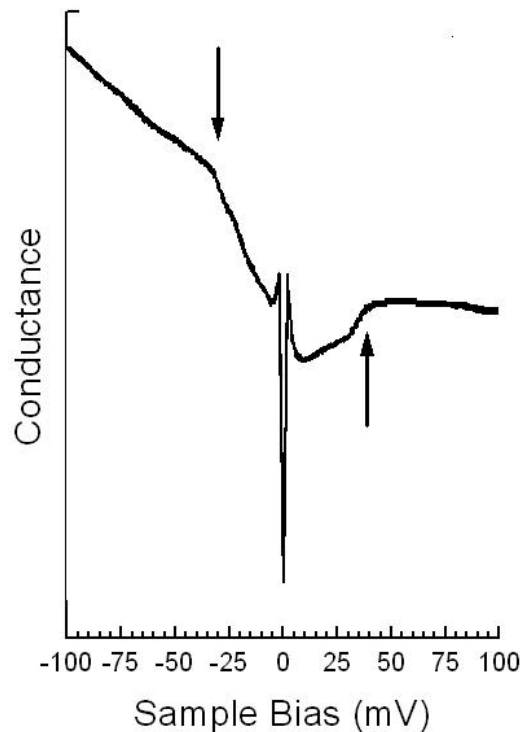
Figure 2.5. Differential tunneling conductance of NbSe$_2$ at 4.2 K. As we are below the CDW transition temperature ($T_{CDW} = 33$ K), a gap has opened around the Fermi energy ($\Delta \approx 35$ mV), as indicated by the arrows. The narrower, deeper gap is the superconducting gap, and is shown in more detail in Fig. 2.7.

20

vector $\mathbf{k}$, the energy $E_{\mathbf{k}}$ of these quasiparticle states is given in BCS theory as $E_{\mathbf{k}} = \sqrt{x_{\mathbf{k}}^2 + \Delta_{\mathbf{k}}^2}$, where the gap energy Δ can in general vary with $\mathbf{k}$ as well, but is assumed to be constant in the original BCS derivation. In addition to the effective potential energy of the gap, excited quasiparticles also have a kinetic energy $x_{\mathbf{k}} = \hbar^2 \mathbf{k}^2 / 2m - E_F$.

For large kinetic energies the gap becomes irrelevant, and the quasiparticle energy spectrum returns to the excitation spectrum of the normal state. Thus, using the fact that no states are generated or lost when the system undergoes the phase transition into its superconducting state, at energies close to E_F the superconducting density of states D_S can be related directly to the normal state DOS at the Fermi Energy $D_N(E_F)$: $D_S(E_{\mathbf{k}})dE_{\mathbf{k}} = D_N(x_{\mathbf{k}})dx_{\mathbf{k}} \approx D_N(E_F)dx_{\mathbf{k}}$. Thus the density of quasiparticle states for a BCS superconductor is given by:

$$\frac{D_S(E_{\mathbf{k}})}{D_N(E_F)} = \frac{dx_{\mathbf{k}}}{dE_{\mathbf{k}}} = \begin{cases} \dfrac{E_{\mathbf{k}}}{\sqrt{E_{\mathbf{k}}^2 - \Delta^2}} & E_{\mathbf{k}} > \Delta \\ 0 & E_{\mathbf{k}} < \Delta \end{cases} \tag{2.1}$$

One important fact to note is that although electrons can be added these states with a minimum energy of $E_F + \mathbf{D}$, they can only be removed from the ground state if a Cooper pair is broken, requiring a total energy of 2Δ (both electrons of the Cooper pair must in general be excited into the unoccupied quasiparticle states lying above the ground state). This asymmetry between tunneling into and out of a superconductor is displayed in Fig. 2.6. As can be seen, when tunneling into a superconductor ($V_{sample} > 0$) the electrons can flow directly into unoccupied quasiparticle states. For tunneling in the

(a) Injection ($V_{sample} > 0$)   **(b) Extraction ($V_{sample} < 0$)**
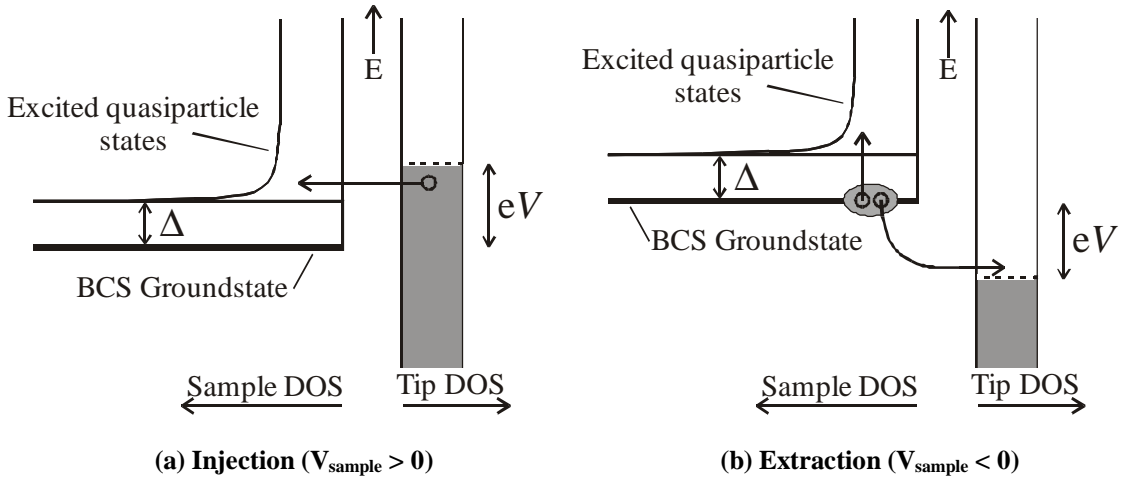
Figure 2.6. Tunneling between an ideal metal tip and a superconducting sample. In (a), electrons from filled states in the normal metal tip are injected into unoccupied quasiparticle states in the superconducting sample. In (b), Cooper pairs in the sample are broken to extract a single electron into the tip, while the other quasiparticle of the pair is simultaneously excited. In both cases the tunneling is elastic, and thus no current flows until $|V_{sample}| > \Delta$.

opposite direction ($V_{sample} < 0$), however, a Cooper pair must be broken. In order to conserve energy, the electron which is extracted from the system must drop an energy equal to the amount of energy required to boost the remaining quasiparticle into the unoccupied quasiparticle states. After the dust settles, however, these two processes yield identical tunneling currents. Thus the picture is typically simplified by stating the existence of a symmetric density of quasiparticle states in the superconductor, $D_S(E) = D_S(|E|)$, and using the tunneling formula derived in chapter 1:

$$I = \frac{4\pi e}{\hbar} \int_{-\infty}^{\infty} |M|^2 \, D_s(e - eV) D_t(e) [f(e - eV) - f(e)] de$$

$$\propto \int_{-\infty}^{\infty} D_s(e - eV)[f(e - eV) - f(e)] de$$

$$= \int_{-\infty}^{\infty} D_s(e)[f(e) - f(e + eV)] de \qquad (2.2)$$

$$= \int_{-\infty}^{\infty} \frac{|e|}{\sqrt{e^2 + \Delta^2}} [f(e) - f(e + eV)] de$$

$$\Rightarrow \frac{dI}{dV} \propto \int_{-\infty}^{-\Delta} + \int_{\Delta}^{\infty} \frac{|e|}{\sqrt{e^2 + \Delta^2}} \left[\frac{-d}{dV} f(e + eV) \right] de$$

This can be numerically integrated to calculate the "BCS differential tunneling conductance" as a function of temperature. At low enough temperatures, the Fermi function can be treated as a step function, and hence its derivative as a δ-function, reducing the differential conductance to exactly the BCS DOS.

2.2.3. Superconducting Energy Gap and Anisotropy

With the relationship between tunneling conductance and the superconducting density of states now understood, I will now return to the spectroscopy of NbSe$_2$, and an investigation of the sharp dip in fig. 2.5 Figure 2.7 shows a set of high resolution dI/dV curves measured by a lock-in technique at various temperatures. The curves are offset in 10 nS steps for clear display. The temperature dependence of the superconducting energy gap is clearly resolved. The modulation amplitude used was 40 μV_{rms} for the curve at 240 mK and 80 μV_{rms} for the rest. We have also successfully used a 10 μV_{rms} modulation amplitude for the same measurement at 240 mK.

Equation 2.2 provides a straightforward method of calculating the theoretical tunneling conductance, and a comparison between calculation and the experimental results of Fig. 2.7 is shown in Fig. 2.8a. Clearly the fits, using values of $\Delta(T = 0) = 1.1$ mV and $T_c = 7.2$ K, are not in good agreement with the data. This difficulty of fitting tunneling measurements of NbSe$_2$ is quite common, and has been commented on by both experimental (Hess 1989 & 1991) and theoretical (Hayashi 1996 & 1997) workers, who observe that the gap value appears to range from 0.7 to 1.4 mV. Hayashi *et al.* (1996 & 1997) attribute this variation to anisotropy of the superconducting gap (Clem 1966), and attempt to improve fits to experimental data by integrating over the in-plane anisotropic gap: $\Delta = \Delta_0 (1 + c_A \cos(6\phi))$, where Δ_0 is the average gap value (which they take to 1.1 mV) and c_A is the degree of in-plane anisotropy (which they take to be 0.33).

Unfortunately, even with this additional theoretical element, fits to the experimental conductance are still poor at all but the highest temperatures.

Previous to the theoretical work of Hayashi *et al*. (1996 & 1997) however, a number of experimental workers had noted the anisotropy of the superconducting energy gap as well as of other material properties, particularly when comparing c-axis ("perpendicular") and in-plane ("parallel") characteristics (Antonova 1969, Clayman 1972, de Trey 1973, Kobayashi 1977). All of these workers reported strong anisotropy (roughly a factor of 2 in gap magnitude, critical field and effective mass) between these two directions. Although tunneling current should contain a dominant c-axis contribution, along which the gap has been measured, by infrared spectroscopy, to be roughly 0.7 meV (Clayman 1972), experimentally it appears as though gap anisotropy does affect the tunneling conductance. Shown in Fig. 2.8b is a calculated tunneling conductance, uniformly integrated over half a unit sphere ($\theta = 0 .. \pi/2$, $\phi = 0 .. 2\pi$), for a fully anisotropic energy gap $\Delta = \Delta_c (1 + \varepsilon \sin^2\theta (1 + c_A \cos(6\phi)))$, with $\Delta_c = 0.62$, $\varepsilon = 1.15$
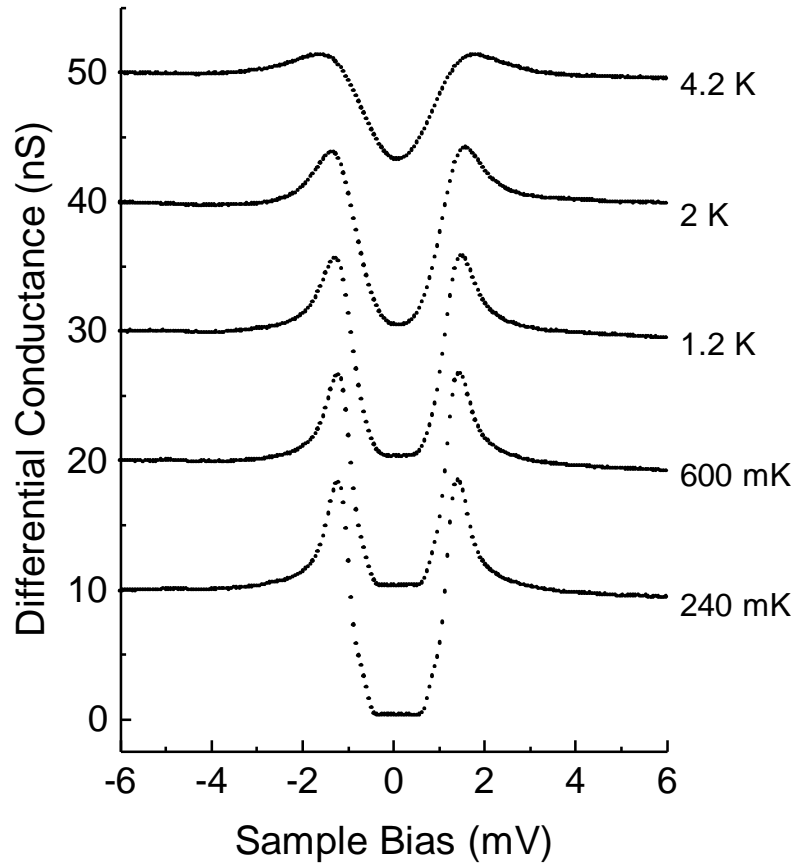
Figure 2.7. A set of dI/dV curves measured at various temperatures on the same sample as in Fig. 2.1. (Modulation frequency $f_{mod} = 331$ Hz, amplitude A_{mod} is 40 μV_{rms} for the curve at 240 mK and 80 μV_{rms} for the rest, 288 data points in 20 minutes acquisition time for each curve.) The curves are offset vertically for clear display. The temperature dependence of the superconducting energy gap is well resolved.

(a) BCS Fit (Δ = 1.1 mV)　　　　　　　**(b) Anisotropic s-Wave**
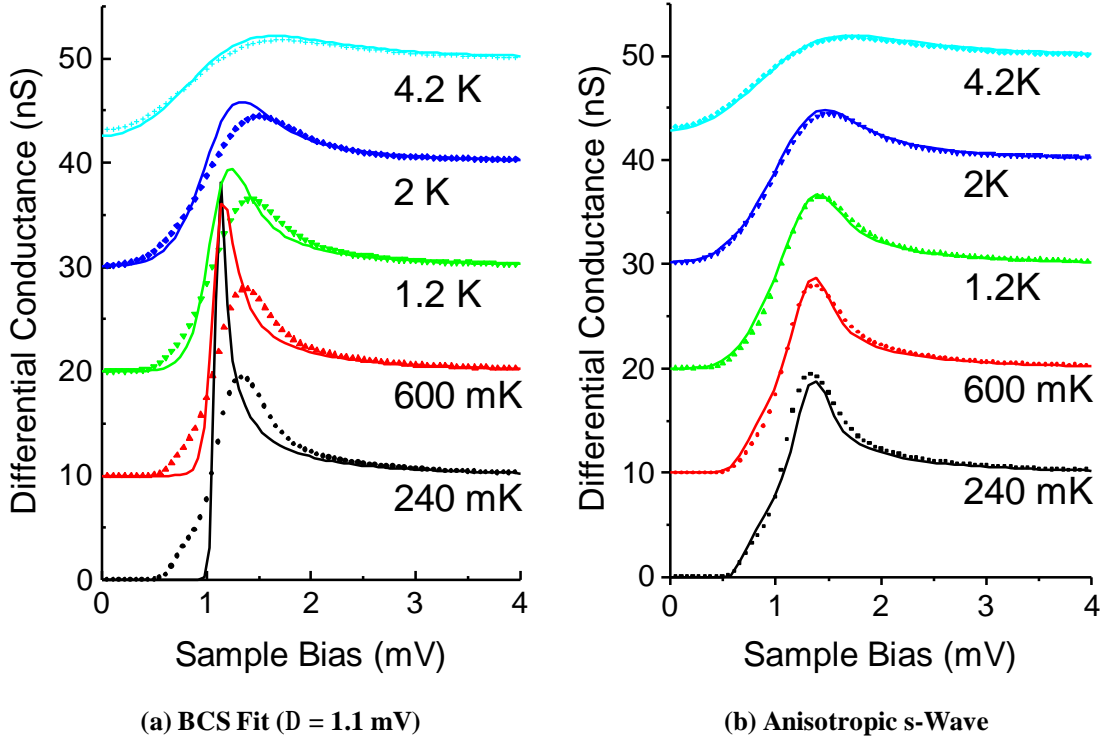
Figure 2.8.　BCS fitting with an anisotropic energy gap.　Experimental differential tunneling conductance of NbSe$_2$ at various temperatures (filled symbols) is fit with two theoretical models.　In (**a**), a BCS fit is made using a constant value for the energy gap, $\Delta = 1.1$ mV.　In (**b**), the anisotropy of the energy gap is taken into consideration, and tunneling is assumed uniform over 2π solid angle. The anisotropy of the energy gap is modeled as $\Delta = \Delta_c (1 + \varepsilon \sin^2\theta (1 + c_A \cos(6\phi)))$, with $\Delta_c = 0.62$ mV, $\varepsilon = 1.15$ and $c_A = 0.15$.　Note the quality of the fit at all measured temperatures.

and $c_A = 0.15$.　These then correspond to an energy gap which is 0.62 meV along the c-axis (consistent with the 0.7 meV mentioned above), and that the in-plane energy gap ranges from 1.2 meV to 1.43 meV, also consistent with previous measurements.　As can be seen, the fit to our experimental results is quite good.

2.3.　Differential Conductance Map: Vortex Imaging

After determining the topographic features of a surface and measuring the differential tunneling conductance as a function of energy, or, roughly speaking, the density of states at the sample surface, we are frequently interested in understanding how the DOS varies with position in the sample.　For example, the presence of impurities or crystal defects can lead to modifications of the DOS, and thus can be detected by mapping the differential conductance at the proper energy.　This technique can reveal important information about the sample under study, and an example of its use is discussed in depth in chapter 5.

(a)   (b)
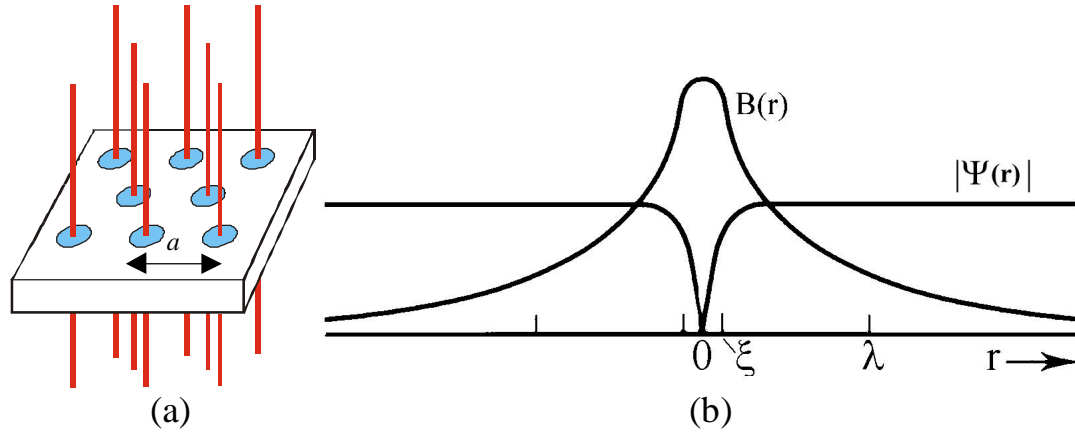
Figure 2.9. Schematic representation of magnetic vortices.
(a) Magnetic flux penetrates the superconductors in small bundles, or vortices. Each vortex is threaded by one quantum of magnetic flux, $\phi_0 = h/2e = 2.07 \times 10^{-15}$ Wb (1 Wb = 1 T m^2). In conventional superconductors the vortices form a regular hexagonal lattice, separated by a core-core distance of $a = 489\text{Å} / \sqrt{H(\text{T})}$.

 (b) A single vortex is characterized by the presence of a magnetic field B(r), which peaks at its center and decreases on the length scale of the penetration depth λ. It is also characterized by a destruction of the superconducting order parameter |Ψ(r)| at its center, which recovers over the length scale of the coherence length ξ. It is the change in the order parameter that leads to changes in the density of states, which the STM measures. In type II superconductors, which support the creation of magnetic vortices, $\lambda > \xi$. This means that the STM, measuring effects on the length scale of ξ, is inherently of higher resolution than other imaging techniques, which are sensitive to the magnetic field (with length scale λ), and thus can be used to study the vortex state in higher magnetic fields, where the vortex density is higher.

In a homogenous sample, the DOS should not in general vary with position, and thus a conductance map would not reveal much. However, inhomogeneity can be intentionally introduced into the sample, for example, by doping with impurities. For superconductors, inhomogeneity can be easily introduced and varied by the application of a magnetic field.

2.3.1. Quantized Magnetic Vortices

Superconductors typically exclude magnetic fields (known as the Meissner effect), and can be driven into the normal state by application of a large enough magnetic field (the upper critical field H_{c2}). However, for a range of applied magnetic fields H, H_{c1} < H < H_{c2}, instead of being expelled by the superconductor, the magnetic flux is instead allowed to punch through in small bundles[27], as schematically indicated in Fig. 2.9a. These flux bundles are referred to as vortices, due to the circulating current surrounding their centers (the vortex cores). Furthermore, just as fluid circulation is quantized in

---

[27] Strictly speaking, the vortex state is only observed in type II superconductors, those which have a large penetration depth λ compared to their superconducting coherence length ξ. For more details refer to a text on superconductivity, such as Tinkham (1996).

vortices in superfluid helium (Vinen 1961, Davis 1991), magnetic flux is quantized in vortices in superconductors (Deaver 1961, Doll 1961), with each vortex threaded by a single flux quantum, $\phi_0 = h/2e = 2.07 \times 10^{-15}$ Wb. As shown in Fig. 2.9b, the length scale over which the magnetic field penetrating a vortex decays is determined by the penetration depth λ of the superconductor.

The existence of this mixed state (with coexistence of magnetic vortices and superconductivity) was first predicted by Abrikosov (1957). Kleiner *et al.* (1964) and Matricon (1964) determined that these vortices would, in the high flux and low flux limits, be arranged in a hexagonal pattern (as schematically shown in Fig. 2.9a), as opposed to the square arrangement predicted by Abrikosov (1957). Experimentally, the presence of magnetic vortices can be inferred from a number of measurements, including transport, magnetization, NMR and μSR Their regular arrangement was first imaged in reciprocal space by neutron diffraction[28] (Cribier 1964), and in real space by the Bitter decoration technique (Essman 1967)[29].

2.3.2. Imaging vortices in NbSe$_2$

Although the vortices in superconductors are magnetic in nature, they also have profound effects on the local density of states (as schematically indicated in Fig. 2.9b), to which the STM is sensitive. Figure 2.10 displays Abrikosov flux lattice and vortex core images taken on NbSe$_2$, which demonstrates both this sensitivity and our ability to operate with stability in a magnetic field. We image the vortices by setting the junction resistance outside the gap (100 MΩ at 10 mV in these cases) and then measuring the differential conductance inside the gap. In addition to imaging the vortex lattice at different temperatures and field strengths (Fig. 2.10a and b), we can also image single vortices (Fig. 2.10c and d), taken in the same 50 mT field at 300 mK, to show the energy dependence of the core states. Details of the vortex lattice and vortex cores in NbSe$_2$ have been investigated by scanning tunneling microscopy by Hess *et al.* (1989 & 1991) and others (for example, Behler 1993, Volodin 1997) and, although many results have been understood (Shore 1989), they are still of theoretical interest (Hayashi 1996). Our work, however, has focussed instead on trying to transfer this imaging technique to the study of high-T$_c$ superconductors, and I will present some of our results in chapter 6.

Before moving on to results on high-T$_c$ superconductors, however, I will, in the next chapter, discuss tip preparation and characterization techniques. In particular, I will focus on the use of superconducting Nb as a tip material, which allows direct measurement of the tip temperature and opens the door to exciting future physics.

---

[28] For a recent review on the use of neutron diffraction to observe magnetic vortices, see Chang (1998).
[29] For a recent review on the use of Bitter decoration to observe magnetic vortices, see Bishop (1992).

(a)

(b)

(c)

(d)
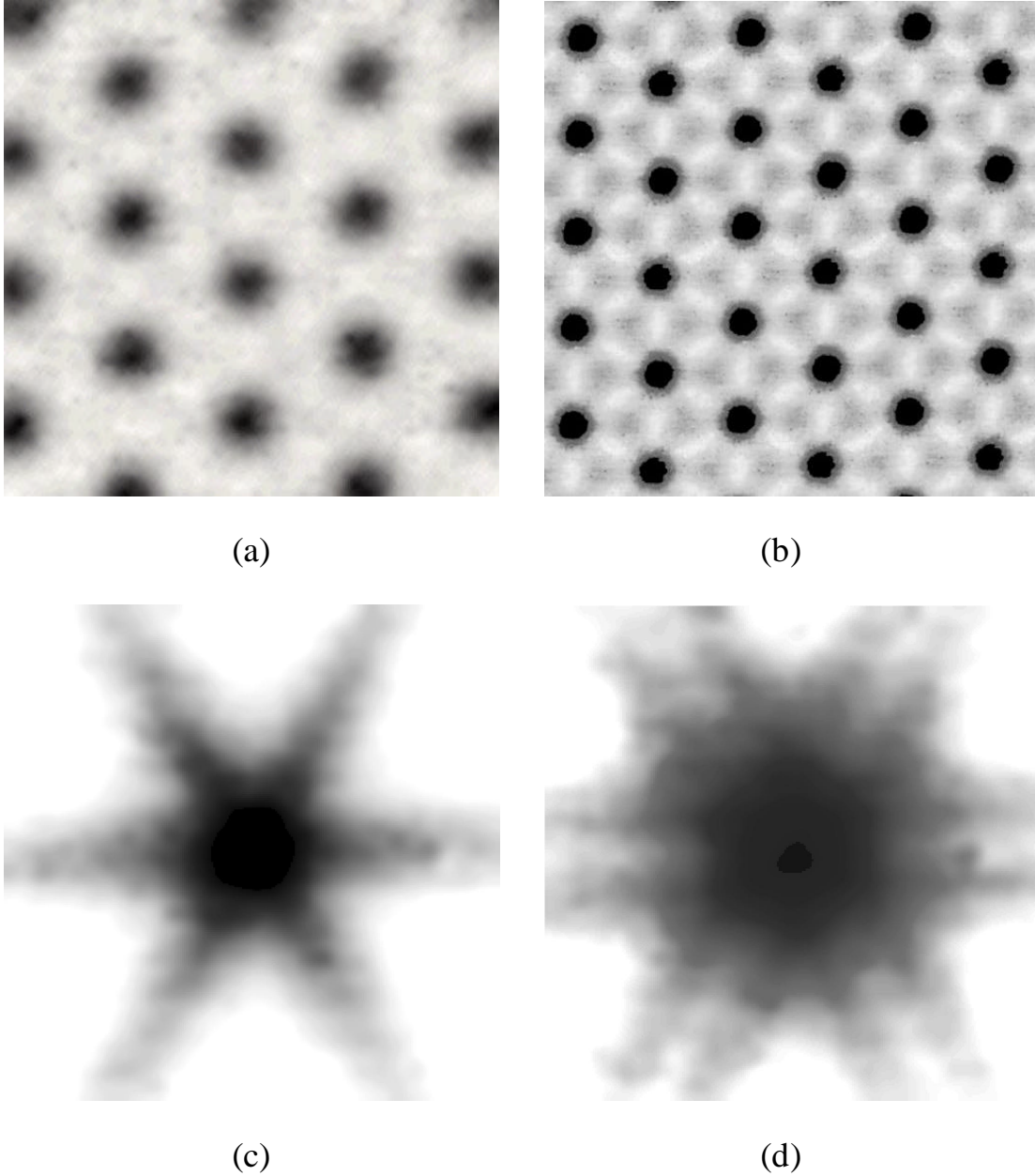
Figure 2.10. Differential conductance maps showing vortices at the surface of 2H-NbSe$_2$. (a) A magnetic field of B = 0.90 T was used, and the measurement was taken at a sample bias of V_{sample} = 0.0 mV at T = 1.6 K (200 nm). (b) B = 0.25 T, V_{sample} = -0.21 mV, T = 300 mK (500 nm).

(c) and (d) show the energy dependence of the vortex states. Both maps were taken in the same 125 nm area, in a B = 0.05 T field at T = 300 mK. (c) was obtained with V_{sample} = 0.0 mV whereas (d) was obtained with V_{sample} = -0.24 mV.

In all cases, the junction resistance was set to 100 MΩ at V_{sample} = -10 mV, and lock-in amplifier settings of f_{mod} = 447.3 Hz and A_{mod} = 100 μV$_{rms}$ were used.

Chapter 3.

Superconducting STM Tips

In this chapter I will discuss the study of atomically sharp superconducting tips for scanning tunneling microscopy and spectroscopy. The results clearly show vacuum tunneling of superconducting quasiparticles from atomically sharp tips. One benefit of such a technique is that it allows accurate measurement of the tip temperature, which confirms that our sample thermometry is consistent with both tip and sample temperature. More importantly for the future, the combination of a superconducting tip and an atomic resolution scanning tunneling microscope provides a means of achieving very high resolution local spectroscopy. I will conclude the chapter by discussing how this combination paves the way for a number of important applications.

3.1. Background

Since early in its history, scanning tunneling microscopy (STM) with nonsuperconducting tips has been used to successfully study the local properties of superconducting samples (de Lozanne 1985, Kirtley 1987 and 1990, Hess 1989). Interestingly, although it has long been proposed (Meservey 1988), use of superconducting tips for STM has not been achieved. A number of important experiments have used scanning tunneling microscopes to create adjustable microscopic junctions with superconducting electrodes (Chen 1994, DeWilde 1998, Murakami 1994). I distinguish these techniques from the use of a sharp superconducting tip (having one or a few atoms at the end), with vacuum tunneling, for atomically resolved microscopy and spectroscopy. One might naturally ask whether such a sharp tip could even exhibit a superconducting density of states (DOS) at the end.

Recently, Yazdani *et al.* (1997) noted the existence of a BCS single electron excitation spectrum above a normal metal adatom on a superconducting Nb substrate. This implies that atomically sharp superconducting STM tips might be achievable. Below, I discuss the successful realization of such tips, and describe their application to the study of both normal and superconducting samples.

3.2. Tip Preparation and Characterization

For this work, we use superconducting tips made from 0.2 mm diameter Nb wire by mechanical sharpening. The tip installation is carried out with the STM open to air at room temperature. The STM chamber is then sealed, evacuated to $\sim 10^{-6}$ Torr, and cooled to 4.2 K. The natural oxide of Nb at the apex of the tip is removed, and the tip is further sharpened, by field emission against a Au target in cryogenic ultrahigh vacuum at
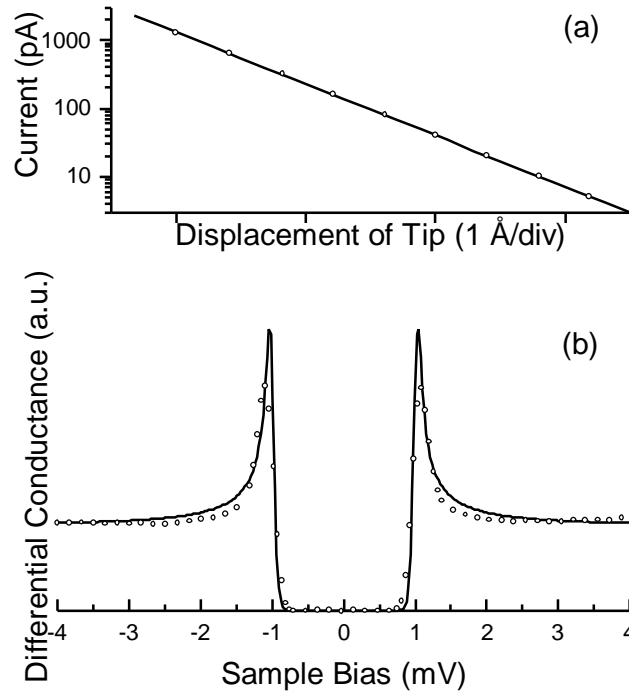
Figure 3.1. **a**.   A log/linear plot of the tunneling current versus displacement of a Nb tip from a Au surface. The circles are the measured data, and the solid line is the linear fit. The exponential relationship over three decades of current indicates the vacuum nature of the tunneling.
b. Tunneling conductance versus sample bias for the same Nb tip at 335 mK. The solid line is the calculated conductance using a BCS DOS and an energy gap $\Delta_{tip}(0) = 1.0$ meV. The circles are the measured data (only a fraction of the measured data points are shown to allow clear display of the underlying calculated curve). The spectrum indicates a superconducting quasiparticle DOS at the tip end.

4.2 K. After this process, the sharpness of the tip is verified by identification of atomic scale features on the Au surface.

Next, the relationship between tunneling current I and tip displacement from the surface z is recorded to confirm the characteristic exponential behavior of vacuum tunneling ($I \propto \exp(-z/z_0)$ where z_0 is a decay constant). As discussed in chapter 1, the effective barrier height, which represents the convoluted work function of the tip and the sample, can be extracted from this data. As an example, the results of an I versus z measurement for a Nb tip is plotted in log/linear format in Fig. 3.1a. The curve is linear over three decades of current, which confirms the vacuum nature of the tunneling, and a work function of 2.9 eV is deduced from its slope.

To evaluate the superconducting properties of this Nb tip, the differential conductance $G(V) = dI/dV$ of tunneling between tip and sample is measured as a function

of bias voltage V.[30] As mentioned in the previous chapter, this function is a measure of the convoluted local DOS of the sample and the tip. We use the Au field emission target as the sample. Fig. 3.1b shows the resulting differential conductance spectrum taken at 335 mK. It clearly demonstrates a superconducting quasiparticle DOS, as evidenced by the zero of conductance below the gap voltage and the high peaks at the gap edge. To clarify that the superconducting features in this spectrum are due to the tip, and not due to possible deposition of Nb onto the surface during field emission, this measurement is performed at several different locations separated by more than 100 nm from the location where the field emission was performed. The absence of significant variations between the spectra at different locations indicates that the energy gap in the DOS observed is that of the tip.

Interestingly, the measured superconducting energy gap value of the tip Δ_{tip} varies from tip to tip after the field emission process, ranging from a few tenths of an meV to near the bulk gap value of Nb (1.53 meV at $T = 0$ K (Townsend 1962)). The origin of this deviation is not fully understood. One possible explanation is that the superconductivity observed at the end of the tip has propagated from the bulk due to the proximity effect (Guéron 1996). Thus the measured gap will depend on the dimensions, structure, and composition of the apex of the tip, which can be modified during field emission.

3.3. Temperature Dependent Superconductor-Normal Metal Tunneling with STM

In Fig. 3.2, differential conductance spectra from another Nb tip (prepared and evaluated for its work function and sharpness as described above) are shown from 8.6 K to 380 mK. Each trace is displaced vertically for clarity. One can clearly see the superconducting gap in the DOS developing at the tip with falling temperature. The solid lines in Fig. 3.2 are the expected spectra for each temperature, calculated from a BCS DOS using a value of the energy gap for the tip $\Delta_{tip}(0) = 1.47$ meV. Note that the agreement between the measured data and calculations is much better than in Fig. 3.1b. In general, the smaller the deviation of the measured gap from its bulk value, the better the agreement with the BCS DOS, especially near the edge of the gap. This is an expected consequence of the proximity effect[31]. Finally, the quality of the fit of these temperature dependent measurements, even down to millikelvin temperatures, indicates

---

[30] All differential conductance spectra measurements reported in this chapter were performed using a lock-in technique with a modulation amplitude of 50 μV. The junction resistance was set to 100 MΩ at a bias voltage of 8 mV (well outside the superconducting energy gap).

[31] J.F. Zasadzinski (private communication).
One of the signatures of the proximity effect is the appearance of two dips directly outside of the peaks at each side of the gap edge. In SS tunneling this can be seen more clearly because there will be no thermal smearing due to a normal state electrode (as evidenced in Fig. 3.4a). One can also approximately simulate SS tunneling effects by convoluting an SN tunneling curve with itself. Self-convolutions of both the data in Fig. 3.1b and Fig. 3.2a show such dips, whereas the self-convolution of the data in Fig. 3.4b does not. This indicates that the proximity effect is indeed only in the tip.
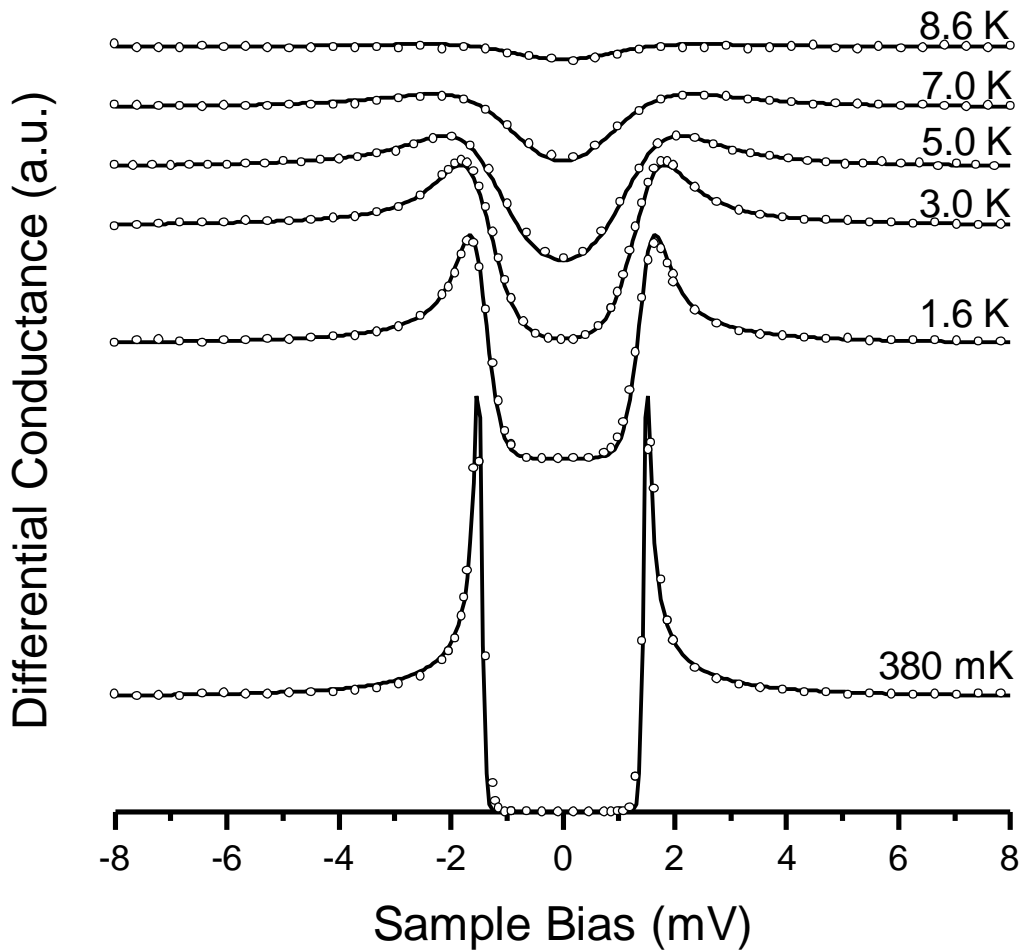
Figure 3.2. Measured differential conductance spectra (circles) for tunneling between a Nb tip and a Au surface at several temperatures. The spectra are displaced vertically from each other for clarity. The solid lines are the calculated conductance using a BCS DOS with $\Delta_{tip}(0)$ = 1.47 meV and the temperatures shown. The excellent agreement of the data and the calculations confirms that the temperature dependence of the tip DOS is very similar to that of bulk Nb, and that the temperatures quoted (as measured by the sample thermometer) accurately represent the temperature of the tip as well as the sample.

Note that the accuracy of the BCS fit is in marked contrast to that of NbSe$_2$, as discussed in the previous chapter. Although Nb is a strong coupling superconductor, which leads to structure in the density of states outside of the gap, it is significantly more isotropic than NbSe$_2$, and thus does not suffer from the same problems when attempting to fit it to tunneling calculations for a simple BCS superconductor.

that the thermometry (a Cernox thermometer mounted on the sample holder) accurately measures the temperature of the tip (that is, of the region of the tip from which the quasiparticles are tunneling) as well as the sample. This measurement therefore resolves long held concerns regarding local heating in the tip or sample due to current flow.
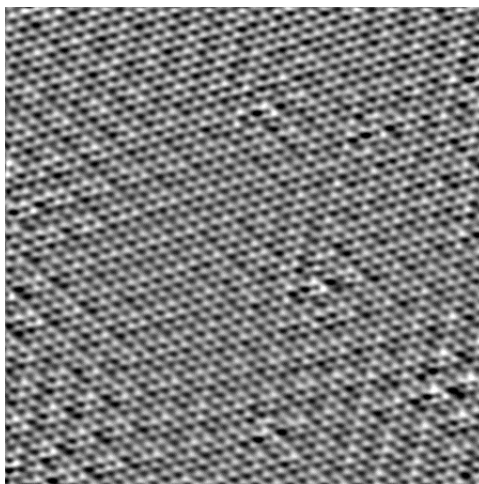
Figure 3.3. Topographic image (150 Å square) of a NbSe$_2$ surface acquired at 4.2 K in constant current mode with the superconducting tip whose tunneling spectrum is shown in Fig. 3.2. A charge density wave pattern is clearly visible. The atomic resolution of the image indicates that this superconducting tip is atomically sharp.

3.4. Superconductor-Superconductor Tunneling

To study superconducting-tip scanning tunneling microscopy on a superconductor, we now use this tip to perform measurements on a sample of NbSe$_2$. As described in chapter 2, this is a well studied, layered material, which shows a charge density wave, and has a superconducting phase transition at T$_c$ = 7.2 K. The average superconducting energy gap, as measured by STM, is $\Delta_{NbSe}(0)$ = 1.11 meV (Hess 1989). A NbSe$_2$ single crystal sample is cleaved *in situ* at 4.2 K and exchanged for the Au sample. Figure 3.3 shows an image of a NbSe$_2$ surface at T = 4.2 K, taken with the tip whose tunneling conductance spectra are shown in Fig. 3.2. Both the atomic lattice on the surface and the charge density wave are clearly resolved. This confirms that the tip is atomically sharp. Again, conductance spectroscopy is carried out on this NbSe$_2$ surface as a function of temperature and the results are displayed in Fig. 3.4a.

The two pairs of peaks in Fig. 3.4a are characteristic of the superconducting-superconducting (SS) nature of the tunneling, and clearly distinguish it from normal-superconducting (NS) tunneling. The experimental values of V = $\pm$ ($\Delta_{tip} \pm \Delta_{NbSe}$)/$e$ at which they occur are plotted in Fig. 3.5, and are in excellent agreement with the values calculated from the BCS theory (Wolf 1985, p. 105) at all temperatures measured. This confirms not only the existence of a superconducting DOS at the end of the tip, but also that tunneling in SS-STM is physically similar to that in planar junctions, albeit in a junction of far smaller area.
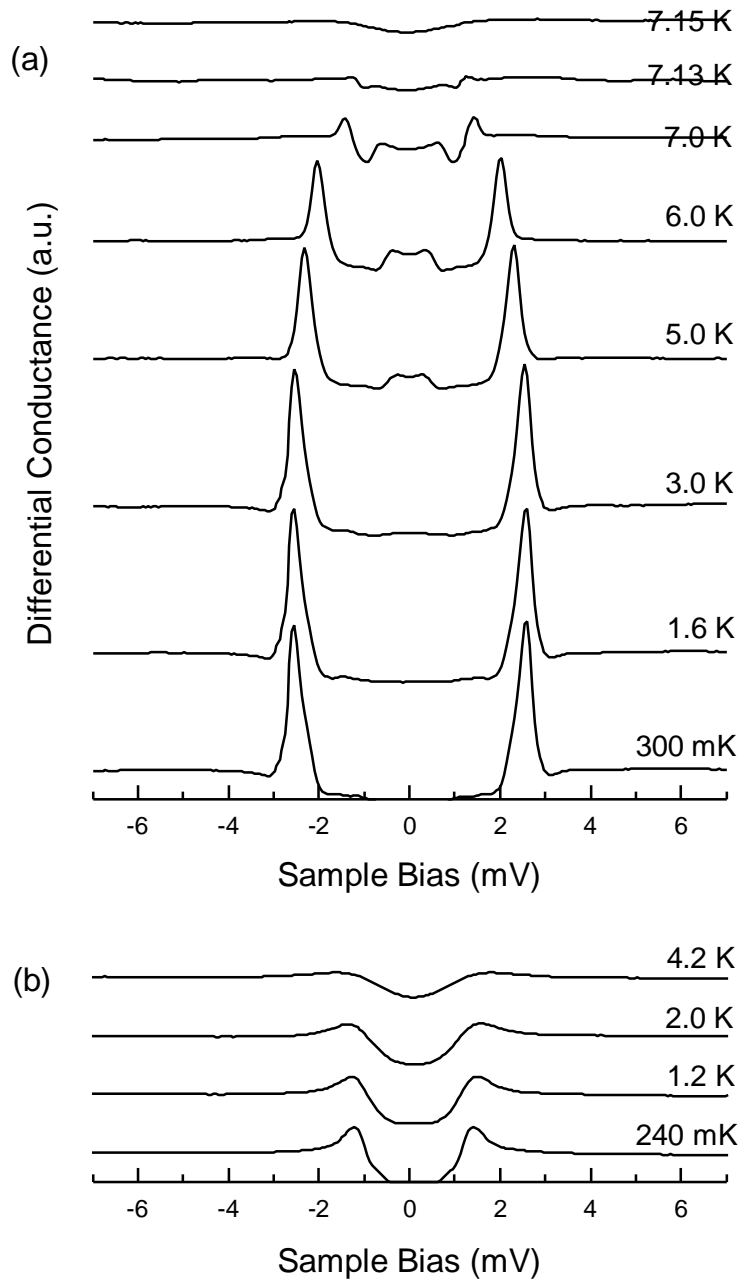
Figure 3.4. **a**. Measured differential conductance spectra for tunneling between a superconducting Nb tip and a NbSe$_2$ surface. The characteristic SS tunneling peaks at $\pm$ (Δ_{tip} + Δ_{NbSe}) and $\pm$ (Δ_{tip} - Δ_{NbSe}) vary in voltage and change in magnitude, with temperature, as expected (see fig. 3.5).
b. Measured differential conductance spectra for tunneling (NS) between a PtIr tip and a NbSe$_2$ surface. Comparison between the SS and NS tunneling spectra, plotted in the same scale, shows the dramatic enhancement in sharpness of the features obtained with a superconducting tip.

3.5. Superconducting Tips: Other Possible Applications

The use of superconducting tips in low temperature scanning tunneling microscopes has a number of significant advantages. Most important of these is the improvement in spectroscopic resolution when compared to normal-tip STM. This is due to the sudden rise in conductance at the gap edge and the associated high peak in the DOS of the superconducting tip (Solymar 1972, p. 112-113). An example of this can be seen by comparing the SS tunneling of Fig. 3.4a with the NS tunneling of Fig. 3.4b, where I show the conductance spectra acquired on NbSe$_2$ with a nonsuperconducting PtIr tip. There is a dramatic enhancement of sharpness of the features in the spectrum obtained with a superconducting tip, which could prove significant in many STS measurements, since it exists even at the commonly available temperature of 4.2 K.

Of even greater significance is the fact that superconducting-tip STM opens the door for important future applications. One example is spin polarized STM and STS. These techniques rely on the possibility of Zeeman splitting of the quasiparticle DOS for
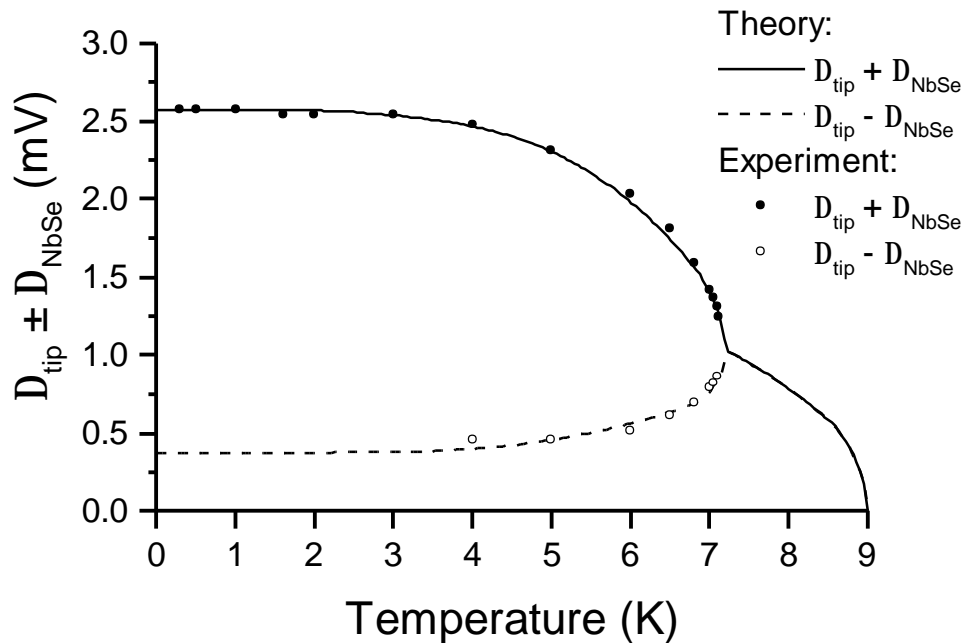
Figure 3.5. Comparison between the BCS theory predictions for, and the observed values of, $\Delta_{tip} + \Delta_{NbSe}$ and $\Delta_{tip} - \Delta_{NbSe}$. The theoretical prediction is made, assuming a BCS DOS in the tip and in the sample, with $\Delta_{tip}(0) = 1.47$ meV and $\Delta_{NbSe}(0) = 1.10$ meV respectively. The excellent agreement between the measured data and the BCS prediction indicates that tunneling in SS-STM is physically similar to that of planar junctions, although the junction area is on the atomic scale.

the two spin orientations in the superconducting tip to provide a spin polarized electron source (Meservey 1988) capable of being scanned, with atomic resolution, over the surface to be studied. Another example is Josephson tunneling in SS-STM. This would be significant in its own right, since it would provide a new type of tunable Josephson junction. It could also become a useful instrument to study, for example, spatial variations of the order parameter in exotic superconductors (Franz 1996).

Chapter 4.

The High-T$_c$ Superconductor Bi$_2$Sr$_2$CaCu$_2$O$_{8+}$d
Imaging and Identification of Atomic Planes

In this chapter I will provide some introductory information about the high-T$_c$ superconductor Bi$_2$Sr$_2$CaCu$_2$O$_{8+\delta}$ (BSCCO), the material on which the remainder of this thesis focuses. I will also present results from one particular cleavage of BSCCO, which revealed a series of repeating terraces. This measurement allows easy visualization of the incommensurate modulation, which is clearly resolved with atomic resolution on each of the exposed planes. Furthermore, the measured separations between the terraces lead to the deduction that any atomic layer can be exposed by mechanical cleavage of BSCCO,

$$a \approx b = 5.4 \text{ Å}$$
$$c = 30.7 \text{ Å}$$

$$T_c \sim 90 \text{ K}$$

$$\xi_c \approx 5 \text{ Å}$$

$$\xi_{ab} \approx 3a \approx 15 \text{ Å}$$
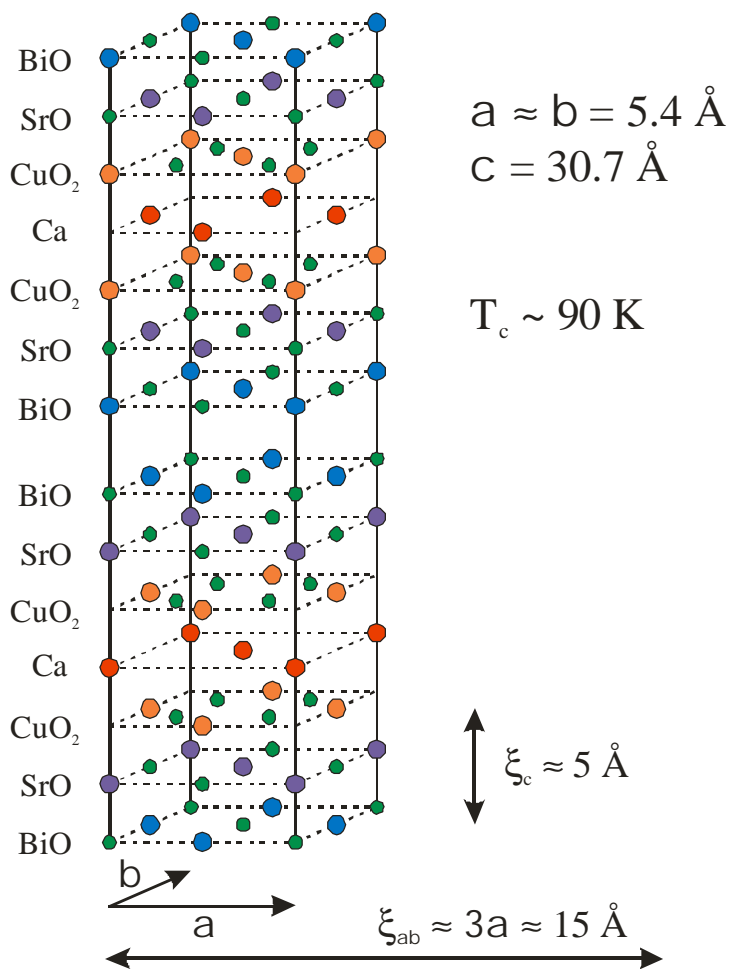
Figure 4.1. Schematic of a single unit cell of Bi$_2$Sr$_2$CaCu$_2$O$_{8+\delta}$. In each layer the oxygen is represented by the smaller circles.

which suggests that the identity of atomic planes, and the direction of tunneling, should always be taken into consideration when interpreting tunneling spectra obtained on such cleaved BSCCO crystals.

4.1. $Bi_2Sr_2CaCu_2O_{8+d}$ Crystal Structure

Superconductivity at the high temperature of 120 K was first reported in $Bi_2Sr_2CaCu_2O_{8+\delta}$ by Maeda *et al*. in January 1988, a result which was rapidly reproduced by others. The system's crystal structure was reported by Subramanian *et al*. (1988), and it is now known to belong to a class of layered superconductors, denoted Bi-22(n-1)n, which have n=1, 2 or 3 CuO_2 layers per half unit cell (Maeda 1996, pp. 8-10). The most common of these crystal structures, and the one on which we have focussed our study, is Bi-2212 (or BSCCO), a structural diagram of which is presented in Fig. 4.1. The structure is pseudo-tetragonal, based on an A-centered orthorhombic subcell. There has been some confusion in the literature regarding the labeling of the crystal axes. In this thesis the **a** and **b** axes refer to axes at 45º to the Cu-O bond direction, as shown in Fig. 4.1. With this notation, **a** ˜ **b** ˜ 5.4 Å.

The actual crystal structure is made a great deal more complicated by the existence of an incommensurate supermodulation, which runs throughout the bulk BSCCO crystal. This "superlattice," whose wave vector q ˜ $\mathbf{b}^*/4.7$[32], was first observed by Subramanian *et al*. (1988), and has since been the focus of a number of studies (Sunshine 1988, Gao 1988, Petricek 1990, Yamamoto 1990, Budin 1993, Levin 1994). Although its presence has been attributed to several causes, including missing Bi atoms in the BiO plane (Kirk 1988), its now widely accepted origin is the presence of addition O atoms in the BiO plane, which lead to a buckling of each of the atomic layers, displacing atoms from their ideal orthorhombic lattice sites along all three crystal axes.

4.2. Atomic Terraces

For the rest of this chapter I will focus on our study of a particular cleavage of BSCCO, which yielded several interesting and important results. With BSCCO, it has often been assumed that when a single crystal is cleaved along the a-b direction that the exposed surface is the BiO plane, and that the tunneling process occurs perpendicularly into this atomic plane. I will demonstrate below, however, that this is not always the case.

Before beginning this study, calibration of our STM scanner was carried out by using a Au, <111> oriented, single crystal[33] as the sample. Atomic resolution imaging and stable spectroscopy were verified on this crystal. Then, the piezo sensitivity in the

---

[32] $\mathbf{b}^*$ is the reciprocal lattice wave vector corresponding to the **b**-axis direction in real space. In other words, the supermodulation appears to ripple along the **b**-axis.

[33] Au single-crystal disc, 1 mm thick, (111) orientation, < 1° miscut, purchased from Monocrystals Co.
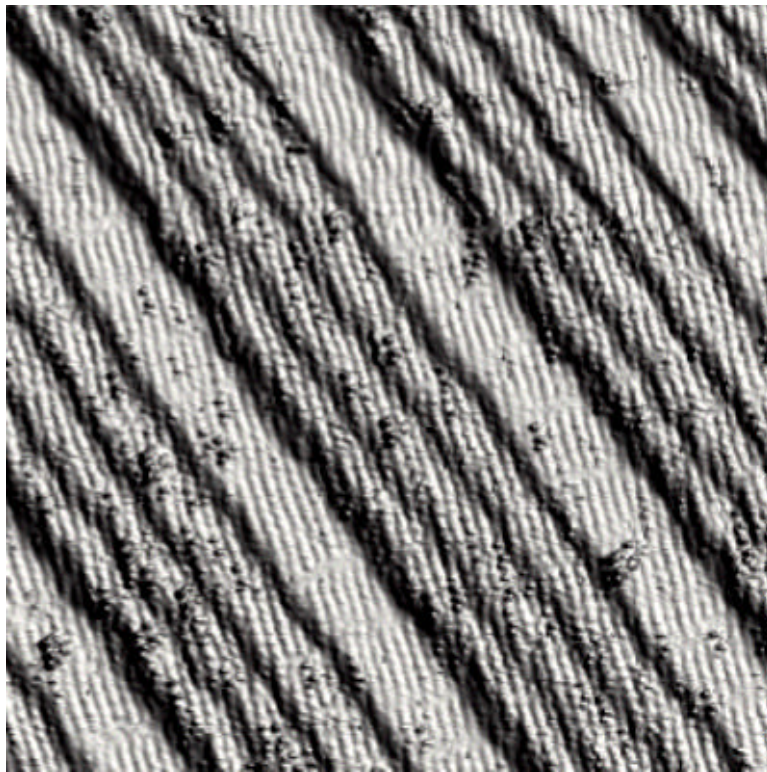
Figure 4.2. Constant current image (145 nm x 145 nm) of the surface of a cleaved BSCCO crystal, showing the supermodulation running along multiple terraces.
Imaged at T = 4.2 K (I = 4 pA, V_{sample} = +900 mV).

direction perpendicular to the sample surface was calibrated against the atomic step sizes seen on the Au <111> surface to an accuracy of 0.01nm.

The BSCCO single crystals used in this study were grown using a flux growth method, based on standard techniques described elsewhere (Yang 1993), and are re-oxygenated just prior to imaging. The onset of the superconducting transition is measured to be at 83 K, with a transition width of 9 K. The crystal is introduced into the cryogenic-UHV from room temperature as described in chapter 1, and cooled to 4.2 K. It is cleaved by the mechanical cleaver and then inserted into the STM head, which is already at 4.2 K.

A topographic image of the surface achieved after one particular cleavage of a BSCCO crystal is displayed in Fig. 4.2. It shows a series of 16 terraces stepping down from the top right to the bottom left corner. Every fourth terrace is broader than the others, and the broad terraces repeat twice in each unit cell of the crystal (as determined below). The incommensurate modulation appears as a sinuous structure. Although it has been imaged on single atomic layers before (Kirk, 1988, Shih 1989, Renner 1995, Murakami 1996), we clearly image this modulation on all terraces, and can follow it from one terrace to the next across step-edges throughout the entire field of view. Figure 4.3, which is a zoomed-in view of one of the broad terraces, shows the supermodulation with

atomic resolution. The dark area in the bottom left hand corner is the fall off of the surface at the step edge. In addition to the supermodulation, there are several different types of atomic dislocations at the crest of the supermodulation which are clearly resolved. They appear as an additional displacement of atoms beyond that due to the supermodulation. We do not know the origin of these structural features, although they are observed on almost all cleaved BSCCO surfaces which we have studied. Careful examination showed that, along with the supermodulation, these dislocations exist on all of the atomic planes shown in Fig. 4.2.

Figure 4.4 is a schematic diagram of the unit cell of the BSCCO crystal (looking along the a axis of Fig. 4.1). There are seven possible atomic layers that could be exposed in each half-unit cell, namely the BiO, SrO, CuO_2, Ca, CuO_2, SrO, and BiO planes. To identify which atomic planes are exposed in Fig. 4.2, we first make a histogram of the topographic data (the measured height of each point on the surface). This results in a series of peaks in the distribution, each peak corresponding to a particular terrace. These peaks are much wider than the resolution of the STM (1 pm) because of the smearing effect of the supermodulation. We determine the height of each terrace from the center of the associated peak in the distribution. The z-distances between each pair of the five broad terraces is 1.570(2) nm, 1.554(1) nm, 1.554(1) nm, and 1.529(3) nm, as determined by the STM. The average is 1.552 ± 0.02 nm, which
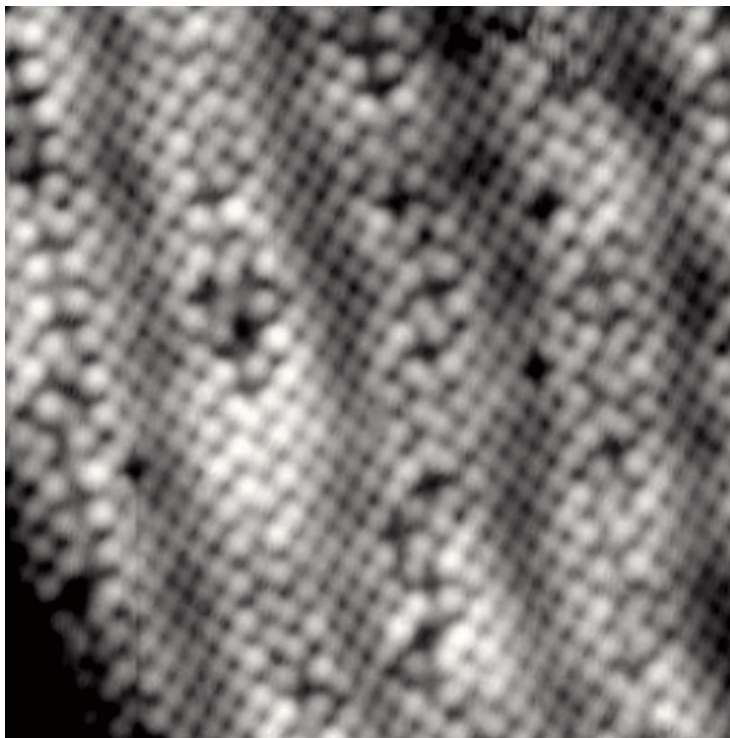
Figure 4.3. High resolution image (100 Å x 100 Å) on one of the broad terraces imaged in Fig. 4.2, showing dislocations and the supermodulation with atomic resolution. (Raw data, imaged at T=4.2 K, I=4 pA, $V_{sample} = +900$ mV)
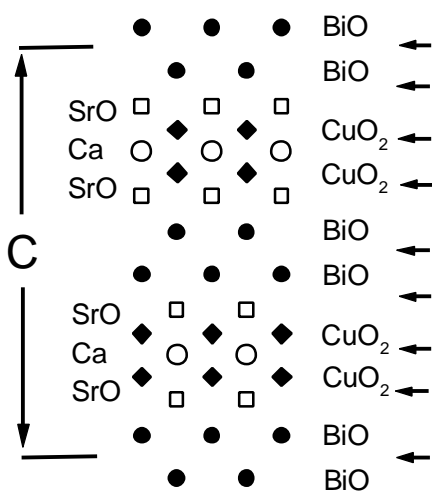
Figure 4.4. Schematic diagram, showing the unit cell of BSCCO. The unit cell height is denoted by **C**. The arrows, at right, indicate the identified cleavage planes.

agrees well with the known size of the half unit cell length of 1.545 nm (Sunshine 1988, Subramanian 1988).

To further identify the exposed atomic layers, the measured terrace separations are scaled to fractions of a unit cell and a least squares fit to the separations, as determined by x-ray diffraction (Subramanian 1988), is performed. Because of symmetry, each set of terraces (one broad and the three below it) has seven possibilities for a fit to the crystal structure (as shown in Fig. 4.5). The standard errors for the best fits are comparable, and thus the fit alone is not sufficient to determine which possibility represents the actual cleavage. However, since the longest and the weakest bonds are between two adjacent BiO planes (Kirk 1988, Lindberg 1989), we propose that the widest terrace is the BiO layer. This assumption immediately leads to the identification of the exposed atomic planes as BiO, SrO, Ca, and SrO in each half unit cell (the left-most set displayed in Fig. 4.5). It should be noted that in constant current mode topographic images, the terrace "height" depends not only on the physical separation of the atomic layers but on their DOS as well. Since, in the above analysis, no account was taken of variation of the DOS on different atomic planes, the error of the fit for the suggested cleavage is not unreasonable.

Even without the above assumption, as can be seen in Fig. 4.4, between the crystal surface we observed, and its complementary surface (on the piece cleaved off), all atomic planes were exposed. Thus, a very important implication can still be deduced -- when a tunnel-junction is made on a mechanically cleaved surface, it is possible that the tunneling is performed onto any atomic plane, or onto multiple planes of different types. Furthermore, the tunnel current may be not only perpendicular to the atomic planes but also consist of contributions into the plane (i.e. a-b direction) through step edges.
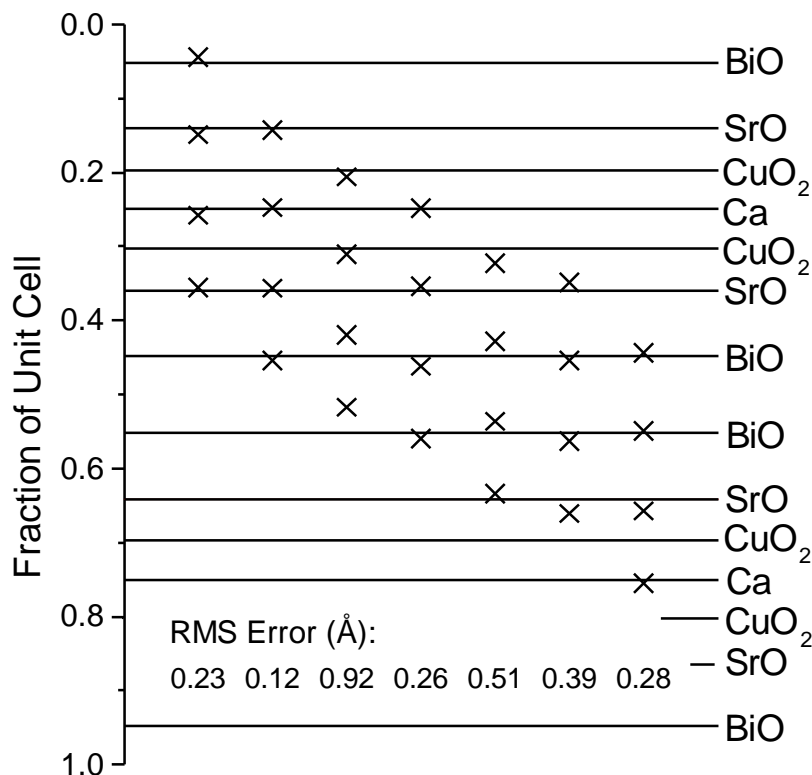
Figure 4.5. Seven possible identifications of the crystal terraces seen in Fig. 4.2. Each column of X's corresponds to the position of a broad terrace and the three terraces below it, whose separations are measured by STM. The RMS error from the least squares fit for each possibility is indicated below its column.

4.3. Summary

In this chapter I have presented images of multiple atomic layers of a cleaved BSCCO crystal. Based on the assumption that the broadest terraces are BiO layers, it is possible to identify the other atomic layers that were exposed. The important implication to draw from this work is that a BSCCO single crystal, mechanically cleaved along the a-b direction, may leave a surface with any atomic plane exposed, possibly with multiple terraces and step edges. Thus care must be taken when interpreting tunneling results from cleaved BSCCO surfaces. This can be difficult, considering that all of the planes which were exposed in this cleavage showed a quite similar supermodulation and other topographic features, making them nearly indistinguishable by topography alone. The remainder of the results on BSCCO that I will be discussing were obtained on single atomic layers. Although we have also obtained different spectroscopic results on one particular cleavage, which we believe to be due to cleaving at the CuO_2 plane[34], we assume, for the reasons mentioned above, that these single atomic layers are BiO planes.

---

[34] From neutron scattering results, it seems as though the supermodulation should appear much weaker in the CuO_2 plane than in the BiO plane, as the Cu atoms are displaced by only 10% the distance of the Bi atoms along the a and b axes.

42

Chapter 5.

Atomic Scale Quasiparticle Scattering Resonances in Bi$_2$Sr$_2$CaCu$_2$O$_{8+}$d

In the previous chapter I discussed the structural aspects of BSCCO, and focussed on topographic measurements. In this chapter I will focus instead on results of spectroscopy and spectroscopic mapping. In particular, spectroscopy of Bi$_2$Sr$_2$CaCu$_2$O$_{8+\delta}$ reveals the existence of large numbers of identical regions with diameter ~ 3 nm that have a relatively high density of low energy quasiparticle states. Their spatial and spectroscopic characteristics are consistent with theories of quasiparticle scattering from atomic scale impurities in a d-wave superconductor. These characteristics include breaking of local particle-hole symmetry, a diameter near twice the superconducting coherence length, and an inverse square dependence of their local density-of-states on distance from the scattering center. In addition to the validation of d-wave quasiparticle scattering theories, these observations also identify a source for the anomalously high levels of low energy quasiparticles in BSCCO at low temperatures.

5.1. Motivation and Background

Impurity atoms and atomic scale defects, even in very small concentrations, can strongly influence the properties of materials. In superconductors, they can play a critical role. Conventional superconductors, such as Nb and Pb, are highly sensitive to the presence of magnetic impurity atoms (Woolf 1965), which suppress the critical temperature by breaking Cooper pairs through spin flip scattering (Abrikosov 1960). Nonmagnetic impurities, on the other hand, have little effect on conventional superconductors. In the high-T$_c$ superconductors however, doping even with nonmagnetic impurities can cause dramatic effects. In fact, it is hole doping in the form of additional oxygen atoms that turns the cuprate-oxides from antiferromagnetic insulators into high-T$_c$ superconductors. On the other hand, impurity doping with Zn or Ni is known to reduce the critical temperature, modify the energy gap, increase the residual resistivity, and alter the vortex phase diagram (Maeda 1990, Xiao 1990, Bonn 1994, Lal 1994, vom Hedt 1994, Kluge 1995, Bernhard 1996, Fukuzumi 1996, Hancotte 1997, Tallon 1997, Movshovich 1998, Noetzel 1998, White 1999A & 1999B).

Despite the numerous important effects of impurity atoms on the macroscopic properties of high-T$_c$ superconductors (Balatsky 1996, and references therein), and despite numerous proposals for STM study of impurity quasiparticle scattering in these systems (Byers 1993, Salkola 1996, Kampf 1997, Flatté 1997 & 1998), no direct observation and systematic study of the effects of quasiparticle scattering at the atomic scale have been reported. Theory indicates that quasiparticle scattering at impurities can

reveal information about the symmetry of the order parameter, the **k** dependence of the energy gap, and the microscopic mechanism of superconductivity (Salkola 1996 & 1998). Several studies predict that impurity atoms create quasiparticle scattering resonances that have characteristic signatures both in the spatial shape of the "quasiparticle cloud" near the scattering center and in their tunneling spectrum (Byers 1993, Salkola 1996 & 1998, Kampf 1997, Flatté 1997 & 1998). Furthermore, it has also been predicted that the low-energy quasiparticle states generated by quasiparticle scattering may be crucial to understanding well known but unexplained low temperature anomalies in the transport properties (Lee 1993, Balatsky 1994, Franz 1996, Ziegler 1996, Joynt 1997).

Impurity scattering in a conventional superconductor has been investigated by Yazdani *et al* (1997). These workers used STM to study quasiparticle scattering from both magnetic and nonmagnetic adatoms that were deposited on the surface of a Nb crystal. For nonmagnetic atoms, no effect was observed in the local density of states near
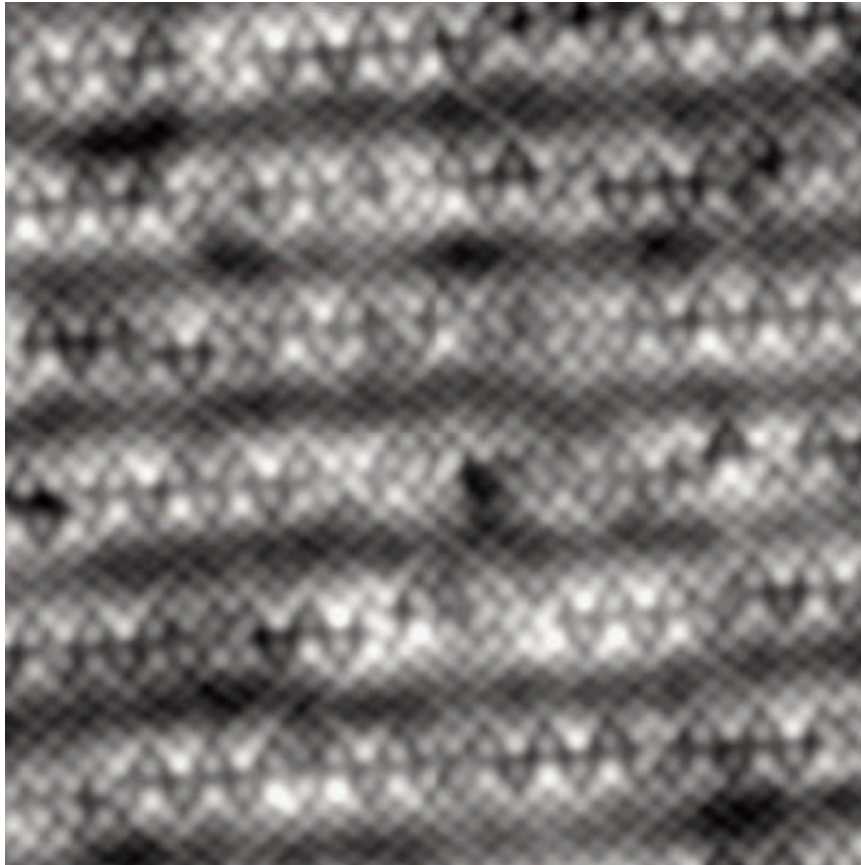
Figure 5.1. A high resolution image, showing topography of a portion of the $Bi_2Sr_2CaCu_2O_{8+\delta}$ surface studied. In this image, the Bi atoms appear as small light spots, forming a nearly square lattice. The supermodulation appears as a series of ripples travelling along the b-axis (vertical). On each crest of the supermodulation, sections of sinusoidal patterns can be seen, the origin of which is still under debate. The surface also shows strong LDOS inhomogeneities, which appear as mottled dark and light patches, and are believed to be due to an inhomogeneous oxygen concentration. This 150 Å image is taken at 4.2 K in constant current mode ($I = 100$ pA, $V_{sample} = -100$ mV).

the impurity, while for magnetic impurities (Mn and Gd) a characteristic quasiparticle scattering spectrum was observed. A.L. de Lozanne and co-workers have also reported tunneling spectroscopy over a single oxygen vacancy site in the CuO chain plane of $YBa_2Cu_3O_{7-\delta}$ (Edwards 1995).

5.2. Experimental Details

Here I will discuss the direct observation and systematic study of atomic scale quasiparticle scattering in single crystal $Bi_2Sr_2CaCu_2O_{8+\delta}$. Since the coherence length of high-T_c superconductors is only a few nanometers, a high spatial resolution STM is a necessity when attempting to identify the location and geometry of scattering sites and to study their atomic scale effects on the quasiparticle density-of states.

The STM tips used in these studies, either PtIr or W[35], are prepared and characterized as discussed for the Nb tip in chapter 3.[36] The samples, BSCCO single crystals grown by the directional solidification method (Mitzi 1990) and measured to have a T_c of 87 K with a transition width of 5 K, are cleaved and inserted into the STM head as discussed in chapter 4. A high-resolution topographic scan is taken to determine the condition of the crystal surface. Figure 5.1 shows a typical 150 Å topographic image. As mentioned at the end of chapter 4, BSCCO most often cleaves to reveal a single BiO layer with only the Bi atoms apparent in STM topography.

5.3. Quasiparticle Scattering Resonances

Following atomic resolution imaging of a larger area, we map the differential tunneling conductance at zero bias on the same area. As mentioned before, such a map is a measure of the LDOS of low energy quasiparticles and, in a superconductor at temperatures far below T_c (and in zero magnetic field), is expected to show a uniformly low differential conductance. In the gray scale used here, this would appear uniformly light. In dramatic contrast to this expectation, a typical zero-bias conductance map in BSCCO, as shown in Fig. 5.2, reveals a large number of localized dark features which have a relatively high LDOS near the Fermi energy E_f. These features are of similar size and shape, with a diameter d = 3.1 ± 0.2 nm, and appear to be randomly distributed (although they are clustered at some locations). Approximately 150 of these features are observed in this 130 nm field of view. The same average density of these features was observed in multiple samples. For reasons to be outlined below, we attribute these LDOS features to quasiparticle scattering from atomic scale defects or impurities, resulting in a

---

[35] No difference was observed between W and PtIr tips. In both cases the chemical identity of the last atom on the tip is unknown.

[36] One difference in tip preparation between the Nb tips discussed in chapter 3 and the PtIr and W tips used in these studies is the method of initial sharpening. The Nb tips are sharpened mechanically (cut), while the PtIr and W tips are chemically etched and rinsed in water before insertion into the STM.
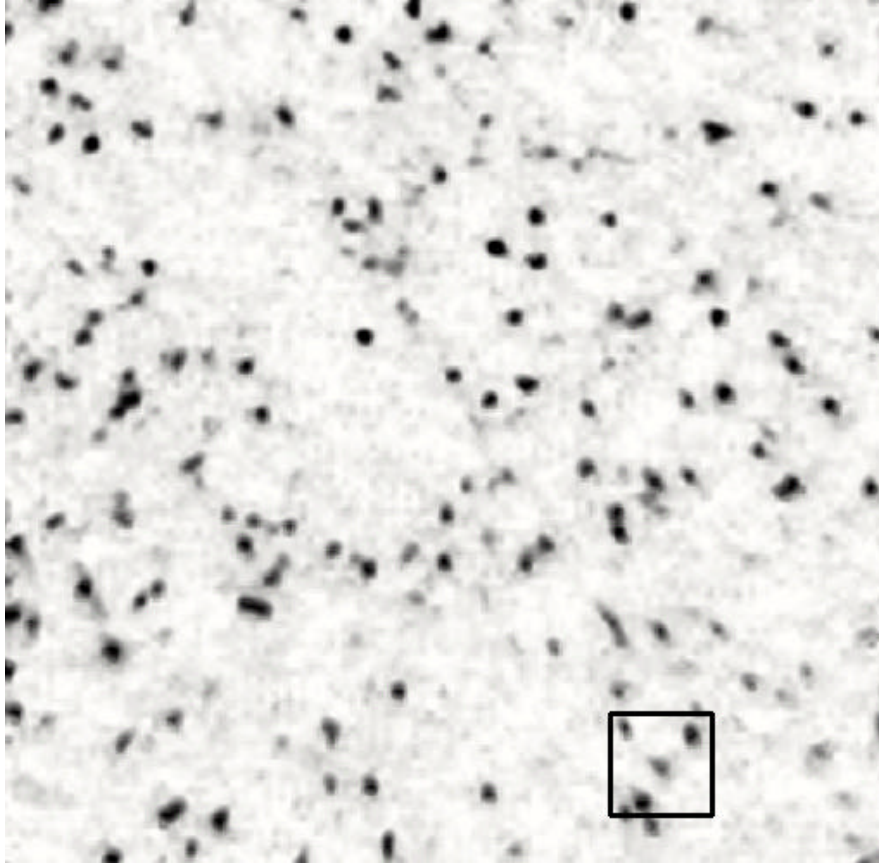
Figure 5.2. A 130 nm square zero-bias conductance map. The QPSR's appear as ~ 3 nm diameter dark regions, owing to their higher zero bias conductance. This entire area is resolved with atomic resolution in topography. As reproduction techniques do not have enough dynamic range to simultaneously show atomic resolution and over a 100 nm scale field of view, I only show as an example of topography (Fig. 5.1) the area marked here by a black frame. For the differential conductance map we set a 1 GΩ junction resistance (100 pA, -100 mV), and measure the conductance with a standard low frequency ac lock-in technique ($A_{modulation} = 500$ μV_{rms}, $f_{mod} = 447.3$ Hz).

resonance of the virtual impurity-bound states (Salkola 1996). Therefore, I will henceforth refer to these features as quasiparticle scattering resonances (QPSR's).

Because of its fundamental importance as an atomic scale probe of the superconducting order parameter, many workers have studied theoretically the effects of quasiparticle scattering from atomic scale impurities or defects in a d-wave superconductor. Predictions for the characteristics of a QPSR at an atomic scale scatterer in a d-wave superconductor include: (1) the LDOS spectrum as a function of impurity scattering strength (Salkola 1996, Flatté 1997), (2) the dependence of the LDOS on distance from the scattering center (Balatsky 1996, Salkola 1996, Kampf 1997, Flatté 1997), (3) the size of a QPSR in terms of the superconducting coherence length, and (4) the spatial shape of the LDOS near a QPSR (Byers 1993, Balatsky 1996, Franz 1996, Salkola 1996 & 1998).

46
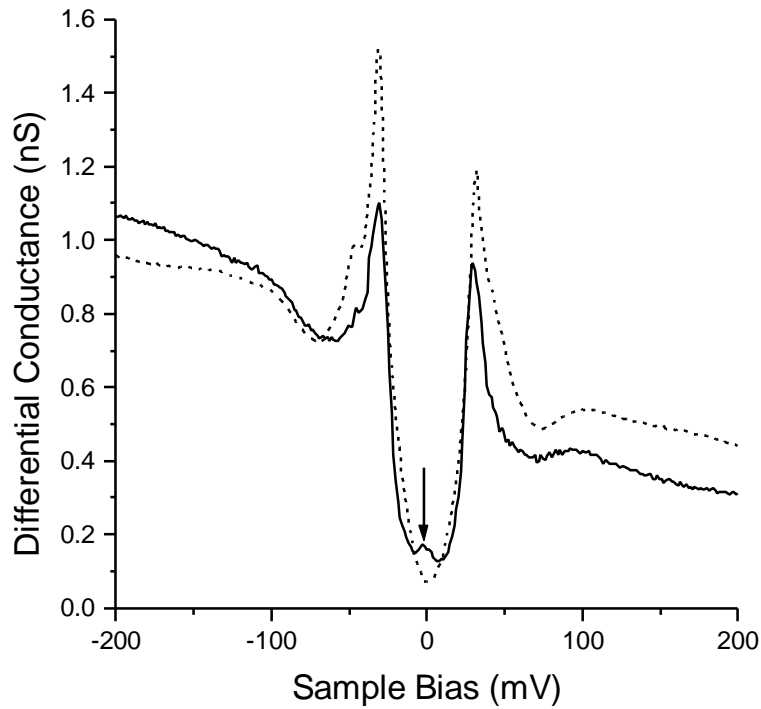
Figure 5.3. Tunneling conductance versus sample bias taken at two different locations on the BSCCO crystal. The dashed line is taken on a 'regular' superconducting region, where QPSR's are absent. The solid line is a typical spectrum taken at the center of a QPSR, exhibiting a low energy resonance peak (indicated by the arrow).

For comparison with these predictions, we carried out a series of spectroscopic measurements on a number of QPSR's. We note that when QPSR's are close together the tunneling spectra are observed to be quite complicated, as has been predicted (Balatsky 1996). Therefore, in an attempt to identify their representative properties, we selected for further study several QPSR's that have no others within at least 8 nm. A typical tunneling spectrum measured at the center of such a QPSR is shown in Figure 5.3 (solid line). For comparison, I also show as a dashed line a typical spectrum taken on a 'regular' superconducting area of the crystal (that is, one that appears light, free of QPSR's, in the conductance map of Fig. 5.2). Aside from the slight suppression of the coherence peaks at the edge of the superconducting gap, the most significant difference between these two curves is a peak in the tunneling conductance spectrum at energies near the Fermi level. Investigation of large numbers of QPSR's[37] show that this peak occurs at varying energies W_0, but always just below E_f, and its magnitude increases with increasing $|W_0|$, as has been predicted (Salkola 1996). On average the spectrum of a QPSR in the crystals studied has $W_0 = -1.3 \pm 0.4$ meV, with a width (FWHM) of 4 meV, and an amplitude of 20 % - 30 % of the normal state conductance.

---

[37] We have found these QPSR's in multiple samples from multiple sources. This chapter focuses only on results from a set of crystals from A. Gupta and K.-W. Ng at the University of Kentucky. Thus "average values," although typical of all crystals we have studied, are calculated only for these crystals.

5.3.1. Comparison to Theoretical Predictions

A number of theoretical studies have predicted the breaking of particle-hole symmetry as a property of quasiparticle scattering from a strong scattering center in a d-wave superconductor (Salkola 1996 & 1998, Kampf 1997, Flatté 1997 & 1998). For example, a recent paper by Salkola, Balatsky and Scalapino (SBS) (1996) proposes a model of quasiparticle scattering from a center described by a δ-function potential: $U(r) = U\delta(r)$. With a T-matrix formulation, they find that the virtual bound-state resonance will occur at an energy given by

$$\Omega_0 \approx \Delta_0 (2U \ln|8U|)^{-1} \qquad (5.1)$$

where $\boldsymbol{D_0}$ is the superconducting energy gap magnitude, and U is the scattering strength in units of the inverse of the density of states at the Fermi energy N_F.

Analysis of our observations in terms of this model indicates that the scattering potential is attractive ($U < 0$), as the resonances are observed below the Fermi level. In Fig. 5.4a, I show high resolution tunneling conductance spectra of six well-isolated QPSR's, and in Fig. 5.4b I show their average. A typical conductance spectrum from a 'regular' region has been subtracted from each of these spectra in order to extract only the contribution from the scattering resonances.

(a)   (b)
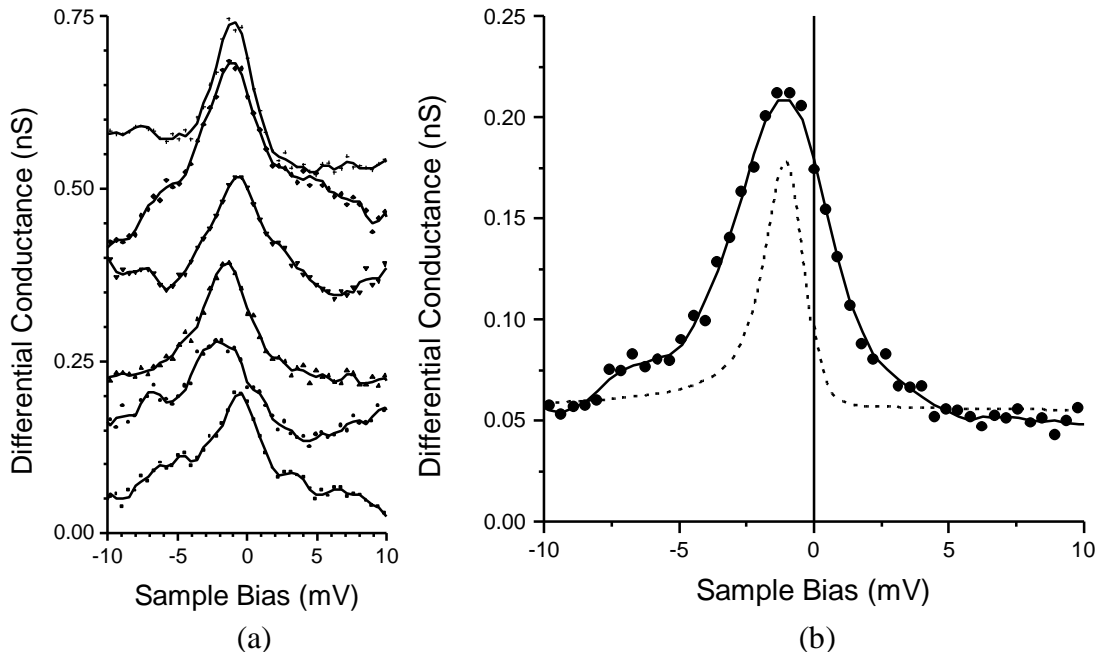
Figure 5.4**a**. High-resolution tunneling conductance spectra taken at the centers of six different QPSR's (offset in 0.1 nS increments for viewing). A typical 'regular' region spectrum has been subtracted to clarify the scattering contribution.
b. The average of the high-resolution spectra in (**a**) (solid circles). The theoretically predicted spectrum calculated using the SBS model, including the effects of thermal broadening in the tip spectrum at 4.2 K and the finite zero-bias density of states background, is shown as a dashed line.
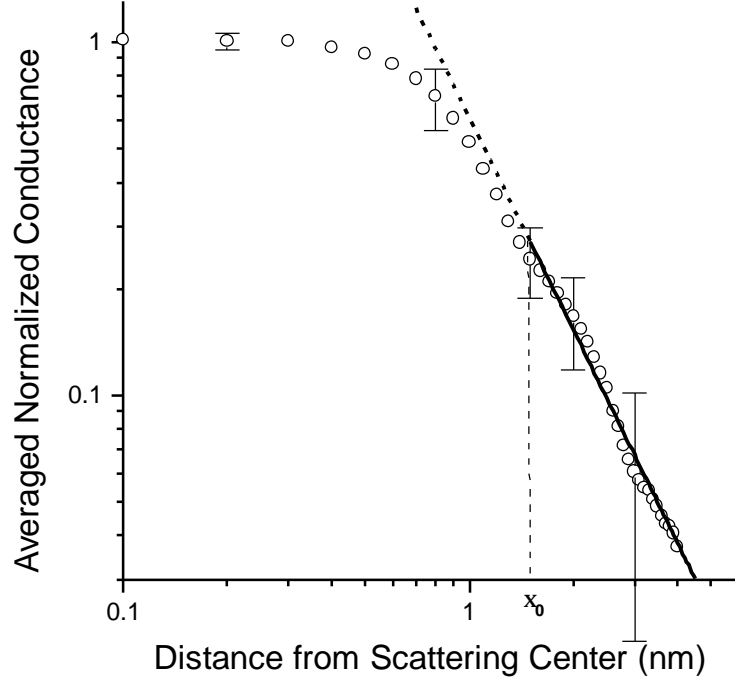
Figure 5.5. Differential conductance G at $V = -1$ mV versus distance r from the center of a QPSR. The data (circles) are extracted from the average of normalized high-resolution conductance maps of five different isolated QPSR's (shown in Fig 5.6). To calculate G(r), an average is then taken over azimuthal angles. The solid line is a linear fit, starting at $x_0 = 1.5$ nm from the QPSR center, and gives a slope of -1.97 ± 0.07 in excellent agreement with the predicted power law of $1/r^2$. The fit is extended as a dashed line to r values below x_0 as a guide to the eye.

Using the value $W_0 = -1.3$ meV from our data in Fig. 5.4b, and $D_0 = 32$ meV[38], we can invert Eqn. 5.1 to give $U = -3.6\ N_F^{-1}$ [39]. Substituting these values into the SBS model, one obtains the predicted LDOS of a QPSR. From this LDOS, and the thermally broadened LDOS of the normal-state tip, we then derive an expected tunneling conductance spectrum of the QPSR. This spectrum is shown in Fig. 5.4b as a dashed line and is in reasonable agreement with the measured QPSR conductance spectrum.[40]

The QPSR's also have a very similar physical extent to that predicted (Byers 1993, Salkola 1996), with observed diameters near 3 nm. Theory indicates a diameter of about two coherence lengths ξ_0, and in BSCCO $\xi_0 \sim 1.5$ nm (Pomar 1996). Furthermore, the dependence of the LDOS of a QPSR on distance r from its center can be analyzed by plotting the tunneling conductance G as a function of r on a log-log scale. In Fig. 5.5 I show the measured form of G(r). To extract this data we first averaged together the LDOS maps of 5 different, well isolated, QPSR's that were scanned with high spatial

---

[38] Δ, defined for this purpose as half the distance between the two superconducting peaks, varies from 25 mV to 45 mV over the observed surface, with a typical value of $\Delta_0 = 32$ mV.

[39]   Since $N_F \sim 3$ states/(eV-unit cell), $U \sim -1$ eV.

[40]   Note that in tunneling measurements, the absolute magnitude of the DOS is not directly measurable, but only the overall shape.
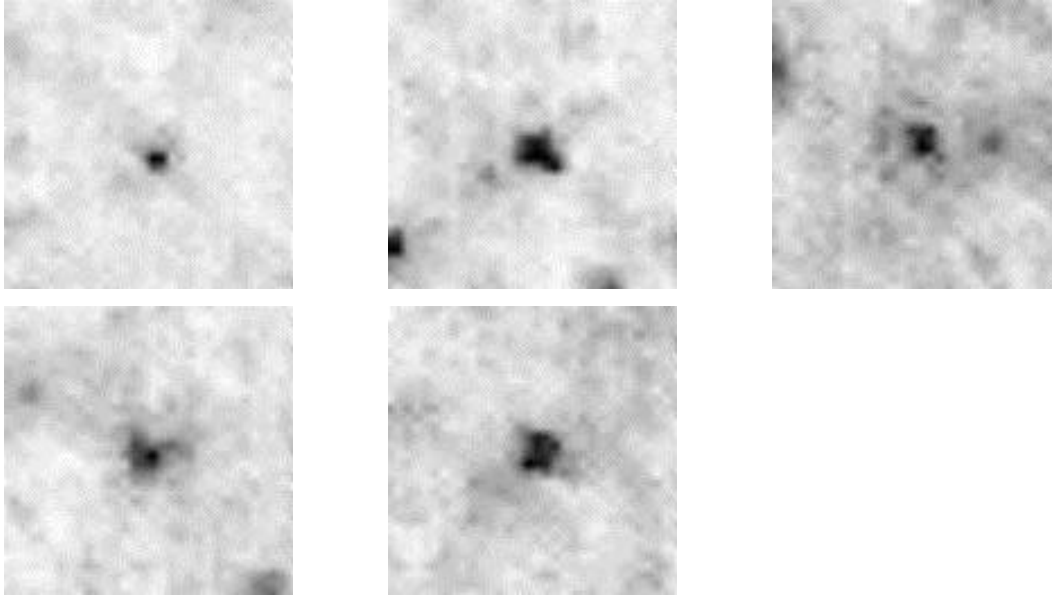
Figure 5.6. Differential conductance maps of the five individual QPSR's that were averaged in order to extract the conductance versus position curve displayed in Fig. 5.4. There may be some evidence for four-fold symmetry in these figures, however the signal to noise for this effect is too small to be sure. 125 Å (128 pixel) images are oriented with the a-axis vertical. I = 100 pA, V_{sample} = -100 mV, imaged at V_{sample} = -1 mV, near the resonance energy.

resolution (as shown in Fig. 5.6), and then averaged the result over azimuthal angles. A linear fit to the data (shown as a solid line), beginning at a distance of ξ_0 from the QPSR center, gives a slope of -1.97 ± 0.07. This result is in excellent agreement with predictions (Balatsky 1996, Salkola 1996) that $G(r) \propto 1/r^2$ for $r > \xi_0$.

Although the tunneling spectrum, physical extent, and $G(r)$ of the QPSR's are all in good agreement with theory, the four-fold cross shape predicted for the QPSR by several authors (Byers 1993, Balatsky 1996, Salkola 1996) has not been evident in this set of experiments. This shape is expected because quasiparticles can escape from the scattering site along the directions of the four nodes in a $d_{x^2-y^2}$ gap. There are several possible explanations for its absence. First, the QPSR's may not be separated by a large enough distance for this weak phenomenon to be obvious (Balatsky 1996). Secondly, and most likely, the signal to noise ratio of our measurement may be insufficient in the regions distant from the center of a QPSR where the star shape might be observed.

5.3.2. Identity of Scattering Centers

Identification of the scattering centers causing the QPSR's will require further study. Possible candidates include: (1) crystal defects, (2) elemental impurities, and (3) oxygen inhomogeneities. When high-resolution topographic data is analyzed for a correlation between it and the simultaneously acquired position of the QPSR's no strong correlation is found. Elemental impurities might be present in these crystals but microprobe analysis of these samples shows that the concentration of impurities is below

0.05 percent by weight (which is the sensitivity limit of this technique) for Mg, Ni, Fe, Al, and Co. However, this does not rule out possibility (2), as the observed QPSR concentration is below this limit. We note that the absence of any effects on the QPSR's from magnetic fields up to 7.25 T supports the view that their source is nonmagnetic. Since oxygen inhomogeneity is universal in high-T_c materials, the third possibility is intriguing. At present we are unable to differentiate between these situations, but future experiments, with systematic oxygen concentration studies or deliberate doping of known impurities, should allow us to relate the spectra to the identity of the scatterers.

5.3.3. Significance of Observations

Independent of the identification of the scattering centers, the observation of these QPSR's is significant in itself since it validates several theories of the effects of scattering at the atomic scale in d-wave superconductors. In addition, it also yields a new understanding of other properties of BSCCO. Theories have long proposed that impurity scattering induced states might lead to a number of different transport properties (Lee 1993, Balatsky 1994 & 1996, Franz 1996, Joynt 1997). Experimentally, both thermal conductivity (Movshovich 1998) and high frequency electrical conductivity (Lee 1996, Mallozzi 1998) measurements at low temperatures have found evidence of excess low energy quasiparticle states. This excess can be understood by considering the observed spatial extension of the QPSR's. At an arbitrary point in the crystal, the sum of the $1/r^2$ tails from all nearby QPSR's contributes to a finite low energy density of states. This can be seen, for example, as a finite zero-bias conductance in tunneling spectroscopy, and may be responsible for the excess quasiparticles identified in bulk measurements.

5.4. Summary

In summary, we have observed large numbers of spatially and spectrally indistinguishable quasiparticle scattering resonances. These data give direct evidence of a strong source of low energy quasiparticle excitations in BSCCO even at low temperatures. The observed QPSR characteristics, including breaking of particle-hole symmetry, diameter of $2\xi_0$, and LDOS decay as $1/r^2$, are all consistent with quasiparticle scattering from atomic scale scatterers in a d-wave (but not s-wave) superconductor. Thus, this data constitutes the first evidence for d-wave superconductivity in BSCCO at the atomic scale. Finally, this experiment demonstrates the possibility of using a single atomic scale scatterer as a probe of high-T_c superconductivity. In the next chapter I will describe further atomic scale investigations, which might one day help to unlock the secrets of the mechanism of high-T_c superconductivity.

Chapter 6.

Atomic Scale Imaging and Spectroscopy of Vortices in $Bi_2Sr_2CaCu_2O_{8+d}$

Quantized vortices reflect the fundamental nature of the condensate in which they exist, both in the structure of individual vortex cores and in that of the overall vortex solid (Salomaa 1987, Krusius 1993, Tinkham 1996, Butts 1999). Unexpectedly, these two characteristics have been reported to be distinctly different in different high-T_c superconductors. For example, scanning tunneling microscopy (STM) studies of $YBa_2Cu_3O_{7-\delta}$ (YBCO) have identified localized quasiparticle states within the vortex cores, and an ordered, oblique-rectangular vortex lattice (Maggio-Aprile 1995). In contrast, similar studies of $Bi_2Sr_2CaCu_2O_{8+\delta}$ found no evidence for localized core states and were indicative of a disordered vortex solid (Renner 1998). In this chapter I will discuss initial results from studies of BSCCO in a magnetic field, which clearly demonstrate the existence of localized vortex core states. I will also demonstrate directly that atomic scale quasiparticle scatterers discussed in the previous chapter influence the vortex solid structure by pinning some of the vortices, and that the random distribution of these scatterers in the crystal leads to the disordered vortex solid.

6.1. Motivation and Background

As described in chapter 2, when type-II superconductors, a class which includes the high-T_c materials, are placed in a magnetic field, quantized vortices are formed. These quantized vortices influence the macroscopic properties of high-T_c superconductors (Crabtree 1997, Sà de Melo 1998) and their properties strongly reflect the microscopic nature of these systems (Volovik 1993, Soininen 1994, Maki 1995, Ren 1995, Schopohl 1995, Ichioka 1996). I focus here on two particular characteristics of vortices in high-T_c superconductors, the detailed electronic structure of the vortex core itself, and the structure of the vortex solid.

Individual vortex cores may contain localized quasiparticle states which, as first described for conventional s-wave superconductors by Caroli, deGennes and Matricon (1964), are analogous to the quantum energy levels of a "particle in a box." Here, the walls of the box are formed by the pair potential Δ, which confines the quasiparticles to a single vortex core (the box). In d-wave superconductors, such as the high-T_c cuprate-oxides, the pair potential is no longer uniform in **k**-space, but instead is believed to fall to zero along four directions, at 45° to the Cu-O bond directions (Shen 1993). Vortex cores in these superconductors, now "leaky boxes," are therefore believed not to have bound

states[41]. However, if an s-wave component were to be induced due to the presence of the vortex, as has been predicted (Volovik 1993, Soininen 1994, Ren 1995, Xu 1995, Franz 1996), then localized states might exist in this region, surrounded by a region of extended states which should have a four-fold symmetry.

The arrangement of positions of these vortices (the vortex solid structure) is determined by inter-vortex interactions and by thermal fluctuations if the material is 'clean' (free of vortex pinning sites). At low temperatures, vortices in 'clean' conventional type-II superconductors repel each other and form a regular two-dimensional hexagonal arrangement -- the Abrikosov lattice (Tinkham 1996, pp. 146-7). In 'dirty' materials, vortices can be pinned at regions to which they are attracted, in order to minimize the overall energy of the system. For 'clean' d-wave superconductors, theory shows that the hexagonal lattice can become oblique-rectangular, with unit vectors that depend on the magnetic field and the microscopic details of the order parameter and its symmetry (Franz 1996, Shirashi 1999).

Although one might expect that different d-wave, high-T_C superconductors should show vortex phenomena similar to each other, the opposite has been reported. STM experiments by Maggio-Aprile *et al* (1995) clearly observed localized vortex core states in YBCO at energies of ±5.5 meV. This work also confirmed small angle neutron scattering results (Keimer 1994) by directly imaging an oblique-rectangular vortex lattice. Surprisingly, a completely different situation has been reported from STM studies of BSCCO. Localized core states have not been observed, and the vortex solid has been inferred to be disordered, rather than forming a lattice (Renner 1998; Fischer 1998, p. 499). These striking differences pose a challenge to the theory of vortices in high-T_c superconductors and have stimulated the new STM studies of BSCCO reported here.

6.2. Imaging of Magnetic Vortices

The samples and tips used in this study are prepared as discussed in chapter 5. As before, we begin by cleaving to a large, flat, atomically clean surface. To identify the quasiparticle scattering resonances (QPSR's), which were discussed in the previous chapter, and to measure background LDOS variations in the crystal surface, a zero-bias conductance map is then taken in zero magnetic field. After turning on a magnetic field, a second zero-bias map is made, which then reveals the existence of additional features associated with magnetic vortices. In order to extract information from the vortex cores *alone*, we identify several vortices that are separated by more than 100 Å from any QPSR and then measure tunneling spectra at their centers. An example of such a vortex core spectrum is shown in Fig. 6.1, along with spectra from a QPSR and from a nearby 'regular' superconducting region, one free from both vortices and QPSR's. Comparison of the spectra in Fig. 6.1 reveals two remarkable features. First, the spectrum from the vortex core center shows complete suppression of both condensation

---

[41] Marcel Franz, private communication.

peaks at the superconducting gap edge. Second, inside the energy gap of the vortex spectrum there clearly exist vortex core states which appear as two local maxima (indicated by the arrows at ±7 mV). We have studied multiple BSCCO samples and highly localized core states are always observed in vortices remote from QPSR's. However, the energy of these core states can vary from vortex to vortex with variations in the local magnitude of the superconducting energy gap.[42]

These two characteristic features, the absence of condensation peaks and the existence of vortex core states, are highly localized. They are easily distinguishable only within a few Angstroms of the vortex center and decay rapidly until no longer observable at a radius of 30 Å. This short range is consistent with the very small coherence length in BSCCO. Furthermore, because of their small magnitude, the core states can easily be masked by the presence of a scattering resonance at or near the vortex site. This can be seen by considering the sum of the vortex spectrum and the QPSR spectrum in Fig. 6.1: the dip between the peaks associated with the vortex core states is filled in by the low energy resonance, obscuring both features. Although the low energy conductance of such a spectrum is higher than that of a regular region, their overall shapes are nearly indistinguishable. These considerations emphasize the necessity for atomic resolution in spectroscopic studies of high-T_c superconductors.

Clearly, from the differences between the spectra in Fig. 6.1, the contrast for vortex mapping (which arises from the difference in conductance between a core and elsewhere) should be stronger at the core state energy. Similarly, for QPSR's the contrast should be stronger near 0 mV. Therefore, we can now apply a new method to distinguishably and simultaneously image the magnetic vortices and QPSR's by mapping at these two different energies.

Figure 6.2, obtained in a magnetic field of 7.25 T, shows a conductance map taken at -7 mV. It displays a 220 nm field of view image, containing about 170 vortices. Such large numbers of vortices not only allow a statistically robust identification of the vortex solid as disordered, but also allows Voronoi diagram analysis (Preparata 1985) for the accurate determination of the flux f associated with each vortex. Since the resulting value $f = 2.1$ ($\pm$ 0.1) x 10^{-15} Wb is consistent with $\phi_0 = 2.07$ x 10^{-15} Wb, we conclude that this core state imaging technique efficiently identifies the vortices. The apparent size and shape of the vortices vary from location to location. This is probably due to variations in the LDOS induced by inhomogeneities in the material. Such variations are also apparent in Fig. 5.1 as mottled patches of dark and light in the topography. At present we do not observe the theoretically predicted four-fold symmetry of the vortex core.

---

[42] In fact, the core state energy varies monotonically with the superconducting gap energy measured nearby. It may, in the future, be possible to determine a functional relationship, which might differentiate theories of their origin (for example, Caroli (1964) states have $E \propto \Delta^2$).
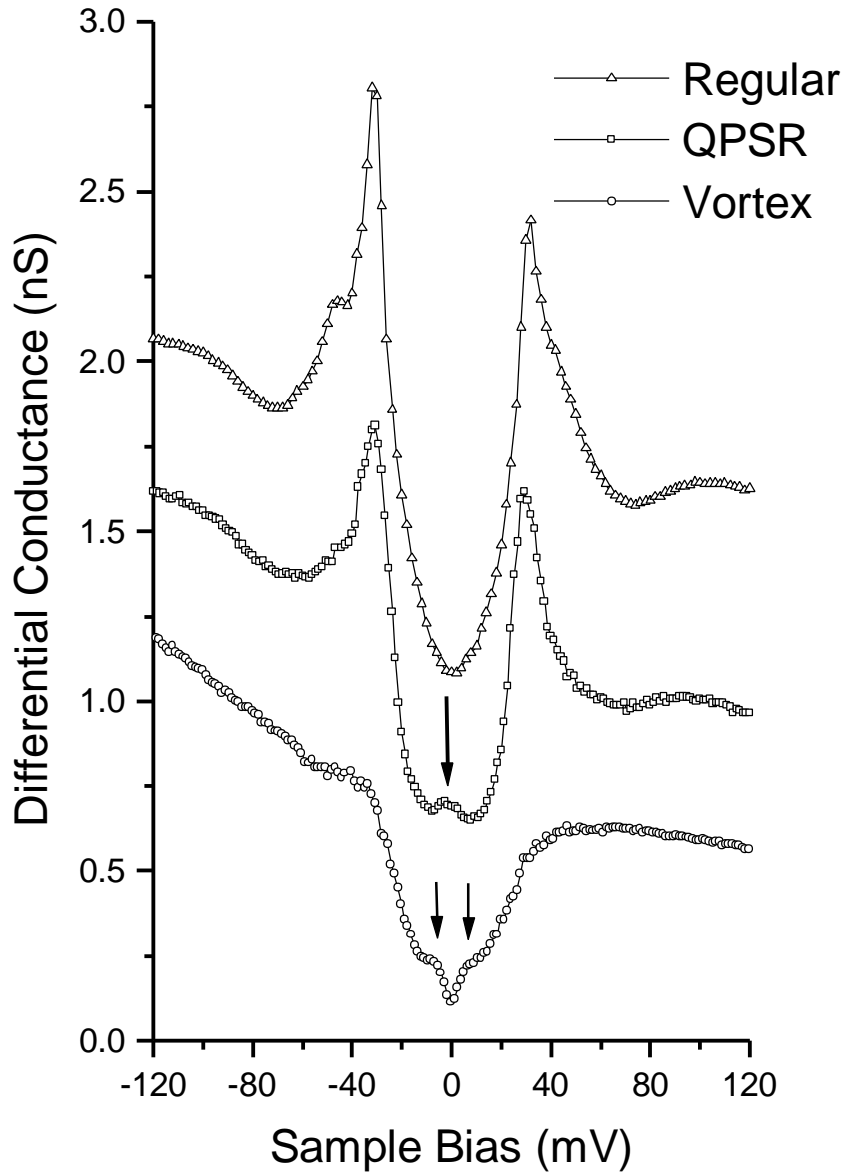
Figure 6.1. Differential tunneling conductance curves taken at three different locations. The top curve, taken on a 'regular' (free of impurity scattering resonances and magnetic vortices) part of the surface, shows a characteristic superconducting energy gap with $\Delta = 32$ mV. The middle curve is a spectrum taken at the center of a quasiparticle scattering resonance (QPSR). The long arrow indicates the location of the resonance peak that leads to an increased zero-bias conductance. The 'regular' and QPSR spectra have been offset vertically by 1.0 nS and 0.5 nS respectively for clarity. The third curve, taken at the center of a vortex core, shows the existence of core states that appear as two local maxima at ± 7 mV, as indicated by the two short arrows. In addition, there is a complete suppression of both condensation peaks at the gap edge. All three curves were obtained at 4.2 K using a lock-in technique, while the feedback is turned off. The junction resistance was set to 1 GΩ at $V_{sample} = -200$ mV, and the 447.3 Hz lock-in modulation had an amplitude of 500 μV_{rms}.

<div align="center">(a)   (b)</div>
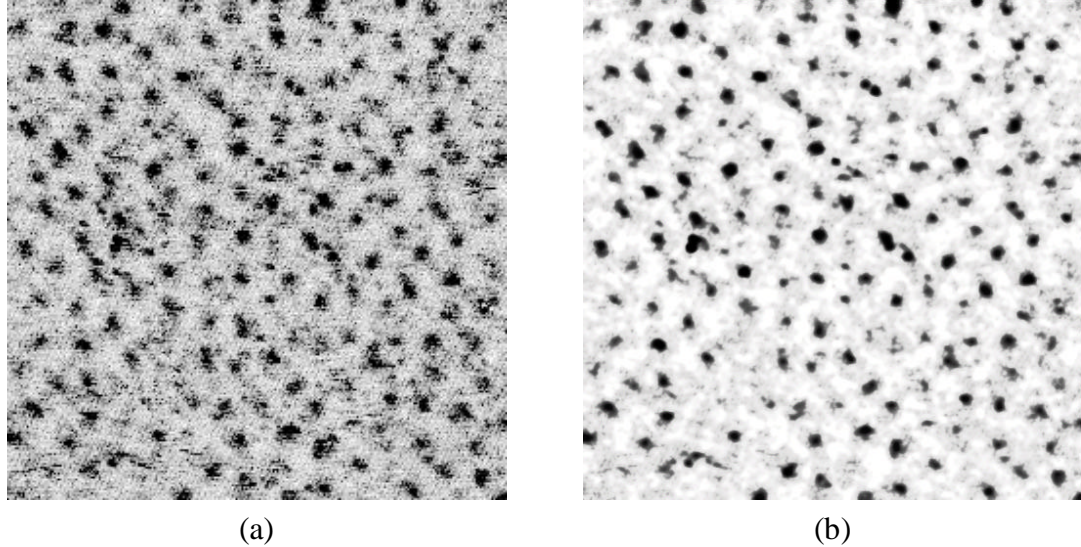
Figure 6.2. A 220 nm square differential tunneling conductance map taken in a 7.25 T magnetic field. This image, taken at a sample bias of -7 mV (near the average vortex core state energy), shows about 170 vortices. The apparent size and shape of the vortices vary from location to location. This is probably due to variations in the local density of states, as was noted in chapter 5. The vortex solid appears to be highly disordered, as opposed to being a regular vortex lattice. (a) is raw data, (b) is smoothed to enhance the contrast for the vortices.

6.3. Correlations between QPSR's and Vortices

With atomic resolution and a simultaneous mapping technique, we can study correlations among topographic features, QPSR's, and magnetic vortices. No significant correlation between topography and the positions of the QPSR's or vortices is found. In contrast, the correlation between the vortices and QPSR's is very significant. As shown in Fig. 6.3, a zero-bias conductance map, the QPSR's all appear as ~ 30 Å diameter dark features. Magnetic vortices in the same area are simultaneously identified by conductance mapping at -7 mV, and their positions are precisely marked on this map as dark circles. One can see that vortices often reside in regions with a high density of QPSR's and are rarely found in regions of low density. This is indicative of the difficulty in identifying for tunneling spectroscopy those vortex cores uninfluenced by scattering centers. In addition, the centers of about 30 % of the vortices coincide closely with the position of a QPSR. Since the probability of such a coincidence is at least three times greater than expected from uncorrelated distributions[43], we conclude that the scattering

---

[43] A rough value of the expected coincidence rate for two uncorrelated distributions can be calculated as follows. We are interested in determining the likelihood of a vortex lying on a QPSR. Imagine that the area in which the vortex is to be placed is tiled with cells whose area is the inverse of the QPSR density ($A_Q = 1/\rho_Q$). Put the vortex at the center of one of these cells. On average a single QPSR will be located somewhere within the cell. Then the expected coincidence rate is simply the ratio of the area in which the QPSR would be considered 'coincident' A_C (for example, the area of the vortex) to the total area of the cell A_Q. Depending on the definition of 'coincidence,' the definition of A_C can change. For example, if the QPSR and vortex radii are r_Q and r_V respectively, then for a QPSR to be completely contained in the vortex, $A_C = \pi(r_V - r_Q)^2$, whereas for them to be merely touching, $A_C = \pi(r_V + r_Q)^2$.
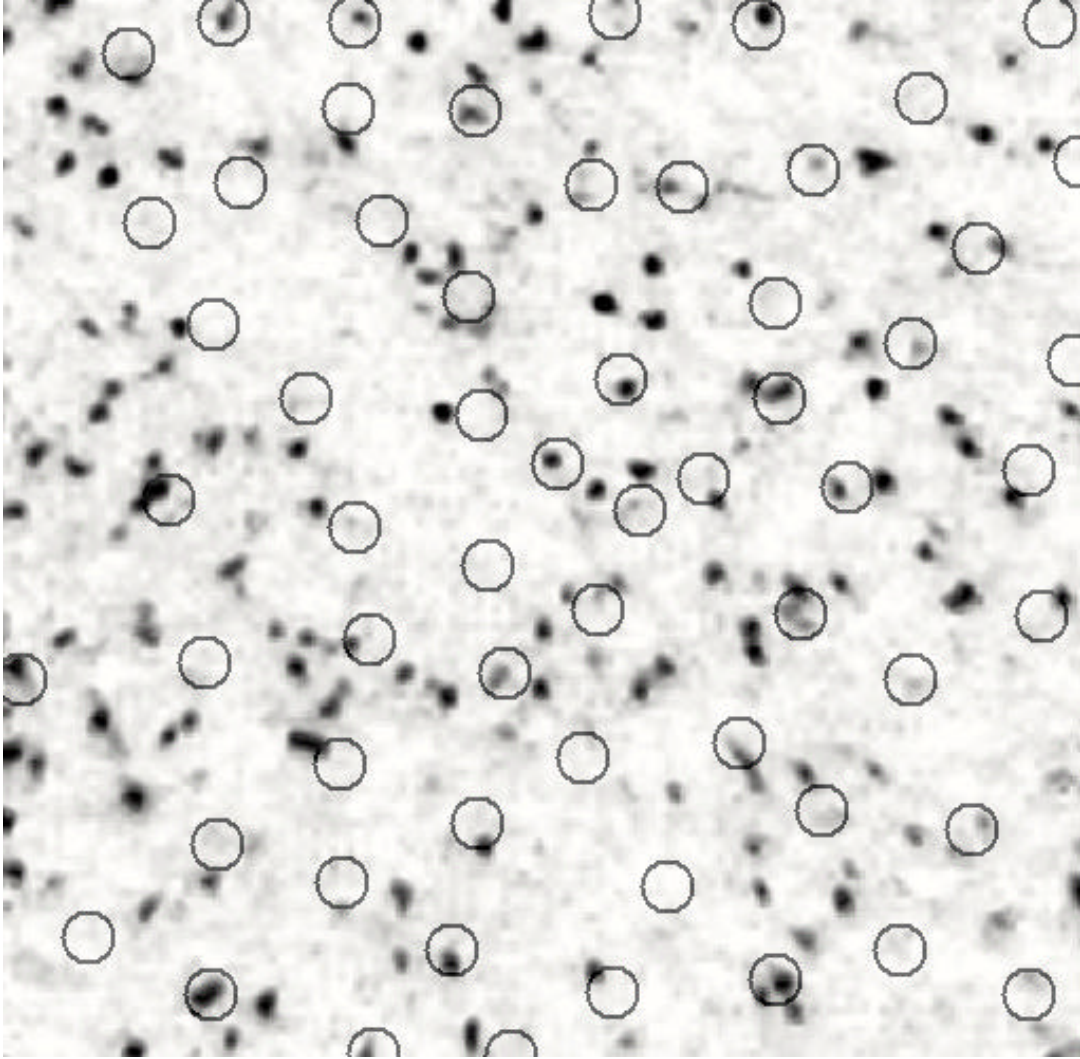
Figure 6.3. A zero-bias conductance map of a 130 nm square region of the surface taken at B = 7.25 T. The QPSR's appear as ~ 30 Å diameter dark regions, owing to their higher zero bias conductance. Magnetic vortices are simultaneously mapped in this area, and their positions are indicated by 60 Å diameter circles. One obvious feature is that many vortices reside in regions with a high density of QPSR's and are rarely found in regions of low density. In addition, the positions of approximately 30 % of the vortices appear to coincide with that of a QPSR. This is a significantly higher coincidence rate than would be expected for uncorrelated random distributions of QPSR and vortex positions at these densities. From this, we conclude that the randomly distributed scattering centers pin the magnetic vortices and lead to disorder in the BSCCO vortex solid.

centers responsible for the QPSR's also provide attractive potentials for pinning of the vortices. Thus, this experiment directly demonstrates that the pinning of vortices by randomly distributed scattering centers provides a source for the disorder in the BSCCO vortex solid.

6.4. Summary

To summarize, we demonstrate experimentally the existence of localized quasiparticle states in vortex cores in BSCCO. These states are easily resolved only within a few Angstroms of the vortex center and decay rapidly until no longer observable at a radius of 30 Å. Both superconducting energy gap peaks are also suppressed in the same region of space. The vortex solid, imaged by conductance mapping at the core state energy, is highly disordered. By comparing the independently measured positions of atomic scale quasiparticle scattering centers with the positions of the vortices, we demonstrate that the vortex solid disorder is due to pinning by randomly distributed scattering centers in the crystal. Both of these two aspects of the mixed state, vortex core states and vortex solid order, reflect the nature of the superconducting condensate in $Bi_2Sr_2CaCu_2O_{8+\delta}$. At this point, however, much analysis still remains in order to extract detailed information. None-the-less, these results represent the next step in our efforts to use microscopic perturbations as a probe of the pairing mechanism in exotic superconductors.

Bibliography

Abrikosov 1957. A.A. Abrikosov. On the Magnetic Properties of Superconductors of the Second Group. *Zhurnal Eksperimental'noi i Teoreticheskoi Fiziki* **32**, 1442-52 (1957); *Soviet Physics – JETP* **5** (6), 1174-82 (1957).

Abrikosov 1960. A.A. Abrikosov and L.P. Gor'kov. Contribution to the theory of superconducting alloys with paramagnetic impurities. *Zhurnal Eksperimental'noi i Teoreticheskoi Fiziki* **39**, 1781-96 (1960); *Soviet Physics – JETP* **12** (6), 1243-53 (1961).

Antonova 1969. E.A. Antonova, S.A. Medvedev, and I.Yu. Shebalin. The anisotropy of the superconducting properties of Niobium Diselenide and the relationship between the properties and the crystal structure and composition. *Zhurnal Eksperimental'noi i Teoreticheskoi Fiziki* **57** (2), 329-45 (1969); *Soviet Physics JETP* **30** (2), 181-9 (1970).

Ashcroft 1976. N.W. Ashcroft and N.D. Mermin. *Solid State Physics* (W.B.. Saunders Company, Philadelphia, 1976).

Balatsky 1994. A.V. Balatsky, A. Rosengren, and B.L. Altshuler. Impurities and quasi-one-dimensional transport in a d-wave superconductor. *Physical Review Letters* **73** (5), 720-3 (1994).

Balatsky 1995. A.V. Balatsky, M.I. Salkola, A. Rosengren. Impurity-induced virtual bound states in d-wave superconductors. *Physical Review B* **51** (21), 15547-51 (1995).

Balatsky 1996. A.V. Balatsky and M.I. Salkola. Impurity states and the absence of quasiparticle localization in disordered d-wave superconductors. *Physical Review Letters* **76** (13), 2386-9 (1996).

Bardeen 1957. J. Bardeen, L.N. Cooper and J.R. Schrieffer. Theory of Superconductivity. *Physical Review* **108** (5), 1175-1204 (1957).

Bardeen 1960. J. Bardeen. Tunneling from a many-body point of view. *Physical Review Letters* **6** (2), 57-9 (1960).

Behler 1993. S. Behler. Rastertunnelmikroskopie an Supraleitern und Fullerenen bei tiefen Temperaturen. Ph.D. Thesis, Inst. für Physik, Uni. Basel, Switzerland (1993).

Bernhard 1996. C. Bernhard, J.L. Tallon, C. Bucci, R. De Renzi, G. Guidi, G.V.M Williams, C. Niedermayer. Suppression of the superconducting condensate in the high-T_c cuprates by Zn substitution and overdoping: evidence for an unconventional pairing state. *Physical Review Letters*, **77** (11), 2304-7 (1996).

Binnig 1982a.   G. Binnig and H. Rohrer. Scanning Tunneling Microscopy. *Helvetica Physica Acta* **55** (6), 726-35 (1982).

Binnig 1982b.   G. Binnig, H. Rohrer, Ch. Gerber, and E. Weibel. Surface studies by scanning tunneling microscopy. *Physical Review Letters* **49** (1), 57-61 (1982).

Bishop 1992.   D.J. Bishop, P.L. Gammel, D.A. Huse, C.A. Murray. Magnetic Flux-Line Lattices and Vortices in the Copper Oxide Superconductors. *Science* **255** (5041), 165-72 (1992).

Bonn 1994.   D.A. Bonn, S. Kamal, Kuan Zhang; Ruixing Liang; D.J. Baar, E. Klein, W.N. Hardy. Comparison of the influence of Ni and Zn impurities on the electromagnetic properties of $YBa_2Cu_3O_{6.95}$. *Physical Review B* **50** (6), 4051-63 (1994).

Budin 1993.   H. Budin, O. Eibl, P. Pongratz, and P. Skalicky. Disorder in the BiO sublattice of $Bi_2Sr_2Ca_{n-1}Cu_nO_{2n+4+z}$ phases. *Physica C* **207** (3-4), 208-24 (1993).

Butts 1999.   D.A. Butts and D.S. Rokhsar. Predicted signatures of rotating Bose-Einstein condensates. *Nature* **397** (6717), 327-9 (1999).

Byers 1993.   J.M. Byers, M.E. Flatté, D.J. Scalapino. Influence of gap extrema on the tunneling conductance near an impurity in an anisotropic superconductor. *Physical Review Letters* **71** (20), 3363-6 (1993).

Campuzano 1990.   J.C. Campuzano, G. Jennings, M. Faiz, L. Beaulaigue, B.W. Veal, J.Z. Liu, A.P. Paulikas, K. Vandervoort, H. Claus, R.S. List, A.J. Arko and R.J. Bartlett. Fermi surfaces of $YBa_2Cu_3O_{6.9}$ as seen by angle-resolved photoemission. *Physical Review Letters* **64** (19), 2308-11 (1990).

Caroli 1964.   C. Caroli, P.G. DeGennes, and J. Matricon. Bound fermion states on a vortex line in a type II superconductor. *Physics Letters* **9** (4), 307-9 (1964).

Chang 1998.   D. Chang, C.-Y. Mou, B. Rosenstein, C.L. Wu. Interpretation of the Neutron Scattering Data on Flux Lattices of Superconductors. *Physical Review Letters* **80** (1), 145-8 (1998).

Chen 1993.   C.J. Chen, *Introduction to Scanning Tunneling Microscopy* (Oxford University Press, Oxford, 1993).

Chen 1994.   Qun Chen, K.-W. Ng, A.E. Manzi, and H.L. Luo. Tunneling studies of $Bi_2Sr_2Ca_2Cu_3O_{10-x}$ in the ab plane. *Physical Review B* **49** (9), 6193-6 (1994).

Clayman 1972.   B.P. Clayman. Anisotropy in the Superconducting Energy Gap of $NbSe_2$. *Canadian Journal of Physics* **50** (24), 3193-7 (1972).

Clem 1966.   J.R. Clem. Effects of Energy Gap Anisotropy in Pure Superconductors. *Annals of Physics* **40** (2), 268-95 (1966).

Coombs 1986. J.H. Coombs and J.B. Pethica. Properties of vacuum tunneling currents: anomalous barrier heights. *IBM Journal of Research and Development* **30** (5), 455-9 (1986).

Crabtree 1997. G.W. Crabtree and D.R. Nelson. Vortex physics in high-temperature superconductors. *Physics Today* **50** (4), 38-45 (April 1997).

Cribier 1964. D. Cribier, B. Jacrot, L. Madhav Rao, and B. Farnoux. Mise en evidence par diffraction de neutrons d' une structure periodique du champ magnetique dans le Niobium supraconducteur. *Physics Letters* **9** (2), 106-7 (1964).

Davis 1991. J.C. Davis, J.D. Close, R. Zieve, and R.E. Packard. Observation of quantized circulation in superfluid ^{3}He-B. *Physical Review Letters* **66**, 329-32 (1991).

de Lozanne 1985. A.L. de Lozanne, S.A. Elrod, and C.F. Quate. Spatial variations in the superconductivity of Nb_3Sn measured by low-temperature tunneling microscopy. *Physical Review Letters* **54** (22), 2433-6 (1985).

de Lozanne 1998. A.L. de Lozanne, H.L. Edwards, C. Yuan, and J.T. Markert. Scanning probe microscopy and spectroscopy of high temperature superconductors. *Acta Physica Polonica A* **93** (2), 333-42 (1998).

de Trey 1973. P. de Trey, Suso Gygax and J.-P. Jan. Anisotropy of the Ginzburg-Landau Parameter k in $NbSe_2$. *Journal of Low Temperature Physics* **11** (3/4), 421-34 (1973).

Deaver 1961. B.S. Deaver and W.M. Fairbank. Experimental evidence for quantized flux in superconducting cylinders. *Physical Review Letters* **7** (2), 43-6 (1961).

DeWilde 1998. Y. DeWilde, N. Miyakawa, P. Guptasarma, M. Iavarone, L. Ozyuzer, J.F., Zasadzinski, P. Romano, D.G. Hinks, C. Kendziora, G.W. Crabtree, and K.W. Gray. Unusual strong-coupling effects in the tunneling spectroscopy of optimally doped and overdoped $Bi_2Sr_2CaCu_2O_{8+\delta}$. *Physical Review Letters* **80** (1), 153 (1998).

Doll 1961. R. Doll and M. Näbauer. Experimental proof of flux quantization in a superconducting ring. *Physical Review Letters* **7** (2), 51-2 (1961).

Edwards 1992. H.L. Edwards, J.T. Markert and A.L. de Lozanne. Energy gap and surface structure of $YBa_2Cu_3O_{7-x}$ probed by scanning tunneling microscopy. *Physical Review Letters* **69** (20), 2967-70 (1992).

Edwards 1995. H.L. Edwards, D.J. Derro, A.L. Barr, J.T. Markert, A.L. de Lozanne. Spatially varying energy gap in the CuO chains of $YBa_2Cu_3O_{7-x}$ detected by scanning tunnelling spectroscopy. *Physical Review Letters* **75** (7), 1387-90 (1995).

Essman 1967. U. Essman and H. Träuble. The direct observation of individual flux lines in type II superconductors. *Physics Letters* **24A** (10), 526-7 (1967).

Fischer 1998. Ø. Fischer, Ch. Renner and I. Maggio-Aprile. Scanning Tunneling Microscopy on High Temperature Superconductors in *The Gap Symmetry and Fluctuations in High-Tc Superconductors*, edited by J. Bok, G. Deutscher, D. Pavuna, and S.A. Wolf. pp. 487-502 (Plenum Press, New York, 1998).

Flatté 1997. M.E. Flatté and J.M. Byers. Local electronic structure of defects in superconductors. *Physical Review B* **56** (17), 11213-31 (1997).

Flatté 1998. M.E. Flatté and J.M. Byers. Impurity effects on quasiparticle c-axis planar tunneling and STM spectra in high-T_c cuprates. *Physical Review Letters* **80** (20), 4546-9 (1998).

Franz 1996A. M. Franz, C. Kallin, P.I. Soininen, A.J. Berlinsky, and A.L. Fetter. Vortex state in a d-wave superconductor. *Physical Review B* **53** (9), 5795-814 (1996).

Franz 1996B. M. Franz, C. Kallin, A.J. Berlinsky. Impurity scattering and localization in d-wave superconductors. *Physical Review B* **54** (10), R6897-900 (1996).

Fukuyama 1996. H. Fukuyama, H. Tan, T. Handa, T. Kumakura, and M. Morishita. Construction of an ultra-low temperature scanning tunneling microscope. *Czechoslovak Journal of Physics* **46** (S5), 2847-8 (1996).

Fukuzumi 1996. Y. Fukuzumi, K. Mizuhashi, K. Takenaka, S. Uchida. Universal superconductor-insulator transition and T_c depression in Zn-substituted high-T_c cuprates in the underdoped regime. *Physical Review Letters* **76** (4), 684-7 (1996).

Garcia 1986. N. Garcia. Theory of scanning tunneling microscopy and spectroscopy: resolution, image and field states, and thin oxide layers. *IBM Journal of Research and Development* **30** (5), 533-42 (1986).

Gao 1988. Yan Gao, Peter Lee, Philip Coppens, M.A. Subramanian, and A.W. Sleight. The Incommensurate Modulation of the 2212 Bi-Sr-Ca-Cu-O Superconductor. *Science* **241** (4868), 954-6 (1988).

Giaever 1961. Ivar Giaever and Karl Megerle. Study of Superconductors by Electron Tunneling. *Physical Review* **122** (4), 1101-11 (1961).

Grévin 1998. B. Grévin, Y. Berthier, G. Collin, and P. Mendels. Evidence for charge instability in the CuO_3 chains of $PrBa_2Cu_3O_7$ from $^{63,65}Cu$ NMR. *Physical Review Letters* **80** (11), 2405-8 (1998).

Guéron 1996. S. Guéron, H. Pothier, N.O. Birge, D. Esteve, and M.H. Devoret. Superconducting proximity effect probed on a mesoscopic length scale. *Physical Review Letters* **77** (14), 3205-8 (1996).

Hancotte 1997. H. Hancotte, R. Deltour, D.N. Davydov, A.G.M. Jansen, P. Wyder. Superconducting order parameter in partially substituted $Bi_2Sr_2CaCu_2O_{8+x}$ single crystals as measured by the tunneling effect. *Physical Review B* **55** (6), R3410-13 (1997).

Hayashi 1996. N. Hayashi, M. Ichioka, and K. Machida. Star-shaped local density of states around vortices in a type-II superconductor. *Physical Review Letters* **77** (19), 4074-7 (1996).

Hayashi 1997. N. Hayashi, M. Ichioka, and K. Machida. Effects of gap anisotropy upon the electronic structure around a superconducting vortex. *Physical Review B* **56** (14), 9052-63 (1997).

Hess 1989. H.F. Hess, R.B. Robinson, R.C. Dynes, J.M. Valles Jr., and J.V. Waszczak, Scanning-Tunneling-Microscope Observation of the Abrikosov Flux Lattice and the Density of States near and inside a Fluxoid. *Physical Review Letters* **62** (2), 214-6 (1989).

Hess 1991. H. F. Hess, R. B. Robinson and J. V. Waszczak. STM spectroscopy of vortex cores and the flux lattice. *Physica B* **169**, 422-31 (1991).

Horiuchi 1996. Shigeo Horiuchi and Eiji Takayama-Muromachi, in *Bismuth-Based High-Temperature Superconductors*, edited by Hiroshi Maeda and Kazumasa Togano (Marcel Dekker, Inc., New York 1996), p. 7.

Hudson 1996. E. W. Hudson, R. W. Simmonds, C. A. YiLeon, S. H. Pan and J. C. Davis. A very low temperature vibration isolation system. *Czechoslovak Journal of Physics* **46** (S5), 2737-8 (1996).

Hudson 1999. E.W. Hudson, S.H. Pan, and J.C. Davis. Atomic Scale Quasiparticle Scattering Resonances in $Bi_2Sr_2CaCu_2O_{8+\delta}$. *Submitted to Science*.

Ichioka 1996. M. Ichioka, N. Hayashi, N. Enomoto, and K. Machida. Vortex structure in d-wave superconductors. *Physical Review B* **53** (22), 15316-26 (1996).

Ishida 1993. K. Ishida, Y. Kitaoka, N. Ogata, T. Kamino, K. Asayama, J.R. Cooper, N. Athanassopoulou. Cu NMR and NQR studies of impurities-doped $YBa_2(Cu_{1-x}M_x)_3O_7$ (M = Zn and Ni). *Journal of the Physical Society of Japan* **62** (8), 2803-18 (1993).

Joynt 1997. R. Joynt. Bound states and impurity averaging in unconventional superconductors. *Journal of Low Temperature Physics* **109** (5-6), 811-68 (1997).

Kampf 1997. A.P. Kampf and T.P. Devereaux. Extended impurity potential in a $d_{x^2-y^2}$ superconductor. *Physical Review B* **56** (5), 2360-3 (1997).

Keimer 1994. B. Keimer, *et al*. Vortex lattice symmetry and electronic structure in $YBa_2Cu_3O_7$. *Physical Review Letters* **73** (25), 3459-62 (1994).

Kikuchi 1995. A. Kikuchi and M. Tsukuda. Theory of STM images of CDW in transition-metal dichalcogenides. *Surface Science* **326** (1-2), 195-207 (1995).

Kirk 1988. M.D. Kirk *et al*. The Origin of the Superstructure in $Bi_2Sr_2CaCu_2O_{8+\delta}$ as Revealed by Scanning Tunneling Microscopy. *Science* **242** (4886), 1673-5 (1988).

Kirtley 1987. J.R. Kirtley, S.I. Raider, R.M. Feenstra, and A.P. Fein. Spatial variation of the observed energy gap in granular superconducting NbN films. *Applied Physics Letters* **50** (22), 1607-9 (1987).

Kirtley 1990. J.R Kirtley. Tunneling measurements of the energy gap in high-T_c superconductors. *International Journal of Modern Physics B* **4** (2), 201-37 (1990).

Kittel 1986. Charles Kittel. *Introduction to Solid State Physics* (John Wiley & Sons, Inc., New York, 1986).

Kleiner 1964. W.H. Kleiner, L.M. Roth, and S.H. Autler. Bulk solution of Ginzburg-Landau Equations for Type II Superconductors: Upper Critical Field Region. *Physical Review* **133** (5A), A1226-7 (1964).

Kluge 1995. T. Kluge, Y. Koike, A. Fujiwara, M. Kato, T. Noji, Y. Saito. Clear distinction between the underdoped and overdoped regime in the T_c suppression of Cu-site-substituted high-T_c cuprates. *Physical Review B* **52** (2), R727-30 (1995).

Kobayashi 1977. Norio Kobayashi, Koshichi Noto and Yoshio Muto. Thermodynamic Properties of the Layered Superconductor $2H\text{-}NbSe_2$. *Journal of Low Temperature Physics* **27** (1/2), 217-44 (1977).

Krusius 1993. M. Krusius. The vortices of superfluid ^3He. *Journal of Low Temperature Physics* **91** (5-6), 233-73 (1993).

Lal 1994. Ratan Lal, S.P. Pandey, A.V. Narlikar E. Gmelin. T_c depression in the $YBa_2Cu_{4-x}M_xO_8$ system for M=Fe, Ni, Zn, and Ga. *Physical Review B* **49** (9), 6382-4 (1994).

Lee 1993. P.A. Lee. Localized states in a d-wave superconductor. *Physical Review Letters* **71** (12), 1887-90 (1993).

Lee 1996. Shih-Fu Lee, D.C. Morgan, R.J. Ormeno, D.M. Broun, R.A. Doyle, R.A., J.R. Waldram, K. Kadowaki. a-b plane microwave surface impedance of a high-quality $Bi_2Sr_2CaCu_2O_8$ single crystal. *Physical Review Letters* **77** (4), 735-8 (1996).

Levin 1994. A.A. Levin, Y.I. Smolin and Y.F. Shepelev. Causes of modulation and hole conductivity of the high-T_c superconductor $Bi_2Sr_2CaCuO_{8+x}$ according to x-ray single-crystal data. *Journal of Physics: Condensed Matter* **6** (19), 3539-51 (1994).

Lindberg 1989. P.A.P. Lindberg, Z.X. Shen, B.O. Wells, D. Dessau, D.B. Mitzi, I. Lindau, W.E. Spicer, and A. Kapitulnik. Reaction of Rb and oxygen overlayers with single crystalline $Bi_2Sr_2CaCu_2O_{8+\delta}$ superconductors. *Physical Review B* **39** (4), 2890-3 (1989).

Maeda 1988. H. Maeda, Y. Tanaka, M. Fukutomi, and T. Asano. A new high-T_c oxide superconductor without a rare earth element. *Japanese Journal of Applied Physics Letters* **27** (2), L209-10 (1988).

Maeda 1990.   A. Maeda, T. Yabe, S. Takebayashi, M. Hase, K. Uchinokura. Substitution of 3d metals for Cu in $Bi_2(Sr_{0.6}Ca_{0.4})_3Cu_2O_y$. *Physical Review B*, **41** (7), 4112-17 (1990).

Maeda 1996.   Hiroshi Maeda and Kazumasa Togano, ed. *Bismuth-Based High-Temperature Superconductors.* (Marcel Dekker, In., New York, 1996).

Maggio-Aprile 1995. I. Maggio-Aprile, Ch. Renner, A. Erb, E. Walker, and Ø. Fischer. Direct Vortex Lattice Imaging and Tunneling Spectroscopy of Flux Lines on $YBa_2Cu_3O_{7-\delta}$. *Physical Review Letters* **75** (14), 2754-2757 (1995).

Maki 1995A.   Kazumi Maki, Nils Schopohl, Hyekyung Won. D-wave superconductor in high magnetic fields. *Physica B* **204** (1-4), 214-221 (1995).

Mallozzi 1998.   R. Mallozzi, J. Corson, J. Orenstein, J.N. Eckstein, I. Bozovic. Terahertz conductivity and c-axis plasma resonance in $Bi_2Sr_2CaCu_2O_{8+\delta}$. *Journal of the Physics and Chemistry of Solids* **59** (10-12), 2095-9 (1998).

Matricon 1964.   J. Matricon. Energy and elastic moduli of a lattice of vortex lines. *Physics Letters* **9** (4), 289-91 (1964).

Meservey 1988.   R. Meservey. Tunnelling in a magnetic field with spin-polarized electrons. *Physica Scripta* **38** (2), 272-6 (1988).

Mitzi 1990.   D.B. Mitzi, L.W. Lombardo, A. Kapitulnik, S.S. Laderman, and R.D. Jacowitz. Growth and properties of oxygen- and ion-doped $Bi_2Sr_2CaCu_2O_{8+\delta}$ single crystals. *Physical Review B* **41** (10A), 6564-74 (1990).

Mizuhashi 1995.   K. Mizuhashi, K. Takenaka, Y. Fukuzumi, S. Uchida. Effect of Zn doping on charge transport in $YBa_2Cu_3O_{7-y}$. *Physical Review B* **52** (6), R3884-7 (1995).

Mook 1996.   H.A. Mook, P. Dai, K. Salama, D. Lee, F. Dögan, G. Aeppli, A.T. Boothroyd, and M.E. Mostoller. Incommensurate one-dimensional fluctuations in $YBa_2Cu_3O_{6.93}$. *Physical Review Letters* **77** (2), 370-3 (1996).

Movshovich 1998.   R. Movshovich, M.A. Hubbard, M.B. Salamon, A.V. Balatsky, R. Yoshizaki, J.L. Sarrao, M. Jaime. Low-temperature anomaly in thermal conductivity of $Bi_2Sr_2Ca(Cu_{1-x}Ni_x)_2O_8$: second superconducting phase? *Physical Review Letters* **80** (9), 1968-71 (1998).

Murakami 1994.   H. Murakami, S. Ohbuchi, and R. Aoki. Tunneling observation of the finite superconducting gap in $YBa_2Cu_3O_y$. *Physica C* **235-240** (3), 1887-8 (1994).

Murakami 1996. H. Murakami and R. Aoki. LT-STM observation of definite superconducting gap states on the multistage crystal surface of $Bi_2Sr_2CaCu_2O_{8+x}$ in *Spectroscopic Studies of Superconductors Part B: Tunneling, Photoelectron and other Spectra*, Ivan Bozovic, Dirk van der Marel, Editors, *Proceedings of the SPIE* **2696** (B), 384-93 (1996).

Noetzel 1998. R. Noetzel and K. Westerholt. Vortex pinning by Ni point defects in $Bi_2Sr_2Ca(Cu_{1-x}Ni_x)_2O_{8+\delta}$ single crystals. *Physical Review B* **58** (22), 15108-15 (1998).

Overhauser 1978. A.W. Overhauser. Charge-density waves and isotropic metals. *Advances in Physics* **27** (3), 343-63 (1978).

Pan unpub. S.H. Pan, S. Behler, M. Bernasconi, H. Hidber, and H.-J. Güntherodt, unpublished.

Pan 1993. S. H. Pan. International Patent Publication Number WO 93/19494, International Bureau, World Intellectual Property Organization), 30 Sept. 1993.

Pan 1998A. S.H. Pan, E.W. Hudson, J. Ma and J.C. Davis. Imaging and identification of atomic planes of cleaved $Bi_2Sr_2CaCu_2O_{8+\delta}$ by high resolution scanning tunneling microscopy. *Applied Physics Letters* **73** (1), 58-60 (1998).

Pan 1998B. S.H. Pan, E.W. Hudson, and J.C. Davis. Vacuum tunneling of superconducting quasiparticles from atomically sharp scanning tunneling microscope tips. *Applied Physics Letters* **73** (20), 2992-4 (1998).

Pan 1999A. S.H. Pan, E.W. Hudson, and J.C. Davis. ^{3}He refrigerator based very low temperature scanning tunneling microscope. *Review of Scientific Instruments* **70** (2), 1459-63 (1999).

Peierls 1955. R.E. Peierls. Quantum Theory of Solids. (Clarendon Press, Oxford, 1955).

Petricek 1990. V. Petricek, Y. Gao, P. Lee, and P. Coppens. X-ray analysis of the incommensurate modulation in the 2:2:1:2 Bi-Sr-Ca-Cu-O superconductor including the oxygen atoms. *Physical Review B* **42** (1A), 387-92 (1990).

Pomar 1996. A. Pomar, M.V. Ramallo, J. Mosqueira, C. Torron, F. Vidal. Fluctuation-induced in-plane conductivity, magnetoconductivity, and diamagnetism of $Bi_2Sr_2CaCu_2O_8$ single crystals in weak magnetic fields. *Physical Review B* **54** (10), 7470-80 (1996).

Preparata 1985. F. Preparata and M.I. Shamos. *Computational Geometry An Introduction* 198-217 (Springer-Verlag, New York, 1985).

Ren 1995. Y. Ren, J.-H. Xu, and C.S. Ting. Ginzburg-Landau Equations and Vortex Structure of a $d_{x^2-y^2}$ Superconductor. *Physical Review Letters* **74** (18), 3680-3 (1995).

Renner 1995. Ch. Renner and Ø. Fischer. Vacuum tunneling spectroscopy and asymmetric density of states of $Bi_2Sr_2CaCu_2O_{8+\delta}$. *Physical Review B* **51** (14), 9208-18 (1995).

Renner 1998. Ch. Renner, B. Revaz, K. Kadowaki, I. Maggio-Aprile, and Ø. Fischer. Observation of the Low Temperature Pseudogap in the Vortex Cores of $Bi_2Sr_2CaCu_2O_{8+\delta}$. *Physical Review Letters* **80** (1), 3606-3609 (1998).

Sà de Melo 1998. C.A.R. Sà de Melo, ed. *The Superconducting State in Magnetic Fields.* (World Scientific, London, 1998).

Salkola 1996. M.I. Salkola, A.V. Balatsky, and D.J. Scalapino. Theory of Scanning Tunneling Microscopy Probe of Impurity States in a D-Wave Superconductor. *Physical Review Letters* **77** (9), 1841-4 (1996).

Salkola 1998. M.I. Salkola and J.R. Schrieffer. Unusual states of inhomogeneous $d_{x^2-y^2}+id_{xy}$ superconductors. *Physical Review B* **58** (10), R5952-5 (1998).

Salomaa 1987. M.M Salomaa and G.E. Volovik. Quantized vortices in superfluid ^{3}He. *Rev. Mod. Phys.* **59** (3), 533-613 (1987).

Schopohl 1995. N. Schopohl, K. Maki. Quasiparticle spectrum around a vortex line in a d-wave superconductor. *Physical Review B* **52** (1), 490-3 (1995).

Shen 1993. Z.-X. Shen, D.S. Dessau, B.O. Wells, D.M. King, W.E. Spicer, A.J. Arko, D. Marshall, L.W Lombardo, A. Kapitulnik, P. Dickinson, S. Doniach, J. DiCarlo, A.G. Loeser, C.H. Park. Anomalously large gap anisotropy in the a-b plane of $Bi_2Sr_2CaCu_2O_{8+\delta}$. *Physical Review Letters* **70** (10), 1553-6 (1993).

Shih 1989. C.K. Shih, R.M. Feenstra, J.R. Kirtley, and G.V. Chandrashekhar. Surface structural and electronic properties of cleaved single crystals of $Bi_{2.15}Sr_{1.7}CaCu_2O_{8+\delta}$ compounds: a scanning tunneling microscopy study. *Physical Review B* **40** (4), 2682-5 (1989).

Shiraishi 1999. J. Shiraishi, M. Kohmoto, and K. Maki. Vortex lattice transition in d-wave superconductors. *Physical Review B* **59** (6), 4497-503 (1999).

Shore 1989. J.D. Shore, M. Huang, A.T. Dorsey, and J.P. Sethna. Density of states in a vortex core and the zero-bias tunneling peak. *Physical Review Letters* **62** (26), 3089-92 (1989).

Soininen 1994. P.I. Soininen, C. Kallin, and A.J. Berlinsky. Structure of a vortex line in a $d_{x^2-y^2}$ superconductor. *Physical Review B* **50** (18), 13883-6 (1994).

Solymar 1972. L. Solymar, *Superconductive Tunneling and Applications.* (Wiley-Interscience, New York 1972).

Stroscio 1986. J.A. Stroscio, R.M. Feenstra, and A.P. Fein. Electronic structure of the Si(100)2x1 surface by scanning tunneling microscopy. *Physical Review Letters* **57** (20), 2579-82 (1986).

Subramanian 1988. M.A. Subramanian, C.C. Torardi, J.C. Calabrese, J. Gopalakrishnan, K.J. Morrissey, T.R. Askew, R.B. Flippen, U. Chowdhry, and A.W. Sleight. A New High-Temperature Superconductor: $Bi_2Sr_{3-x}Ca_xCu_2O_{8+y}$. *Science* **239** (4843), 1015-7 (1988).

Sunshine 1988. S.A. Sunshine, T. Siegrist, L.F. Schneemeyer, D.W. Murphy, R.J. Cava, B. Batlogg, R.B. van Dover, R.M. Fleming, S.H. Glarum, S. Nakahara, R. Farrow, J.J. Krajewski, S.M. Zahurak, J.V. Waszczak, J.H. Marshall, P. Marsh, L.W. Rupp, Jr., and W.F. Peck. Structure and physical properties of single crystals of the 84-K superconductor $Bi_{2.2}Sr_2Ca_{0.8}Cu_2O_{8+\delta}$. *Physical Review B* **38** (1), 893-6 (1988).

Tallon 1997. J.L. Tallon, C. Bernhard, G.V.M. Williams, J.W. Loram. Zn-induced T_c reduction in high-T_c superconductors: scattering in the presence of a pseudogap. *Physical Review Letters* **79** (26), 5294-7 (1997).

Tersoff 1983. J. Tersoff and D.R. Hamann. Theory and application for the scanning tunneling microscope. *Physical Review Letters* **50** (25), 1998-2001 (1983).

Tersoff 1985. J. Tersoff and D.R. Hamann. Theory of the scanning tunneling microscope. *Physical Review B* **31** (2), 805-13 (1985).

Tinkham 1996. M. Tinkham. *Introduction to Superconductivity* (McGraw-Hill, Inc., New York, 1996).

Townsend 1962. P. Townsend and J. Sutton. Investigation by Electron Tunneling of the Superconducting Energy Gaps in Nb, Ta, Sn and Pb. *Physical Review* **128**, 591-5 (1962).

Vinen 1961. W.F. Vinen. The detection of single quanta of circulation in liquid helium II. *Proceedings of the Royal Society of London A* **260**, 218-36 (1961).

Volodin 1997. A.P. Volodin, A.A. Golubov, and J. Aarts. Vortex core shapes measured by STM. *Zeitschrift fur Physik B* **102** (3), 317-21 (1997).

Volovik 1993. G.E. Volovik. Superconductivity with lines of GAP nodes: density of states in the vortex. *Pis'ma v Zhurnal Eksperimental'noi i Teoreticheskoi Fiziki* **58** (6), 457-61; *JETP Letters* **58** (6), 469-73 (1993).

vom Hedt 1994. B. vom Hedt, W. Lisseck, K. Westerholt, H. Bach. Superconductivity in $Bi_2Sr_2CaCu_2O_{8+\delta}$ single crystals doped with Fe, Ni, and Zn. *Physical Review B* **49** (14), 9898-905 (1994).

White 1999A. P.J. White, Z. X. Shen, D. L. Feng, C. Kim, M. Z. Hasan, J. M. Harris, A. G. Loeser, H. Ikeda, R. Yoshizaki, G. D. Gu, N. Koshizuka. Zn Impurities in $Bi_2Sr_2CaCuZnO(I)$ - Electronic Structure Evolution. cond-mat/9901349 (1999).

White 1999B. P. J. White, Z. X. Shen, D. L. Feng, C. Kim, M. Z. Hasan, A. G. Loeser, H. Ikeda, R. Yoshizaki, G. D. Gu, N. Koshizuka. Zn Impurities in BiSrCa(CuZn)O II - Temperature Induced Spectral Change. cond-mat/9901354 (1999).

Wilson 1975. J.A. Wilson, F.J. Di Salvo and S. Mahajan. Charge-density waves and superlattices in the metallic layered transition metal dichalcogenides. *Advances in Physics* **24** (2), 117-201 (1975).

Williams 1976. P.M. Williams. Phase Transitions and Charge Density Waves in the Layered Transition Metal Dichalcogenides, in *Crystallography and Crystal Chemistry of Materials with Layered Structures*, F. Lévy, ed., 51-92 (D. Reidel Publishing Company, Dordrecht-Holland, 1976).

Wolf 1985. E.L. Wolf, *Principles of Electron Tunneling Spectroscopy* (International series of monographs on physics; 71) (Oxford University Press, New York 1985).

Woolf 1965. Michael A. Woolf and F. Reif. Effect of Magnetic Impurities on the Density of States of Superconductors. *Physical Review* **137**, A557-64 (1965).

Xiao 1990. G. Xiao, M.Z. Cieplak, J.Q. Xiao, C.L. Chien. Magnetic pair-breaking effects: moment formation and critical doping level in superconducting $La_{1.85}Sr_{0.15}Cu_{1-x}A_xO_4$ systems (A=Fe, Co, Ni, Zn, Ga, Al). *Physical Review B* **42** (13.B), 8752-5 (1990).

Xu 1995. Ji-Hai Xu, Yong Ren, and C.S. Ting. Ginzburg-Landau equations for a d-wave superconductor with applications to vortex structure and surface problems. *Physical Review B* **52** (10), 7663-74 (1995).

Yamamoto 1990. A. Yamamoto, M. Onoda, E. Takayama-Muromachi, F. Izumi, T. Ishigaki, and H. Asano. Rietveld analysis of the modulated structure in the superconducting oxide $Bi_2(Sr,Ca)_3Cu_2O_{8+x}$. *Physical Review B* **42** (7), 4228-39 (1990).

Yang 1993. G. Yang, S. Sutton, P. Shang, C.E. Gough, and J.S. Abell. Growth of BSCCO and YBCO single crystals using large temperature gradients. *IEEE Transaction on Applied Superconductivity* **3** (1), 1663-6 (1993).

Yazdani 1997. A. Yazdani, B.A. Jones, C.P. Lutz, M.F. Crommie and D.M. Eigler. Probing the local effects of magnetic impurities on superconductivity. *Science* **275** (5307), 1767-70 (1997).

Ziegler 1996. K. Ziegler, M.H. Hettler, P.J. Hirschfeld. Nonzero Fermi level density of states for a disordered d-wave superconductor in two dimensions. *Physical Review Letters* **77** (14), 3013-16 (1996).

Appendix A.

Control and Data Acquisition: Software Protocols

In this appendix I will provide an outline of the steps used by the software for various standard routines, including tip approach, spectroscopy and mapping. In each case I will indicate the steps that are controlled by user-modifiable variables (for example, delay times) as well as the standard values (or sets of standard values) used.

A.1. Tip Approach – "Woodpecker Mode"

The tip approach routine is specifically written to put the tip and sample at as little risk of crashing during the approach as possible. For this reason, the approach is quite slow, essentially consisting of walking the walker one step, and then reaching out with the scanner to see if the surface is in range before withdrawing and stepping again. Because of the length of time involved, we usually perform approaches overnight, and thus the routine to determine whether the tip has actually found the surface must also be completely robust, as a false approach could cost hours of run time.

First of all, a note about units. Many of the variables are specified in bits. All variables are 16 bit so one bit is 1.5 x 10^{-5} of full scale, or 6.7 mV on the high voltage outputs ($\pm$ 220 V full range), 305 μV on the low voltage outputs ($\pm$ 10 V full range). Time is frequently specified in units of the clock cycle. The DSP runs at 100 kHz so one "clock cycle" is roughly 10 μS.

Woodpecker Approach Mode
1. Ramp z-piezo forward while looking for current:
   1.1. Average current signal (INTERRUPTSPERFWDDELTA [10] clock cycles)
   1.2. If average larger than current setpoint, return to 'Surface Found' (7.)
   1.3. Ramp z-piezo forward (BITSPERFWDDELTA [4] bits)
   1.4. Repeat 1.1 – 1.4 until piezo fully extended towards surface
Surface Not Found
2. Ramp z-piezo to full withdrawal (BITSPERBKDDELTA [4] bits/clock cycle)
3. Delay to make sure fully withdrawn (AFTERRAMPBACKDELAY [10] ms)
4. If still in approach mode (ie. user hasn't cancelled) send one pulse to walker
5. Delay to let walker settle (AFTERMOTORDELAY [100] ms)
6. Repeat to 1. Until Surface Found
Surface Found
7. Ramp z-piezo to full withdrawal (BITSPERBKDDELTA [4] bits/clock cycle)
8. Delay to let spurious noise pass (1000 ms)
9. Repeat step 1. to see if the surface is found again. If not, restart loop at 1. If so…
10. Delay to really let spurious noise pass (10000 ms)

11.   Repeat the entire surface found routine (with two ramp checks) one more time.

The last two steps were included much later to ensure that there would be no false approaches overnight. At this point, the walker is grounded and a final, slow ramp [3 V/s] of the z-piezo is made to bring it into tunneling before turning on the feedback.

A.2. IV and IS Spectroscopy

The IV and IS Spectroscopy routines are quite straight forward, and involve turning off the feedback, ramping to a given voltage/position, averaging the input value, and then repeating. There are many variables that may vary however, which are indicated below (when different, the IV and IS values are indicated respectively, separated by a slash (/)). Note also that IV spectroscopy can be turned into CITS (constant current tunneling spectroscopy) by scanning to each point in the map sequentially and performing the below routine.

1. Delay to ensure good feedback (ESTABLISHFEEDBACK [2 s]).
2. Turn off the feedback
3. **V only**: Ramp to the starting voltage (V_{start}) at the initial ramp rate (STARTPOINT [1 V/s])
4. Pause at the starting value to let settle (DELAYSTART [1 s]).
Take Data
5. Ramp (SAMPLEPOINT [0.1 V/s]) to the next voltage/Z value at which to take data.
6. Pause to let settle (BEFORESAMPLE [0.1 s]).
7. Read data at the sampling rate (100 kHz) (for AVERAGING [0.1 s]) and average.
8. Repeat steps 5-7 until the half cycle (from V/Z_{start} to V/Z_{end}) is completed.
End Of Half Cycle (Start to End)
If more than one half-cycle is requested, repeat **Take Data** from *End* to *Start*.
End Of Full Cycle (Start to End)
9. If more than two half cycles are requested, then if FEEDBACKBETWEENCYCLES:
    9.1. Ramp back to the feedback point (FEEDBACKPOINT [1 V/s])
    9.2. Delay to establish feedback (ESTABLISHFEEDBACK [2 s])
10. Repeat from 2 to finish remaining half cycles

A.3. Differential Conductance Spectroscopy

The differential tunneling conductance (or dI/dV spectroscopy) routines are quite similar to the IV and IS routine of section B.2, with the exception that the lock-in modulation must be turned on and off at appropriate times. We have developed two sets of times, "fast" and "slow," which will both be listed below, separated by a slash (/). Also, many of the times depend directly on the time constant τ chosen, so in this case the value will be quoted in terms of τ. The procedure is as follows:

1. Delay to ensure good feedback (ESTABLISHFEEDBACK [0.15 s / 2 s])
2. Turn off the feedback
3. Turn on the bias modulation
4. Ramp to the starting voltage (V_{start}) at the initial rate (STARTPOINT [20 V/s / 1 V/s])
5. Pause at the starting value to let settle (DELAYSTART [100τ]) (NOTE: For mapping, only 10τ is used).

Take Data

6. Ramp (SAMPLEPOINT [2 V/s / 0.1 V/s]) to the next voltage at which to take data.
7. Pause to let settle (BEFORESAMPLE [9τ]).
8. Read data at the sampling rate (100 kHz) (for AVERAGING [3τ]) and average.
9. Repeat steps 5-7 until the half cycle (from V_{start} to V_{end}) is completed.

End Of Half Cycle (Start to End)

If more than one half-cycle is requested, repeat **Take Data** from *End* to *Start*.

End Of Full Cycle (Start to End)

10. If more than two half cycles are requested, then if FEEDBACKBETWEENCYCLES:
    10.1. Ramp back to the feedback point (FEEDBACKPOINT [1 V/s])
    10.2. Turn off bias modulation
    10.3. Delay to establish feedback (ESTABLISHFEEDBACK [0.15 s / 2 s])
11. Repeat from 2 to finish remaining half cycles

So, in summary:

'Rate'	Frequency	Time Const.	Start Delay (map time)	Sample Delay	Average
Very Slow	447.3 Hz	100 ms	10 s	900 ms	300 ms
Slow	447.3 Hz	30 ms	3 s (0.3 S)	270 ms	100 ms
Fast	1.1137 kHz	3 ms	0.3 s (30 ms)	27 ms	10 ms

Appendix B.

Distributors and Manufacturers

Company Name	Product	Location	Phone
Acra Ball Manufacturing	Sapphire Balls	Anaheim, CA	714-632-3801
Alfa Aesar	Elements, Ceramics	Ward Hill, MA	800-343-0660
American Magnetics	Magnets	Oak Ridge, TN	423-482-1056
Balzers-Pfeiffer	Vacuum Products	Hudson, NH	603-889-6888
Ceramic Products	Macor	Palisades Park, NJ	201-947-0336
Coors Ceramic Company	Alumina Sheet	Golden, CO	800-821-6110
D.L. Instruments	Amplifiers	Ithaca, NY	607-277-8498
Gebrüder Wild Edelsteine	Sapphire Prism	Germany	49-06781-43370
Kadel Engineering	Dewars	Danville, IN	317-745-2798
Lake Shore Cryogenics	Cryogenic Products	Westerville, OH	614-891-2243
Monocrystals Co.	Single Crystal Au	Richmond Heights, OH	216-531-7820
Staveley Sensors	Piezos	East Hartford, CT	860-291-2526
Technical Manufacturing Corporation	Airsprings	Peabody, MA	978-532-6330
ThermoMicroscopes	STM Controller	Sunnyvale, CA	800-776-1602
Union Carbide Crystal Products	HOPG	Washougal, WA	360-835-2001
Varian Vacuum Products	Vacuum Products	Lexington, MA	800-882-7426